

Fundamental studies of superconductors using scanning magnetic imaging

J.R. Kirtley

Center for Probing the Nanoscale, Stanford University, Stanford, California, USA

Abstract. In this review I discuss the application of scanning magnetic imaging to fundamental studies of superconductors, concentrating on three scanning magnetic microscopies - scanning SQUID microscopy (SSM), scanning Hall bar microscopy (SHM), and magnetic force microscopy (MFM). I briefly discuss the history, sensitivity, spatial resolution, invasiveness, and potential future developments of each technique. I then discuss a selection of applications of these microscopies. I start with static imaging of magnetic flux: An SSM study provides deeper understanding of vortex trapping in narrow strips, which are used to reduce noise in superconducting circuitry. Studies of vortex trapping in wire lattices, clusters, and arrays of rings and nanoholes show fascinating ordering effects. The cuprate high- T_c superconductors are shown to have predominantly d -wave pairing symmetry by magnetic imaging of the half-integer flux quantum effect. Arrays of superconducting rings act as a physical analog for the Ising spin model, with the half-integer flux quantum effect helping to eliminate one source of disorder in antiferromagnetic arrangements of the ring moments. Tests of the interlayer tunneling model show that the condensation energy available from this mechanism can not account for the high critical temperatures observed in the cuprates. The strong divergence in the magnetic fields of Pearl vortices allows them to be imaged using SSM, even for penetration depths of a millimeter. Unusual vortex arrangements occur in samples comparable in size to the coherence length. Spontaneous magnetization is not observed in Sr_2RuO_4 , which is believed to have $p_x \pm ip_y$ pairing symmetry, although effects hundreds of times bigger than the sensitivity limits had been predicted. However, unusual flux trapping is observed in this superconductor. Finally, unusual flux arrangements are also observed in magnetic superconductors. I then turn to vortex dynamics: Imaging of vortices in rings of highly underdoped cuprates places limits on spin-charge separation in these materials. Studies of spontaneous generation of fluxoids upon cooling rings through the superconducting transition provide clues to dynamical processes relevant to the early development of the universe, while studies of vortex motion in cuprate grain boundaries allow the measurement of current-voltage characteristics at the femtovolt scale for these technologically important defects. Scanning SQUID susceptometry allows the measurement of superconducting fluctuations on samples comparable in size to the coherence length, reveal stripes in susceptibility believed to be associated with enhanced superfluid density on the twin boundaries in the pnictide superconductor Co-doped Ba-122, and indicate the presence of spin-like excitations, which may be a source of noise in superconducting devices, in a wide variety of materials. Scanning magnetic microscopies allow the absolute value of penetration depths to be measured locally over a wide temperature range, providing clues to the symmetry of the order parameter in unconventional superconductors. Finally, MFM tips can be used to manipulate vortices, providing information on flux trapping in superconductors.

Contents

1 Introduction

<i>CONTENTS</i>	2
2 Fundamentals	4
2.1 Scanning SQUID microscopy	4
2.2 Hall bar microscopy	11
2.3 Magnetic force microscopy	13
2.4 Summary	16
3 Applications	18
3.1 Static imaging of magnetic flux	18
3.1.1 Narrow strips	19
3.1.2 Superconducting wire lattices, clusters, and nano-hole arrays . . .	21
3.1.3 Half-integer flux quantum effect	21
3.1.4 Ring arrays	25
3.1.5 Tests of the interlayer tunneling model	26
3.1.6 Pearl vortices	27
3.1.7 Mesoscopic superconductors	30
3.1.8 Sr_2RuO_4	31
3.1.9 Magnetic superconductors	32
3.2 Fluxoid dynamics	33
3.2.1 Limits on spin-charge separation	33
3.2.2 Superconducting rings	34
3.2.3 High- T_c grain boundaries	35
3.3 Local susceptibility measurements	37
3.3.1 Superconducting fluctuations	37
3.3.2 Stripes	38
3.3.3 Spinlike susceptibility	40
3.4 Penetration depths	40
3.5 Manipulation of individual vortices	44
4 Conclusions	45
5 Acknowledgements	46

1. Introduction

Superconductivity, the complete absence of electrical resistance in some metals below a critical temperature T_c , is one of the best understood phenomena in solid-state physics. As described in the Bardeen-Cooper-Schrieffer (BCS) theory [1], superconductivity occurs in conventional superconductors through phonon-mediated pair-wise interaction of charge carriers to form Cooper pairs. The characteristic energy needed to form a single particle excitation from the superconducting condensate is the energy gap Δ . The Cooper pairs form a macroscopic quantum state characterized by a wave function $\psi(\vec{r}) = |\psi(\vec{r})|e^{i\phi(\vec{r})}$, where ϕ is the Cooper pair phase, with the density of Cooper pairs $n_s(\vec{r}) = |\psi(\vec{r})|^2$. The macroscopic quantum nature of the pairing state leads to a wide variety of behaviors: persistent currents, Meissner screening, flux quantization, the Josephson effects, and superconducting quantum interference. Superconductivity has become a multi-billion dollar industry, with applications in medical imaging, cell phone filters, electrical motors, power transmission, transportation, magnetic manipulation, magnetic sensing, etc.

However, there is still much to learn about superconductivity: Although superconductivity in the copper-oxide based perovskites [2, 3] was discovered in 1986, despite almost 25 years of intense effort a consensus on the pairing mechanism in the cuprates has yet to emerge. The heavy Fermion superconductors [4, 5] have large carrier masses, strong interaction between spin and charge degrees of freedom, and potentially a wide variety of Cooper pairing symmetries. The non-cuprate perovskite superconductor Sr_2RuO_4 [6] is believed to have a p -wave pairing state that breaks time reversal symmetry [7]. Interest in unconventional superconductors has been reawakened with the discovery of iron-based compounds with high critical temperatures [8].

Scanning magnetic microscopies have played, and will continue to play, an important part in our efforts to understand superconductivity. There are now a large number of scanning magnetic microscopies. Although it is beyond the scope of this review to cover all of these techniques in detail, it is appropriate to briefly describe some, and provide a few citations as an introduction to the literature:

In Lorentz microscopy [9, 10, 11, 12], a coherent beam of high energy (300keV) electrons are passed through a thin sample and then imaged slightly off the focal plane. Magnetic fields introduce small phase shifts which cause interference in the defocused image. Lorentz microscopy can image vortices with deep sub-micron spatial resolution at video rates and is sensitive not only to surface fields but also to fields within the sample. However, the sample must be thinned.

In magneto-optic microscopy [13, 14, 15], the sample is illuminated with linearly polarized light. It passes through a magneto-optically active layer, reflects off the sample surface, passes again through the magneto-optically active layer, and then through a crossed polarizer. Regions of the sample with magnetic fields produce rotations of the polarization axis of the light, which is detected as a bright spot. Magneto-optic microscopy has the advantage of relative simplicity, but has limited spatial resolution and sensitivity. Nevertheless, observation of individual superconducting vortices with $0.8\mu\text{m}$ spatial resolution has recently been reported [15].

In Sagnac interferometry [16, 17, 18], a single beam of light is split into two components which travel along identical paths in opposite directions around a loop. Any effects which break the time reversal symmetry, including the magneto-optical effect, will cause interference, which can be sensitively detected. High spatial resolution can be achieved using scanning near-field optical microscopy [17].

In spin polarized scanning tunneling microscopy [19, 20, 21] a scanning tunneling

microscope has a tunneling tip with a ferromagnetic or antiferromagnetic atom from which the tunneling electrons emerge. The tunneling probability depends on the spin polarization of the sample, and therefore contrast is achieved if there are spatial variations in the atomic spin polarizations. Spin polarized tunneling is useful for studying superconductivity in, for example, the high-temperature cuprate superconductors, since it is believed that magnetism and superconductivity are intimately related in these materials. However, the spin polarized tunneling current is not directly related to the local magnetic fields.

In diamond nitrogen-vacancy microscopy [22, 23, 24, 25, 26], a magnetic field dependent shift in the energy levels of a single nitrogen-vacancy center in diamond is detected optically. There are two basic schemes for detecting this energy shift. In the “dc” technique, microwaves at a fixed frequency as well as light are incident on the center. The intensity of the resultant fluorescence depends on the local magnetic field. This method can detect milliTesla fields with, in principle, nanometer scale spatial resolution. In the “ac” technique, spin-echo microwave techniques are used to detect the modulation of the center’s energy levels by the local magnetic field. The “ac” technique has a sensitivity of 60 nT, with in principle a spatial resolution of a few nm, but has reduced sensitivity at zero frequency. These techniques have the advantages of good sensitivity, small invasiveness, room temperature operation, inherently high speed, and potentially high spatial resolution. It remains to be seen whether single nitrogen-vacancies in nm sized diamond crystallites can be placed at the end of scanning tips while still retaining long lifetimes. This is necessary to achieve high spatial resolution and sensitivity simultaneously.

A magnetic tunnel junction [27, 28, 29] is a planar structure with two ferromagnetic electrodes. The tunneling current through the junction depends on the relative alignment of the magnetic moments of the electrodes, and therefore depends on the magnetic field environment. Magnetic tunnel junctions suitable for scanning microscopy are commercially available. They currently have lateral dimensions (and therefore spatial resolutions) of about 4 microns, and field noises at 100 Hz of about $5 \times 10^{-8} T / Hz^{1/2}$ [29]. They have the advantage of room temperature operation, but are not currently as sensitive as Hall bars or SQUIDs.

There are already excellent reviews covering the topic of magnetic imaging of superconductors [30, 31, 32], and there has been an enormous amount of work in this area. I will therefore not attempt to survey the field exhaustively, but will only cover recent work in three scanning magnetic microscopy techniques: scanning SQUID, scanning Hall bar, and magnetic force microscopies. I will present a short introduction to the basics, advantages and shortcomings of each technique, and then present a selection of fundamental applications of these magnetic microscopies in the area of superconductivity.

2. Fundamentals

2.1. Scanning SQUID microscopy

Josephson [33] predicted in 1962 the possibility of coherent tunneling of Cooper pairs between two weakly coupled superconductors, and wrote down the fundamental relations:

$$\begin{aligned} I_s &= I_0 \sin \varphi \\ V &= \frac{\hbar}{2e} \frac{d\varphi}{dt}, \end{aligned} \tag{1}$$

where I_s is the supercurrent through the weak link, φ is the difference between the Cooper pair phases on the two sides of the weak link, V is the voltage across the weak link, and I_0 is the critical current, the maximum current that can pass through the weak link before a voltage develops. A physical Josephson junction can be modeled as an ideal Josephson element in parallel with a capacitor and a resistor in the resistively shunted junction (RSJ) model [34, 35]. This model obeys the equation:

$$I_B = \frac{\hbar}{2eR} \frac{d\varphi}{dt} + I_0 \sin \varphi + \frac{\hbar C}{2e} \frac{d^2\varphi}{dt^2} + I_n, \quad (2)$$

where I_B is the bias current through the weak link, R is the resistance, C is the capacitance, and I_n is a noise current, given for the case of an ideal Johnson noise source resistor by

$$\langle I_n \rangle^2 = 4k_B T \Delta f / R, \quad (3)$$

where $\langle I_n \rangle^2$ is the time-averaged current noise squared, and Δf is the frequency band width over which the current noise is measured. This equation has the form of the equation of motion of a driven, damped harmonic oscillator. The dynamics of a Josephson weak-link can be visualized as that of a particle moving in a sinusoidal “washboard” potential with oscillation amplitude $I_0\Phi_0/2\pi$, where $\Phi_0 = h/2e$ is the superconducting flux quantum, and the average slope of the potential is given by $\langle dE/d\varphi \rangle = \Phi_0(I_B - I_n)/2\pi$. In the absence of a noise current, the particle will escape from a local potential minimum and run down the washboard potential if the bias current I_B is greater than I_0 , in the process developing a voltage given by the second of Eq.s 1. The solutions to Eq. 2 can be divided into two classes, according to whether the Stewart-McCumber parameter $\beta_c = 2\pi I_0 R^2 C / \Phi_0$ is greater or less than 1. If $\beta_c < 1$, a running particle retraps into a local potential minimum ($V = 0$), as soon as $I_B = I_0$, and the current-voltage characteristic is non-hysteretic. On the other hand, if $\beta_c > 1$, a running particle is not retrapped until $I_B < I_0$, and the current-voltage characteristic is hysteretic. In the presence of noise, the SQUID can be thermally excited out of the zero-voltage state at bias current $I_B < I_0$ [36]. In addition, the weak-link can macroscopically quantum tunnel through the barrier from the zero-voltage to the voltage state [37].

A Superconducting Quantum Interference Device (SQUID) is a superconducting ring interrupted by at least one Josephson weak link. For SQUID microscope applications a SQUID with two weak-links is most often used. Such a SQUID is labelled a dc-SQUID, since the modulation of the SQUID critical current with applied magnetic field can be observed using time-independent bias currents. Consider a SQUID with two weak-links 1, 2 with critical currents I_{c1}, I_{c2} , phase drops across the weak-links φ_1, φ_2 , and inductances in the two arms of the SQUID L_1, L_2 . Neglecting for the moment the current through the resistive and capacitive elements of the junctions, the bias current across the SQUID I_B and the magnetic flux through the SQUID Φ are given by

$$\begin{aligned} I_B &= I_1 \sin \varphi_1 + I_2 \sin \varphi_2 \\ \Phi &= \Phi_a - L_1 I_1 + L_2 I_2, \end{aligned} \quad (4)$$

where Φ_a is the externally applied flux. Integrating all the changes in phase around the SQUID loop along a path sufficiently deep inside the superconductor that there are no supercurrents along the integration path (i.e. they are shielded out by the bulk of the superconductor), and using the fact that the canonical momentum of the Cooper pairs is given by $\vec{p}_{\text{canonical}} = \vec{p} + q\vec{A}$, where $q = 2e$ is the charge on the Cooper pairs and \vec{A} is the vector potential, and finally by insisting that the Cooper pair wavefunction be

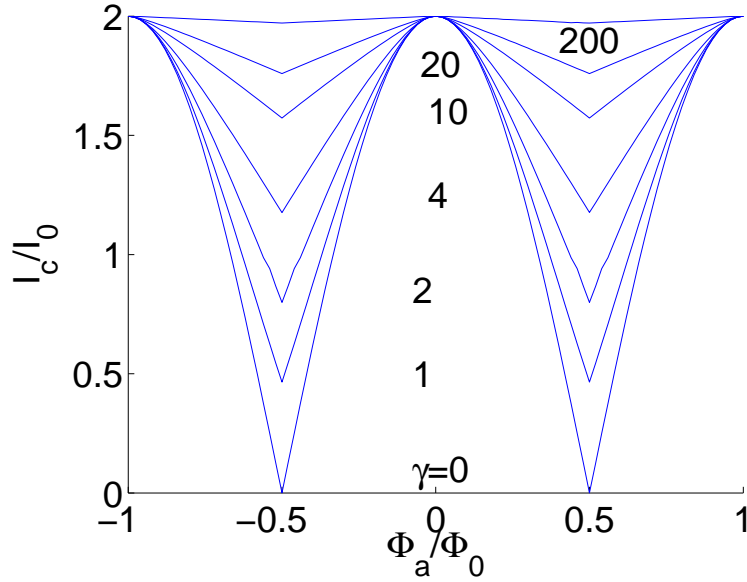


Figure 1. Plot of the critical current I_c of a symmetric ($L_1 = L_2 = L/2$, $I_1=I_2=I_0$) 2-weak link SQUID as a function of applied flux, for different values of the parameter $\gamma = 2\pi LI_0/\Phi_0$. I_0 is the critical current of one of the weak-links, and L is the total inductance of the SQUID.

single valued, leads to

$$2\pi n = \varphi_2 - \varphi_1 + \frac{2\pi}{\Phi_0}(\Phi_a + L_2 I_2 - L_1 I_1) \quad (5)$$

n an integer. Solutions to Equations 4 and 5 are shown in Figure 1 for the case of symmetric weak-link critical currents ($I_{c1} = I_{c2}$) and arm inductances ($L_1 = L_2$). The parameter $\gamma = 2\pi LI_0/\Phi_0$ ($L=L_1+L_2$) determines the depth of the modulation of the SQUID critical current with flux: larger SQUID inductances lead to smaller modulations. The solutions for non-symmetric SQUIDs are more complicated, but qualitatively similar [38] to those shown here.

There are 4 relevant sources of noise in dc SQUIDs: Johnson noise arises from thermal fluctuations, assumed to be dominated by the shunt resistor in the RSJ model [39]; shot noise arises from the discrete charge of the quasiparticles [40] and Cooper pairs [41] traversing the weak-links; quantum noise arises from zero point motion in the shunt resistors [42]; and $1/f$ noise can arise from a number of sources. Tesche and Clarke calculate [39] that the signal to noise ratio in dc SQUIDs is optimized when $\beta_L = 2LI_0/\Phi_0 \approx 1$. In addition, the Stewart-McCumber parameter β_c should be about 1, so that the SQUID is just non-hysteretic. If these two conditions are met, the optimal flux noise power S_Φ from the first three sources is given by:

$$S_\Phi = \begin{cases} 4k_B T L (\pi L C)^{1/2} & \text{Johnson noise} \\ hL & \text{Shot noise} \\ \hbar L & \text{Quantum noise.} \end{cases} \quad (6)$$

Typical values for scanning SQUID sensors using a Nb-Al₂O₃-Nb trilayer process are $L = 100$ pH, $I_0 = 6 \mu\text{A}$, $C = 8.36 \times 10^{-13}$ F, $R = 5 \Omega$ and $T = 4.2$ K. These parameters lead to $\Phi_{\text{Johnson}} = \sqrt{S_\Phi} = 3 \times 10^{-7} \Phi_0 / \sqrt{\text{Hz}}$ for the flux noise due to Johnson noise;

$\Phi_{\text{shot}} = 1.2 \times 10^{-7} \Phi_0 / \sqrt{\text{Hz}}$ for shot noise; and $\Phi_{\text{quantum}} = 5 \times 10^{-8} \Phi_0 / \sqrt{Hz}$ for noise due to zero point motion.

In the frequency range of interest Johnson noise, shot noise, and quantum noise are “white”: the frequency distribution of the noise is independent of frequency f . $1/f$ noise, as its name implies, has a noise amplitude that follows a $1/f$ dependence. It almost always dominates the noise in SQUIDs at sufficiently low frequencies. In the Dutta, Dimon, and Horn model [43] $1/f$ noise results from the superposition of “shot-like” contributions from two-level traps with a large distribution of trap energies. These traps could be, for example, defects in the oxide in a tunnel junction, or trap sites for superconducting vortices in the superconducting bulk making up the SQUID. Koch, Divincenzo, and Clarke [44] have suggested that $1/f$ noise in SQUIDs could result from coupling of flux into the SQUID from electronic spins with a wide distribution of characteristic times.

As can be seen in Figure 1, the critical current of the SQUID is periodic in flux, with a period given by Φ_0 . The most commonly used scheme for determining this magnetic flux uses *ac* flux modulation in a flux locked loop [45, 46]. If the SQUID is current biased just above the critical current the voltage varies sinusoidally with flux. If the *dc* component of the total (external+feedback) flux is such that the SQUID voltage is at an extremum, the first harmonic voltage response will be zero and any flux change will give a linear response. Negative feedback on the *dc* component of the flux is then used to keep the response zeroed: this feedback signal is linearly proportional to the flux threading the SQUID, with a constant of proportionality that can easily be determined with great precision. Traditionally the voltage signal from the SQUID has been amplified at low temperatures using a tuned *LC* circuit or a transformer, and at room temperature using phase sensitive lock-in detection. However, SQUID array amplifiers can also be used [47, 48]. These have the advantage of bandwidths of over 100 MHz, and no requirement for *ac* flux modulation.

For this review I will concentrate on high-spatial resolution magnetic microscopies. High spatial resolution is achieved by placing a small sensor close to the sample. In the case of SQUID microscopy this means making the SQUID small, or making a pickup loop integrated into the SQUID small. The scaling of the flux signal and spatial resolution with sensor size depends on the type of field source. For this review I will concentrate on three basic field sources: A point dipole \vec{m} generates the magnetic induction

$$\vec{B} = \frac{\mu_0}{4\pi} \frac{3\hat{r}(\hat{r} \cdot \vec{m}) - \vec{m}}{r^3}, \quad \text{Dipole field} \quad (7)$$

where \hat{r} is the direction and r is the magnitude of the vector between the dipole source and the point of interest. The magnetic flux Φ_s through a square area of side d oriented parallel to the xy plane and centered at $\vec{r} = z\hat{z}$ above a dipole at the origin with moment m oriented parallel to the z axis is given by

$$\Phi_s = \frac{2\mu_0 m d^2}{\pi \sqrt{d^2/2 + z^2} (d^2 + 4z^2)}. \quad \text{Dipole flux} \quad (8)$$

In the limit $z \rightarrow 0$ $\Phi_s \rightarrow 2\sqrt{2}\mu_0 m / \pi d$.

A superconducting vortex generates the induction

$$\vec{B} = \frac{\Phi_0}{2\pi r^2} \hat{r}, \quad \text{Monopole field} \quad (9)$$

where $\Phi_0 = h/2e$ is the total magnetic flux generated by the vortex. The magnetic flux Φ_s through a square area of side d oriented parallel to the xy plane and centered at

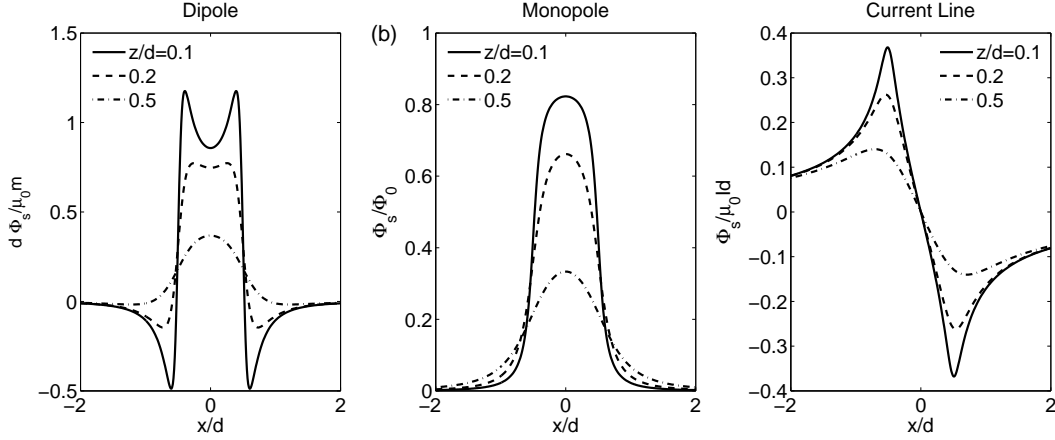


Figure 2. Plot of the flux through a square area of side d a height z above (a) dipole source with moment m oriented normal to the scan plane (b) a monopole source with flux Φ_0 , and (c) a line source with current I . For a given value of z/d the flux signal scales like d^{-1} for a dipole source, is independent of d for a monopole source, and scales like d for a current line source.

$\vec{r} = z\hat{z}$ above a vortex at the origin is given by

$$\Phi_s = \frac{2\Phi_0}{\pi} \tan^{-1} \left(\frac{d^2}{2z\sqrt{2d^2 + 4z^2}} \right). \quad \text{Monopole flux} \quad (10)$$

In the limit $z \rightarrow 0$ $\Phi_s \rightarrow \Phi_0$. Finally, an infinitely long and narrow line of current I in the \hat{y} direction at $x = 0, z = 0$ generates the field

$$\vec{B} = \frac{\mu_0 I}{2\pi r} \hat{\theta}, \quad \text{Current field} \quad (11)$$

where $\hat{\theta} = (x\hat{z} - z\hat{x})/r$. The magnetic flux Φ_s through a square area of side d oriented parallel to the xy plane at a height z above this line has peaks at $x = \pm\sqrt{d^2 + z^2}/2$ with magnitude

$$\Phi_s = \frac{\mu_0 Id}{4\pi} \ln \left[\frac{(d - \sqrt{d^2 + z^2})^2 + 4z^2}{(d + \sqrt{d^2 + z^2})^2 + 4z^2} \right] \quad \text{Current flux} \quad (12)$$

In the limit $z \rightarrow 0$ the magnetic fluxes at the peaks diverge logarithmically.

Figure 2 plots the calculated flux through a square area of side d , as a function of x , the lateral position of the SQUID relative to the field source, for various spacings z between pickup loop and sample, for these three different sources of field. For a given value of z/d for a dipole source the flux signal through the SQUID gets larger as d gets smaller, scaling like $1/d$. For a monopole source, such as a superconducting vortex, the peak flux is independent of d at constant z/d . For a line of current, the peak flux signal increases like d as the pickup loop diameter increases. In all cases the spatial resolution is about d for $z \ll d$.

Figure 3a plots the ratio of the peak flux at a sensor height z to the peak flux at $z/d = 0.1$ for the three different field sources, while Figure 3b plots the full width at half-maximum Δx for the dipole and monopole field sources, and the peak-to-peak distance for the current line source, as a function of sensor height z . The peak amplitude falls off nearly exponentially with sensor height for a dipole source, but falls off less quickly for a monopole or current line source. Similarly, the spatial resolution falls off quickly

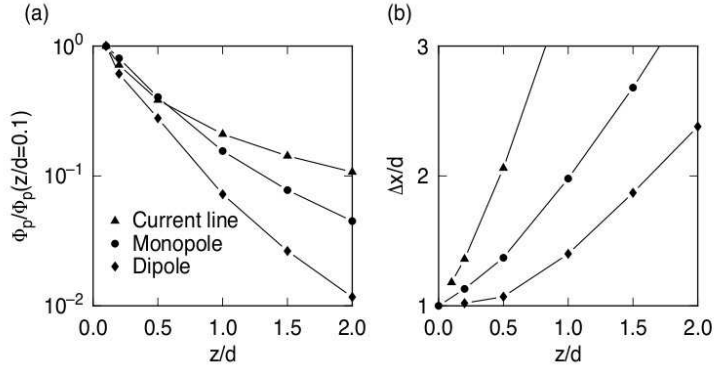


Figure 3. (a) Plot of the ratio of the flux through a square area of side d at a height z to that at a height $z/d = 0.1$ for various sources of field. (b) Full width at half-maximum for the dipole and monopole field sources, and the peak-to-peak distance for the current line source, of the flux through a square area of side d as a function of height z .

with sensor height for the dipole source, but less quickly for the monopole and current line sources.

The same qualitative conclusions can be made for more complex sources of field [49]. Consider a geometry in which the sample takes up a half-space $z < 0$. For the static case the magnetic fields in the half space $z > 0$ can be written as the gradient of a scalar potential φ_m : $\vec{B} = \vec{\nabla}\varphi_m$, where $\nabla^2\varphi_m = 0$. If we resolve the fields at the surface of the sample into Fourier components

$$\vec{b}_k(z=0) = \frac{1}{(2\pi)^2} \int_{-\infty}^{\infty} \int_{-\infty}^{\infty} \vec{B}(x, y, z=0) e^{i(k_x x + k_y y)} dx dy, \quad (13)$$

each of the components of the field for $z > 0$ will be of the form $\vec{b}_k(z) = \vec{b}_k(z=0)e^{-kz}$, where $k = \sqrt{k_x^2 + k_y^2}$: The fields will decay exponentially as z gets larger, with the higher Fourier components decaying more rapidly. Therefore to get optimal sensitivity and spatial resolution, the sensor must be placed close to the sample.

It was recognized almost immediately after the demonstration of the Josephson effect [50] and superconducting quantum interference effects [51] that local magnetic fields could be imaged by scanning samples and SQUIDs relative to each other [52]. However, it was not until 1983 that the first two-dimensional scanning SQUID microscope was built by Rogers and Bermon at IBM Research [53]. This instrument was used to image superconducting vortices in association with the IBM Josephson computer program. Other notable early efforts in SQUID microscopy were by the Wellstood group at the University of Maryland [54, 55, 56], the van Harlingen group at the University of Illinois [57, 58], the Wikswo group at Vanderbilt University [59], the Clarke group at U.C. Berkeley [60] and the Kirtley group at IBM Research [61, 62]. Kirtley and Wikswo [46] reviewed some of fundamentals and early work concerning scanning SQUID microscopy.

There are several competing strategies for achieving good spatial resolution in a SQUID microscope sensor. The first strategy is to make the SQUID very small (μ -SQUID), with narrow and thin constrictions for the Josephson weak links [63, 64]. This strategy has the advantage of simplicity, since only one level of lithography is required. The original μ -SQUIDs had hysteretic current-voltage characteristics. This meant that flux-locked-loop feedback schemes could not be used, and the flux sensitivity

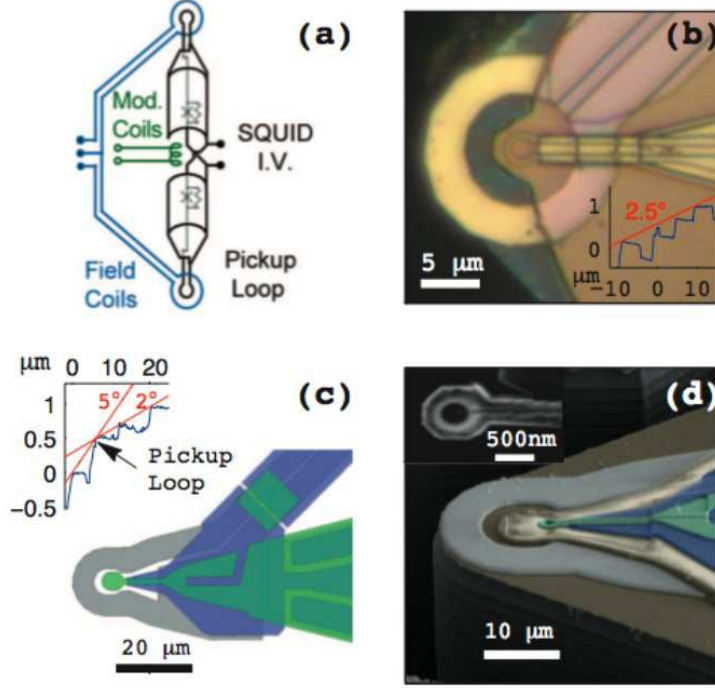


Figure 4. Advanced integrated scanning SQUID susceptometer design. (a) Diagram of a counterwound SQUID susceptometer. (b) Optical micrograph of pickup loop region of an optically defined SQUID susceptometer. The outer ring is the field coil and the inner ring is the flux pickup loop of the SQUID. The edge of the silicon substrate is just visible on the left side. The inset shows an atomic force microscopy cross-section of the structure along a horizontal line through the center of the pickup loop. The pickup loop is closest to the sample when the tip is aligned at a 2.5° angle. (c) Design for a SQUID sensor in which the pickup loop is defined using focussed ion beam (FIB) etching. In this case the pickup loop can touch down first if the alignment angle is between 2° and 5° . (d) Scanning electron microscopy images of the sensor after FIB definition of the pickup loop. Reprinted figure with permission from N.C. Koshnick, M.E. Huber, J.A. Bert, C.W. Hicks, J. Large, H. Edwards and K.A. Moler, *Appl. Phys. Lett.* **93**, 243101 (2008). Copyright 2008 by the American Institute of Physics.

of these SQUIDs was relatively poor. However, recently non-hysteretic, sub-micron sized SQUIDs have been made [65, 66, 67]. Hao *et al.* [67] made their SQUIDs non-hysteretic by using a second layer of tungsten to shunt them, and reported white noise floor levels of $0.2\mu\Phi_0/\text{Hz}^{1/2}$ in a SQUID with a diameter of about 370 nm.

A second strategy is a self-aligned SQUID recently reported by Finkler *et al.* [68]. In this work three aluminum evaporations are made onto a quartz tube that has been pulled into a sharp tip with apex diameter between 100 and 400 nm. The first two evaporations, performed at an angle of 100 degrees relative to the axis of the tube, form the leads. A third evaporation along the tip axis forms a ring with two weak links to the leads, forming a dc SQUID. Finkler *et al.* report non-hysteretic current-voltage characteristics and a flux sensitivity of $1.8 \times 10^{-6} \Phi_0/\text{Hz}^{1/2}$ for SQUIDs with an effective area of $0.34 \mu\text{m}^2$, operating at fields up to 0.6 T.

A third strategy is to make a more conventional SQUID, but to have well shielded superconducting leads to a small pickup loop integrated into it [69, 70, 62] (see Fig. 4).

This has the disadvantage of complexity, since multiple levels of metal are required to shield the pickup loop leads, but has the advantages of reduced interaction between the SQUID and the sample and ease of using flux feedback schemes. Figure 4 illustrates the properties of current advanced scanning SQUID sensor design using the integrated pickup loop strategy [71]. This SQUID sensor uses a Nb-AlO_x-Nb trilayer for the junctions, two levels of Nb for wiring and shielding, and SiO₂ for insulation between the various levels, as well as local field coils integrated into the pickup loop region, to allow local magnetic susceptibility measurements [69, 72]. High symmetry in the SQUID and field coil layout (see Fig. 4a) and tapered terminations are desirable to discriminate against background fields and reduce unwanted electromagnetic resonances [73]. Fig. 4b is an optical micrograph of a scanning SQUID susceptometer in which both the field coil and pickup loop were defined using optical lithography. Fig. 4c shows the layout for a device in which the pickup loop area is left as a “tab” in the optical lithography step, and then patterned into a loop using focussed ion beam lithography [74]. The completed device is shown in a scanning electron micrograph in Fig. 4d. This device uses a non-planarized process, meaning that each successive layer conforms to the topography of the previous one. This leads to constraints on the alignment angles that can be used to get the minimum spacing between pickup loop and sample, as illustrated in the insets in Fig. 4b,c. These constraints can be reduced by using a planarized process [75], in which the insulating layers are chemically-mechanically polished to planes before successive Nb wiring levels are added.

If we assume a SQUID or SQUID pickup loop diameter of $1\mu\text{m}$, a SQUID-sample spacing of $0.1\mu\text{m}$, and a SQUID noise level of $10^{-6}\Phi_0/\text{Hz}^{1/2}$, and using the peak signals from Fig. 2, we find a minimum detectable dipole signal of 139 electron spins/ $\text{Hz}^{1/2}$, a minimum flux signal of $1.25\times 10^{-6}\Phi_0/\text{Hz}^{1/2}$, and a minimum detectable line of current signal of $1.65\text{ nA}/\text{Hz}^{1/2}$.

2.2. Hall bar microscopy

A Hall bar develops a transverse voltage $V_x = -I_y B_z / n_{2d} e$ when a current I_y passes through it in the presence of a magnetic induction B_z perpendicular to the plane of the Hall bar [30, 31, 32], where n_{2d} is the carrier density per unit area of the Hall bar. Therefore materials with small carrier densities such as semi-metals, semi-conductors, or two-dimensional electron gases at the interface between semi-conductors with different bandgaps develop larger Hall voltages. Early scanning Hall bar systems used evaporated films of bismuth [76], InSb [77], or GaAs [78]. More recently high sensitivity and spatial resolution have been achieved with GaAs/Al_xGa_{1-x}As heterojunction structures [79, 80, 81, 82, 83, 84]. In addition, 250 nm sized scanning probes using GaSb/InAs/GaSb [83], and micron-scale Si/SiGe and InGaAs/InP Hall crosses have been characterized at low temperatures [85, 86]. Hicks et al. [87] have fabricated Hall bars as small as 85 nm on a side (see Fig. 5) from GaAs/Al_xGa_{1-x}As heterojunction electron gas material, and estimate a field noise of $500\mu\text{T}/\text{Hz}^{1/2}$ and a spin sensitivity of $1.2\times 10^4\mu_B/Hz^{1/2}$ at 3 Hz and 9K for sensors 100 nm on a side. Sandhu *et al.* have fabricated 50 nm bismuth Hall bar sensors with a noise of $0.8\text{G}/Hz^{1/2}$ [88]. At present Hall bars from GaAs/Al_xGa_{1-x}As heterojunctions are less sensitive above about 100 K because of thermal excitations. Scanning Hall bar sensors made of InAs have been used to image single magnetic biomolecular labels at room temperature [89].

Magnetic tunnel junctions and Hall bars in the ballistic regime [90, 91, 92] produce a signal which is proportional to $\langle B_z \rangle$, the magnetic field perpendicular to the sensor, averaged over the sensor. The situation is more complicated for a Hall bar in

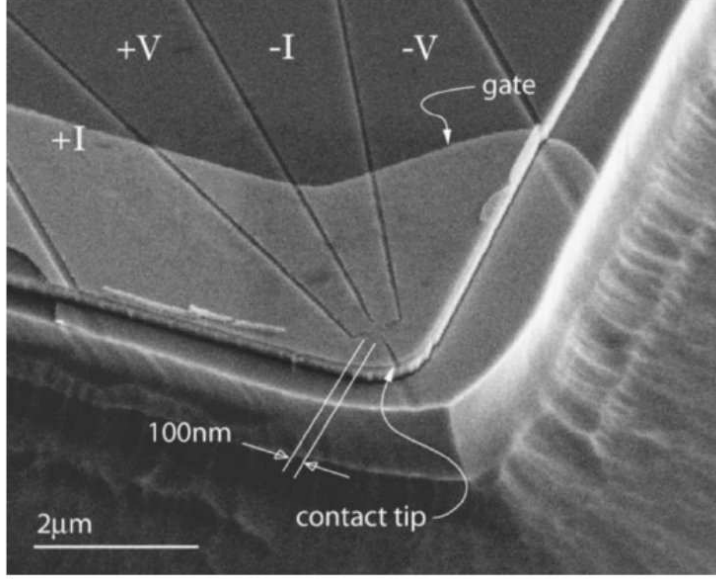


Figure 5. Scanning electron microscope image of a 100 nm Hall probe. The four leads are separated by narrow etch lines. The gate shields the Hall cross from stray electrical charges and allows the modulation of the 2DEG beneath. The Hall probe will touch the sample surface at the contact tip. Reprinted figure with permission from C.W. Hicks, L. Luan, K.A. Moler, E. Zeldov, and H. Shtrikman, *Appl. Phys. Lett.* **90**, 133512 (2007). Copyright 2007 by the American Institute of Physics.

the diffusive regime [93], but may be qualitatively similar. The average fields $\langle B_z \rangle$ for the three sources of field can be inferred from Eq.s 8, 10 and 12 (Fig. 2), by substituting $\Phi_s \rightarrow \langle B_z \rangle d^2$ and in Fig. 3 by substituting $\Phi_p \rightarrow \langle B_z \rangle_p$, where $\langle B_z \rangle_p$ is the peak value of the field averaged over the sensor area. For a given value of z/d , $\langle B_z \rangle$ is proportional to $1/d^3$ for a dipole source, proportional to $1/d^2$ for a monopole source, and proportional to $1/d$ for a line of current source. Boero *et al.* [94] estimate that the optimal Johnson noise limited minimum detectable magnetic field in a micro-Hall cross geometry is given by

$$B_{min} \approx \frac{\sqrt{4k_B T R_0}}{v_{sat} w} \quad \text{Thermal} \quad (14)$$

where k_B is Boltzman's constant, T is the operating temperature, R_0 is the output resistance at zero magnetic field, v_{sat} is the saturation carrier drift velocity, and w is the width of the cross. This results in $B_{min} \sim 2nT/\sqrt{Hz}$ for $w=1\mu\text{m}$ at 300K for doped InSb. Thermal noise is expected to be independent of sensor size, and therefore the scaling for sensitivity is the same as for $\langle B_z \rangle$. At the low temperatures used for imaging superconductors, transport in the Hall sensor is often quasi-ballistic and the signal-to-noise is better characterized by a mobility and an optimum probe current. The latter is typically defined as the maximum current before the onset of pronounced $1/f$ noise due to one of several possible sources, e.g., generation-recombination noise at deep traps or across heterointerfaces, heating or impact ionization. However, noise in micron scale Hall bars is often dominated by $1/f$ noise [92, 87]. The minimum detectable field can then be written as [89]

$$B_{min} \approx \frac{1}{\mu d} \sqrt{\frac{\alpha_H G_N \Delta f}{n f}}, \quad 1/f \quad (15)$$

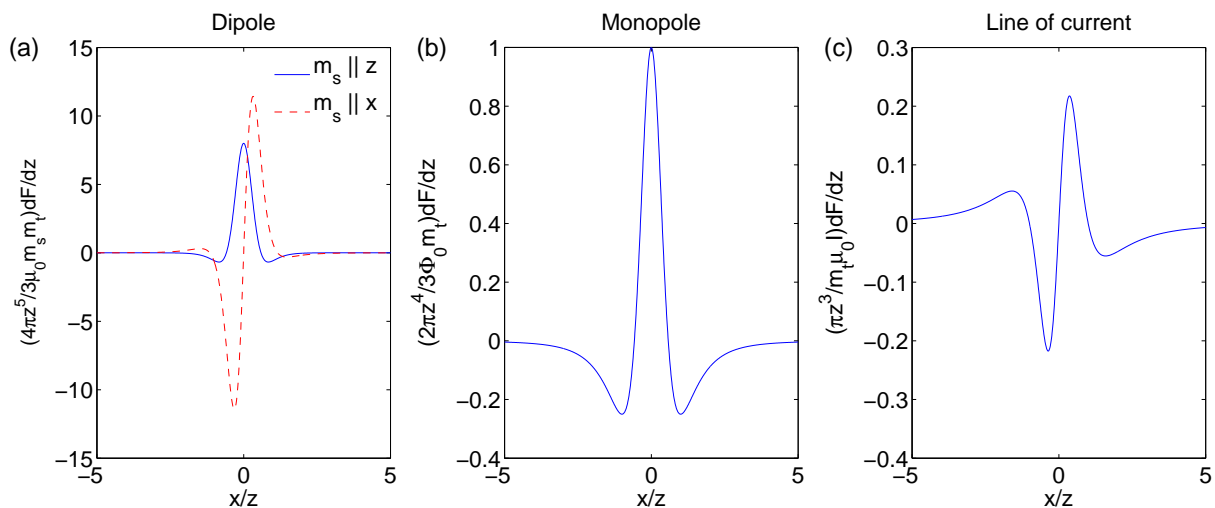


Figure 6. MFM modeling using the point dipole tip approximation: Force derivative curves for (a) a dipole source located at the origin with magnetic moment m_s oriented parallel to z (solid line) or parallel to x (dashed line), Eq. 7, (b) a monopole source located at the origin with magnetic flux Φ_0 , Eq. 9, and (c) a line of current I along the y axis, Eq. 11. The tip is modeled as a point dipole with moment m_t oriented parallel to the z -axis scanning a height z above the xy plane along the x axis (Eqn.'s 17).

where μ is the mobility, d is the sensor size, α_H is Hooge's $1/f$ noise parameter, $G_N \sim 0.325$ is a constant, n is the carrier density, Δf is the measurement bandwidth, and f is the frequency. Eq. 15 combined with Eq.'s 8, 10, and 12 imply that for a Hall bar dominated by $1/f$ noise, for a given z/d the minimum detectable dipole moment scales like d^2 , the minimum detectable flux scales like d , and the minimum detectable current is independent of d . It has been reported that low frequency noise in Hall bar devices can be significantly reduced by optimizing the voltage on a gate over the Hall cross [95, 87] and that sufficiently small devices have noise which is composed of a single Lorentzian spectrum [96].

2.3. Magnetic force microscopy

A magnetic force microscope [97, 98, 99] images small changes in the resonance frequency of a cantilever due to the interaction between magnetic material on a sharp tip at the end of the cantilever and local sample magnetic fields. The signal from a magnetic force microscope is proportional to $dF_{tip,z}/dz$, the derivative of the z -component of the force on the tip with respect to its z -position. Since this force sums contributions from all the magnetic material in the tip, the sensitivity and spatial resolution of MFM depends on the shape of the tip. For some applications and tip materials the tip can be modeled as having a magnetic monopole at its apex, with the force approximated by $F_{tip,z} = qB_z$, where q is the effective magnetic *monopole* moment of the tip [100, 32]. However, Lohau *et al.* have shown that their experimental MFM data can be modeled either using a monopole or a dipole approximation for the end of the tip, but that in either case the effective position of the monopole or dipole is a function of the field gradient from the sample [101].

It is instructive to model the ultimate spatial resolution and sensitivity of an MFM in the point monopole and dipole approximations for the tip. The z -component of the

force derivative on the tip from a field source can be written as [101]

$$\frac{\partial F_z}{\partial z} = -\frac{q}{\mu_0} \frac{\partial B_z}{dz} + m_{t,x} \frac{\partial^2 B_x}{\partial z^2} + m_{t,y} \frac{\partial^2 B_y}{\partial z^2} + m_{t,z} \frac{\partial^2 B_z}{\partial z^2}, \quad (16)$$

where q is the magnetic monopole flux, and $m_{t,i}$ are the dipole moments of the tip in the x, y, z directions. Assume for simplicity that the tip is magnetized only in the z -direction. Then $m_{t,x} = m_{t,y} = 0$ and the force derivatives due to the dipole, monopole, and current line sources of Eq.'s 7, 9, and 11 are given by

$$\begin{aligned} \frac{\partial F_z}{\partial z} &= \frac{3m_{t,z}\mu_0}{4\pi r^9} \left[-5(m_{s,x}x + m_{s,y}y)z(3r^2 - 7z^2) \right. \\ &\quad \left. + m_{s,z}(3r^4 - 30r^2z^2 + 35z^4) \right] \quad \text{Dipole - dipole} \\ &= \frac{3\Phi_0 m_{t,z} z}{2\pi} \frac{5z^2 - 3r^2}{r^7} \quad \text{Dipole - Monopole} \\ &= -\frac{m_{t,z}\mu_0 I x}{\pi} \frac{x^2 - 3z^2}{(x^2 + z^2)^3} \quad \text{Dipole - Current line} \end{aligned} \quad (17)$$

where $m_{t,z}$ is the dipole moment of the tip.

Similarly, the expressions for the force derivative in the monopole approximation are given by:

$$\begin{aligned} \frac{\partial F_z}{\partial z} &= -\frac{3q}{4\pi r^7} \left[(xm_{s,x} + ym_{s,y})(r^2 - 5z^2) \right. \\ &\quad \left. + m_{s,z}z(3r^2 - 5z^2) \right] \quad \text{Monopole - dipole} \\ &= -\frac{q\Phi_0}{2\pi\mu_0} \frac{r^2 - 3z^2}{r^5} \quad \text{Monopole - Monopole} \\ &= \frac{qI}{\pi} \frac{xz}{(x^2 + z^2)^2} \quad \text{Monopole - Current line} \end{aligned} \quad (18)$$

The force derivative relations given by Eq.'s 17 and 18 are plotted in Figures 6 and 7 respectively.

Within these approximations the force derivative signal strength increases strongly with decreasing z - like $1/z^5$ for a dipole source, $1/z^4$ for a monopole source, and $1/z^3$ for a current line source, in the point dipole tip approximation. In the monopole tip approximation the powers are $1/z^4$, $1/z^3$, and $1/z^2$ for the three sources, respectively. The widths of the predicted force derivative features are proportional to the height z of the tip above the source. The constant of proportionality does not depend strongly on source: the full width at half-maximum (or distance between the maximum and minimum force derivative for a line of current source) is $\Delta x/z=0.6, 0.66,$ and 0.74 for the dipole tip, and $0.74, 1,$ and 1.16 for the monopole tip, for the three sources respectively. Of course, these conclusions would be modified for a real tip with a finite size. It has been estimated that the effective tip-sample spacing and radius of curvature for conventional MFM tips are both about 10 nm [100].

In order to estimate the sensitivity of MFM, one needs to know the minimum detectable force derivative, which depends on a number of characteristics of the MFM, including those of the cantilever. Using the lumped mass model for an MFM cantilever, the equation of motion of the tip end position z is that of a driven, damped harmonic oscillator

$$m \frac{d^2 z}{dt^2} + \Gamma \frac{dz}{dt} + kz = F_{\text{signal}}(t) + F_{\text{thermal}}(t), \quad (19)$$

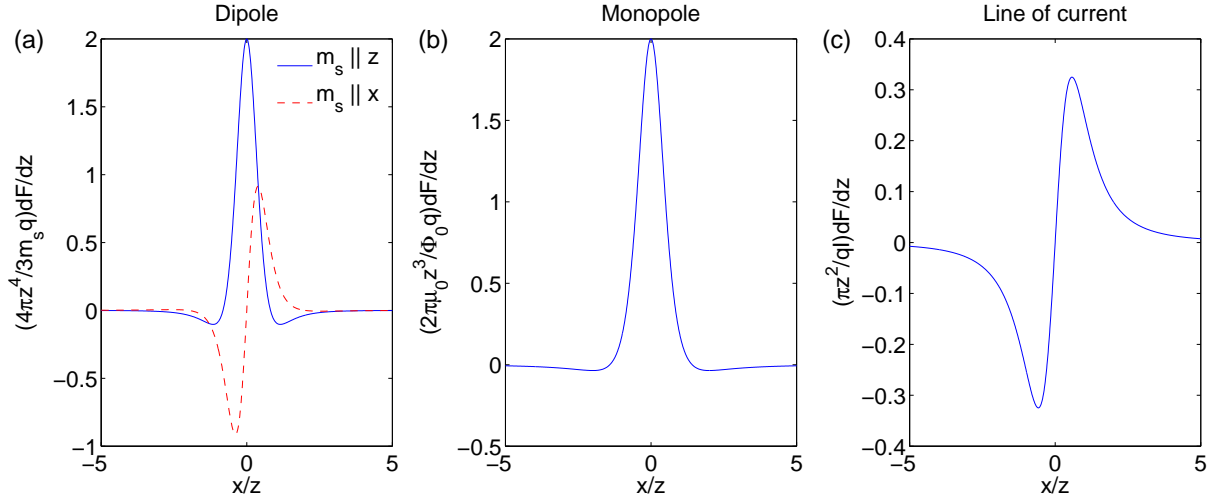


Figure 7. MFM modeling using the monopole tip approximation: MFM force derivative curves for (a) a dipole source located at the origin with magnetic moment m_s oriented parallel to z (solid line) or parallel to x (dashed line), Eq. 7, (b) a monopole source located at the origin with magnetic flux Φ_0 , Eq. 9, and (c) a line of current I along the y axis, Eq. 11. The tip is modeled as a point monopole with magnetic flux q scanning along the x axis a height z above the xy plane (Eqn.s 18).

where m is the effective mass of the cantilever, $\Gamma = k/\omega_0 Q$ is the damping constant, k is the cantilever spring constant, ω_0 is the angular resonant frequency, Q is the quality factor, F_{signal} is the signal force (in this case the magnetic interaction between the tip and sample), and F_{thermal} is the force due to thermal fluctuations. The equipartition theorem implies that the power spectral density of thermal fluctuations $S_F = 4\Gamma k_B T$. Then the thermally limited minimum detectable force derivative is given by

$$\frac{\partial F}{\partial z}_{\min} = \frac{1}{A} \sqrt{\frac{4k k_B T B W}{\omega_0 Q}}, \quad (20)$$

where BW is the measurement bandwidth and A is the amplitude of oscillation of the cantilever.

A major thrust in research in MFM is to reduce the spatial extent of the magnetic material in the cantilever tip to improve spatial resolution and spin sensitivity. This is often done by shaping previously deposited material using focussed ion beam etching [102, 103]. Sharply defined magnetic tips can also be produced by evaporating magnetic material on an electron beam deposited carbon and ion etched needle [104], or onto a carbon nanotube [105] at the end of a conventional Si cantilever tip (see Figure 8). Small amounts of magnetic material can also be deposited directly onto cantilever tips through nanoscale holes fabricated in a stencil mask [106]. One approach would be to place nano-magnets directly on the apex of cantilever tips. This would serve three goals: improved spatial resolution, improved spin sensitivity, and improved interpretability, since the magnetic moment of the deposited nano-magnets would have a narrow distribution [107]. However, such tips could be especially susceptible to switching of the tip moment in sufficiently strong magnetic fields, reversing the contrast of the MFM images [108]. Although this complicates the interpretation of the images, the tip magnetization state is also known better, since the tip is generally close to saturation either up or down except for a narrow window around the switching points. The tip in MFM exerts a relatively strong magnetic field, comparable to the saturation magnetization of the

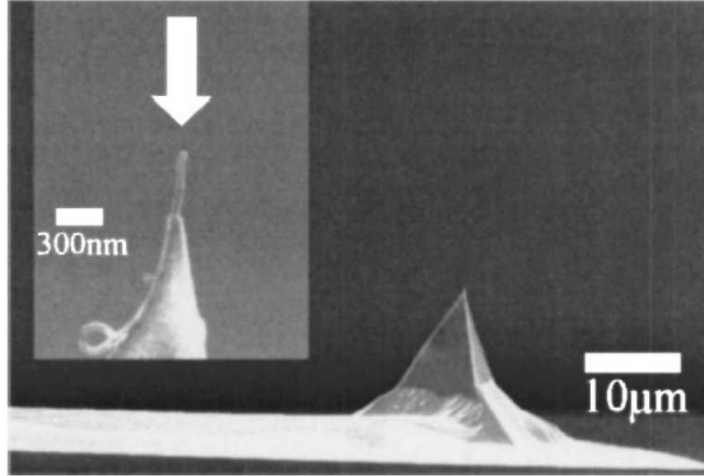


Figure 8. Scanning electron microscope (SEM) image of a MFM cantilever. Insert upper left: high-resolution SEM image of the apex of the pyramid, where a coated carbon nanotube tip (CCNT) is visible. The arrow shows the direction of the metal evaporation. Reprinted figure with permission from Z. Deng, E. Yenilmez, J. Leu, J.E. Hoffman, E.W.J. Straver, H. Dai, and K.A. Moler, *Appl. Phys. Lett.* **85**, 6263 (2004). Copyright 2004 by the American Institute of Physics.

magnetic material used in the tip, on the sample. This can cause switching of the local magnetic moment of the sample [109], but can also be taken advantage of for vortex manipulation studies (see Section 3.5).

Assume for the moment that it will be possible to locate small nanoparticles at the end of an MFM cantilever tip. A 7 nm diameter cobalt nanoparticle will have a total dipole moment of $m_t = 2.5 \times 10^{-19} \text{ A} \cdot \text{m}^2$, assuming a magnetization of $M = 1.4 \times 10^6 \text{ A/m}$ [110]. Taking values of $Q=50,000$, $\omega_0=2\pi \times 50 \text{ kHz}$, $A=1 \text{ nm}$, $k=2\text{N/m}$, and $T=4\text{K}$, the thermally limited force gradient is $\partial F/\partial z|_{\min}=1.7 \times 10^{-7} \text{ N/m}$. Using the dipole approximation for the tip, the peak force due to a sample dipole m_s with both tip and sample moments oriented parallel to the z axis is given by (Eq. 17, Fig. 6) $\partial F/\partial z_{\text{peak}} = 24\mu_0 m_s m_t / 4\pi z^5$. Using $z=15 \text{ nm}$ results in a minimum detectible sample moment of 23 Bohr magnetons. From Fig. 6 the full width at half maximum of the force derivative response would be $\Delta x = 0.6z = 9\text{nm}$.

2.4. Summary

Each of the three techniques described here has advantages and disadvantages: MFM has the best spatial resolution ($\sim 10\text{-}100 \text{ nm}$), SSM the worst ($\sim 0.3\text{-}10 \mu\text{m}$), with Hall bars intermediate ($\sim 0.1\text{-}5 \mu\text{m}$). The relative sensitivities of the three techniques depend on the type of field source. As in all microscopies there are tradeoffs between sensitivity and spatial resolution. The spatial resolution for SQUIDs and Hall bars is roughly given by $\Delta x \approx d$ for heights $z \ll d$, where d is the sensor size (Fig.'s 2, 3). For MFM the spatial resolution is roughly set by the tip-sample spacing z , in the limit where the radius of curvature of the tip end is smaller than z (Fig.'s 7,6). The flux sensitivity of SQUIDs is nearly independent of SQUID or pickup loop size, so the field sensitivity is roughly proportional to the inverse of the pickup loop or SQUID area. With Hall bars limited by thermal noise the field sensitivity is independent of sensor size, but Hall

bars dominated by $1/f$ noise are expected to have a field sensitivity that scales like $1/d$. Current MFM's measured field gradients, rather than fields, and the tradeoff between sensitivity and spatial resolution is less clear than for SSM and SHM, although larger amounts of magnetic material will produce larger sensitivity but will require a larger tip volume, reducing resolution. Table 1 compares sensitivity and spatial resolution for a state of the art SQUID, with a pickup loop $0.6\mu\text{m}$ in diameter and a flux noise of $0.7\times 10^{-6}\Phi_0/Hz^{1/2}$ (Figure 4 [71]), a state of the art Hall bar with sensor size 100 nm and a field noise of $500\mu\text{T}/Hz^{1/2}$ at 3 Hz (Fig. 5 [87], and a hypothetical MFM with a 7 nm Co nanoparticle at the tip as discussed in Section 2.3. These numbers should be treated with a great deal of caution. For example, I have assumed that $z/d = 0.1$ for the SQUID and SHM, and $z=15$ nm for the MFM. These may be unreasonably optimistic estimates. However, the Table 1 does indicate how relative sensitivities depend on the field source. As an example, SSM and MFM have roughly comparable spin sensitivities, but SSM has nearly two orders of magnitude better sensitivity for a monopole source, and nearly 4 orders of magnitude better sensitivity for a line of current source.

Table 1. Sensitivities and spatial resolutions

	Dipole		Monopole		Line of current	
	$N(\mu_B/\sqrt{Hz})$	$\Delta x(\text{nm})$	$\Phi(\Phi_0/\sqrt{Hz})$	$\Delta x(\text{nm})$	$I(\text{A}/\sqrt{Hz})$	$\Delta x(\text{nm})$
MFM	23	9	3.4×10^{-5}	10	2.6×10^{-5}	11
SHM	4.5×10^4	100	3×10^{-3}	108	1.14×10^{-4}	118
SSM	78	600	8.8×10^{-7}	650	5.5×10^{-9}	710

Table 2 provides a summary of the scaling exponents n for the minimum detectable field sources for SSM, SHM, and MFM. In this table the minimum detectable dipole moment, flux, and current are proportional to d^n for SSM and SHM, while for MFM these quantities are proportional to z^n . For SSM and SHM it is assumed that z/d is held constant. For SSM it is assumed that thermal noise dominates. There are two columns for SHM, for noise dominated by thermal fluctuations, or by $1/f$ noise. For MFM there are two columns, for the monopole and the dipole tip approximations.

Table 2. Scaling exponents n

	SSM	Hall	Hall	MFM	MFM
		1/f	thermal	monopole	dipole
Line of current	-1	0	1	2	3
Monopole	0	1	2	3	4
Dipole	1	2	3	4	5

There are further considerations in deciding which magnetic microscopy is best for a given application: SSM requires a cooled sensor, about 9K for the most technically advanced Nb SQUIDs, although Hall bars and MFM also have the highest sensitivities at low temperatures. SSM is the most straightforward to calibrate absolutely. Hall bars tend to be mechanically delicate and the most sensitive to destruction by electrostatic discharge. MFM applies the largest fields to the sample. In general Hall bars and MFM can tolerate larger applied magnetic fields than SQUIDs. As we shall see in Section 3, each has been very useful in the study of superconductors.

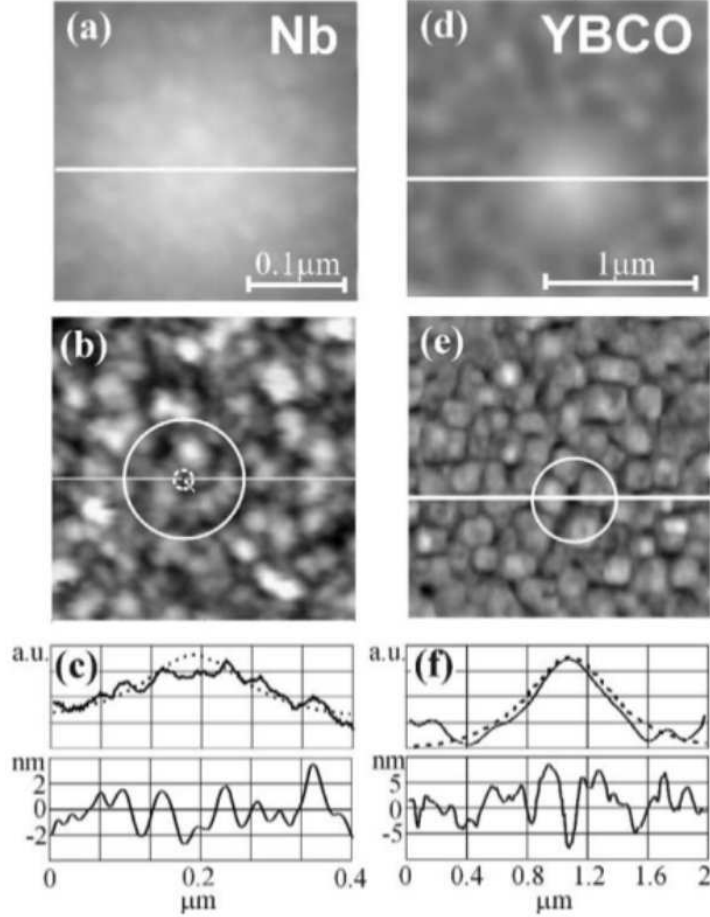


Figure 9. (a) Magnetic force microscope image of $0.3 \mu\text{m} \times 0.3 \mu\text{m}$ areas for a Nb film and the corresponding topographic image (b). (d) MFM image of a single vortex ($2 \times 2 \mu\text{m}^2$) in a YBCO film and (e) the corresponding topographic image. The white circles in (b) and (e) correspond to the distance at which the stray field emanating from the vortex has decreased to $1/e$ of its maximum value. The small dotted circle in (b) defines an area with diameter $2\xi \approx 22 \text{ nm}$. The lower panels (c) and (f) are cross-sections of the MFM data and the topography profiles along the white lines indicated in (a), (b), (d), and (e). The dotted curves correspond to a Gaussian profile fitting of the MFM signal after filtering with a low-pass filter. Reprinted figure from *Physica C: Superconductivity* **369**, A. Volodin, K. Temst, Y. Bruynseraede, C. van Haesendonck, M.I. Montero, I.K. Schuller, B. Dam, J.M. Huijbregtse and R. Griessen, “Magnetic force microscopy of vortex pinning at grain boundaries in superconducting thin films”, P. 165-170 (2002), with permission from Elsevier.

3. Applications

3.1. Static imaging of magnetic flux

Understanding the trapping of vortices in superconductors is of crucial technological importance, both because vortex pinning is the primary mechanism for enhanced critical currents in type II superconductors [111], and also because trapped vortices are an important source of noise in superconducting electronic devices. Superconducting vortices are especially easy to image using magnetic imaging because they are highly localized, quantized, and have relatively large magnetic fields. A number of different

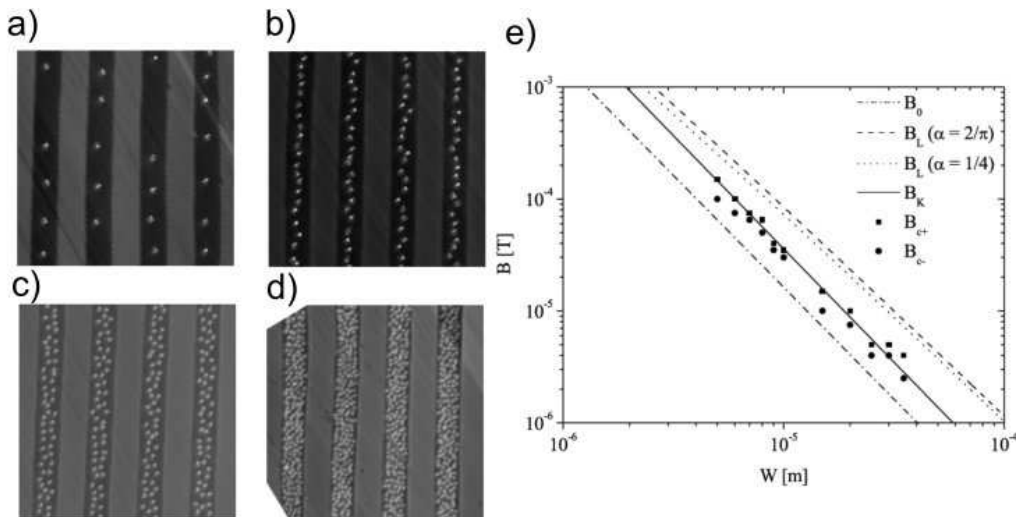


Figure 10. SQUID microscope images of $35 \mu\text{m}$ wide YBCO thin film strips cooled in magnetic inductions of (a) 5, (b) 10, (c) 20, and (d) $50 \mu\text{T}$. e) Critical inductions for vortex trapping in YBCO thin films as a function of strip width. The squares (B_{c+}) represent the lowest induction in which vortices were observed, and the dots (B_{c-}) are the highest inductions for which vortex trapping was not observed. The dashed-dotted line is the metastable critical induction B_0 [Eq. 23] [120], the short-dashed and long-dashed lines are B_L [Eq. 22], the critical induction calculated using an absolute stability criterion, and the solid line is B_K [Eq. 24], calculated using a dynamic equilibrium criterion between thermally activation and escape for vortices. Reprinted figure with permission from K.H. Kuit, J.R. Kirtley, W. van der Veur, C.G. Molenaar, F.J.G. Roesthuis, A.G.P. Troeman, J.R. Clem, H. Hilgenkamp, H. Rogalla, and J. Flokstra, Phys. Rev. B **77**, 134504 (2008). Copyright 2008 by the American Physical Society.

techniques have been used for imaging superconducting vortices, including SSM, SHM, and MFM. MFM has the advantage for this application that it can image both the vortex magnetic fields and sample topography simultaneously, so that macroscopic pinning sites can be identified. It has been used for a number of years to image superconducting vortices [112, 113, 114, 115, 116, 117, 118, 119]. Care must be taken however, because the large magnetic fields exerted by the tip can distort and dislodge vortices. As we will see in Section 3.5, this can also be an advantage. An particularly striking example of simultaneous magnetic and topographic imaging of vortices in Nb and YBCO is shown in Figure 9 [113].

3.1.1. Narrow strips The sensitivity of high- T_c superconducting sensors such as SQUIDs and hybrid magnetometers based on high- T_c flux concentrators is limited by $1/f$ noise. One source of this noise is the movement of vortices trapped in the sensor. One technique for reducing this source of noise is to trap vortices at a distance from the sensitive regions of the superconducting circuitry using holes or motes [121, 122]. Jeffery *et al.* [123] used a scanning SQUID microscope to image flux trapping in superconducting electronic circuitry with motes. Veauvy *et al.* [124] studied vortex trapping in regular arrays of nanoholes in superconducting aluminum. Noise from trapped vortices in high- T_c SQUID washers and flux concentrators can be eliminated by dividing the high- T_c body into thin strips [125, 126]. Below a critical magnetic induction no vortex trapping occurs in these strips for a given strip width. A number of models for

the critical inductions of thin-film strips have been proposed [127, 120, 128, 129]. Indirect experimental testing of these models was done by observing noise in high- T_c SQUIDS as a function of strip width and induction [125, 126, 130]. More direct experimental verification of these models was presented by Stan *et al.* [131] using scanning Hall probe microscopy on Nb strips and Suzuki *et al.* [132] using SQUID microscopy on $\text{NdBa}_2\text{Cu}_3\text{O}_y$ thin-film patterns with slots. Both experiment and theory found that the critical magnetic induction varied roughly as $1/W^2$, where W is the strip width. However, the experimental [131] and theoretical [120, 127] pre-factors multiplying this $1/W^2$ dependence differ significantly.

Figure 10a-d shows SQUID microscope images of $35\mu\text{m}$ wide YBCO strips cooled in various magnetic inductions. Fig. 10e plots B_{c+} , the lowest induction at which vortices are trapped in the strips (squares), and B_{c-} , the highest induction at which vortices are not trapped (dots) as a function of strip width. The lines represent various theoretical predictions.

The Gibbs free energy for a vortex in a superconducting strip of width W in an applied induction B_a perpendicular to the strip plane can be written as [133]:

$$G(x) = \frac{\Phi_0^2}{2\pi\mu_0\Lambda} \ln \left[\frac{\alpha W}{\xi} \sin \left(\frac{\pi x}{W} \right) \right] \mp \frac{\Phi_0(B_a - n\Phi_0)}{\mu_0\Lambda} x(W - x), \quad (21)$$

where $\Lambda = 2\lambda^2/d$ is the Pearl length of the strip, λ is the London penetration depth, α is a constant of order 1, n is the areal density of vortices, ξ is the coherence length, and x is the lateral position of the vortex in the strip. The critical induction model of Likharev [127] states that in order to trap a vortex in a strip the vortex should be absolutely stable: the critical induction then happens when the Gibbs free energy in the middle of the strip is equal to zero, and leads to

$$B_L = \frac{2\Phi_0}{\pi W^2} \ln \left(\frac{\alpha W}{\xi} \right). \quad (22)$$

This is plotted as the dashed and dotted lines in Fig. 10 for two assumed values of α . A second model, proposed by Clem [120] considers a metastable condition, in which the induction is just large enough to cause a minimum in the Gibbs energy at the center of the strip, $d^2G(W/2)/dx^2 = 0$, leading to

$$B_0 = \frac{\pi\Phi_0}{4W^2}. \quad (23)$$

This is plotted as the dot-dashed line in Fig. 10. Finally, Kuit *et al.* proposed that the critical induction should result from a dynamic equilibrium between vortex thermal generation and escape. This leads to the critical induction

$$B_K = 1.65 \frac{\Phi_0}{W^2}. \quad (24)$$

It can be seen in Figure 10 that the dynamic equilibrium model (solid line) fits the data the best of the three models, with no fitting parameters. Kuit *et al.* also found that n , the areal density of trapped vortices, increased linearly with applied induction above the critical value, in agreement with the dynamic equilibrium model, and that the trapping positions showed lateral ordering, with a critical field for formation of a second row that was consistent with a numerical prediction of Bronson *et al.* [134]. Similar good agreement between experiment and the dynamic equilibrium model was found by the same authors for Nb thin film strips.

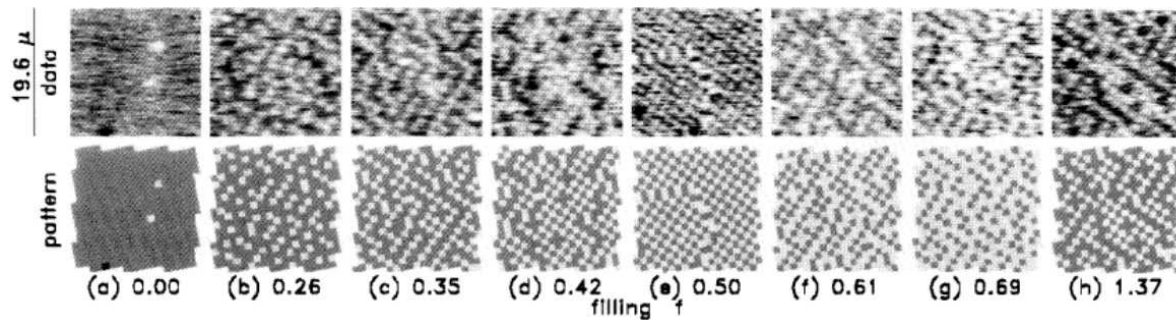


Figure 11. Top row: Scanning Hall probe microscopy images of vortex configurations in square areas $19.6 \mu\text{m}$ on a side in a superconducting Nb wire grid of $0.95 \mu\text{m} \times 0.95 \mu\text{m}$ square holes, at the filling fractions f indicated. The second row shows maps of the positions in the grid occupied by vortices. Note the ordering observed near $f = 1/3$ (c), $f = 1/2$ (e), and $f = 4/3$ (h). Reprinted figure with permission from H.D. Hallen, R. Seshadri, A.M. Chang, R.E. Miller, L.N. Pfeiffer, K.W. West, C.A. Murray, and H.F. Hess, Phys. Rev. Lett. **71**, 3007 (1993). Copyright 1993 by the American Physical Society.

3.1.2. Superconducting wire lattices, clusters, and nano-hole arrays Two dimensional arrays of Josephson junctions [135, 136, 137, 138, 139, 140] have been studied extensively, not only because they offer the possibility of studying Kosterlitz-Thouless effects [141] in an ordered 2-dimensional system, but also because of interesting effects that were predicted [142] and observed [135, 136] to occur when the applied field is a rational fraction of the field required to populate each cell with a quantum of magnetic flux. Scanning magnetic microscopy has been used extensively for studying vortex trapping in two-dimensional superconducting wire networks [143, 58], clusters [58], and ring arrays [144, 145]. Superconducting wire networks are of interest because they are a physical realization of a frustrated xy model [146, 142, 147], where the variable is the phase of the superconducting order parameter. The filling fraction f of vortices/site can be varied by cooling the network in various fields, and detailed predictions have been made for the ground state vortex configurations at rational f fractions [148]. Studies of these systems were at first performed using transport [149, 150, 151, 152], but direct imaging of the vortex positions provides more detailed information. Runge *et al.* did magnetic decoration experiments on superconducting wire lattices [153]. Although these experiments provided direct information on the vortex positions, only one set of conditions, such as magnetic field and temperature, can be explored for each sample using this technique. An example of scanning Hall bar microscopy on a superconducting wire network is shown in Figure 11 [143]. In this figure ordered vortex arrangements can be seen near the fractional filling factors of $f=1/3$, $1/2$, and $4/3$, as predicted by Teitel and Jayaprakash [146, 142], along with grain boundaries between ordered domains and vacancies.

Field *et al.* [154] studied vortex trapping in Nb films with large arrays of $0.3\mu\text{m}$ holes on a square lattice. They found strong matching effects when the cooling fields corresponded to one or two vortices per site, as well as at several fractional multiples of the matching field. They also observed striking domain structure and grain boundaries between the domains.

3.1.3. Half-integer flux quantum effect The discovery in 1986 of superconductivity at high temperatures in the cuprate perovskites [2, 3] generated enormous excitement.

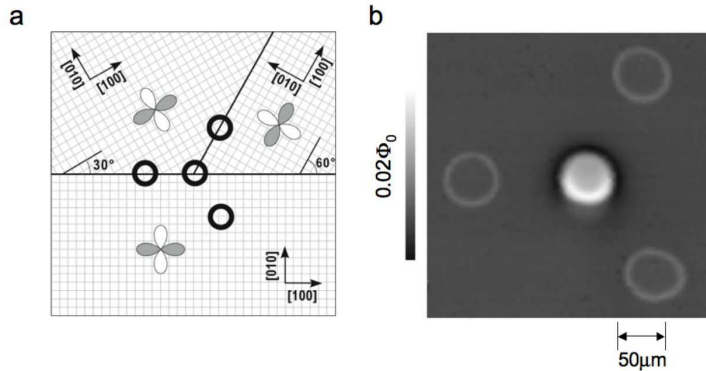


Figure 12. (a) Schematic diagram for the tricrystal (100) SrTiO₃ substrate used in the phase sensitive pairing symmetry tests of Tsuei *et al.* [61]. Four epitaxial YBa₂Cu₃O_{7- δ} thin film rings are interrupted by 0, 2, or 3 grain boundary Josephson weak links. (b) Scanning SQUID microscopy image of the four superconducting rings in (a), cooled in a field <5 mG. The central ring has $\Phi_0/2$ magnetic flux, where Φ_0 is the superconducting flux quantum, spontaneously generated in it. The other 3 rings, which have no spontaneously generated flux, are visible through a small change in the self-inductance of the SQUID when passing over the superconducting walls of the rings.

Although there was a great deal of evidence that the superconducting gap in the cuprates was highly anisotropic, with a significant density of states at low energies [155, 156], phase sensitive measurements [157, 158] were required to distinguish, for example, d -wave from highly anisotropic s -wave pairing symmetry. The first such experiments [159, 160] used the magnetic field dependence of the critical current in single junctions and 2-junction SQUIDs between single crystals of YBa₂Cu₃O_{7- δ} (YBCO) and Pb to demonstrate a π -phase shift between the component of the superconducting pairing order parameter perpendicular to adjacent in-plane crystal faces (*e.g.*, ignoring the effects of twinning, between the a vs b axis normal faces) of the YBCO. Similar phase sensitive Josephson interference experiments were performed by Brawner *et al.* [161], Iguchi *et al.* [162], Miller *et al.* [163] and Kouznetsov *et al.* [164].

A phase-sensitive technique for determining pairing symmetry that is complementary to Josephson interference is to image magnetic fields generated by spontaneous supercurrents in superconducting rings that have an odd number of intrinsic π -phase shifts in circling them, or in Josephson junctions that have intrinsic π -shifts along them [165, 166]. The first such experiments were done by Tsuei *et al.* [61], using YBCO films grown epitaxially on tricrystal SrTiO₃ substrates. A scanning SQUID microscope was used to image the magnetic fields generated by supercurrents circulating rings photolithographically patterned in the YBCO films. In the original experiments the central ring (Fig. 12), which has 3 grain boundary Josephson junctions, has either 1 or 3 intrinsic π -phase shifts for a superconductor with predominantly $d_{x^2-y^2}$ pairing symmetry, and should therefore have states of local energy minima, when no external magnetic field is applied, with the total flux through the ring of $\Phi = (n + 1/2)\Phi_0$, n an integer, for sufficiently large LI_c products, where L is the inductance of the ring, and I_c is the smallest critical current of the junctions in the ring. This is the half-integer flux quantum effect. The two outer rings that cross the tricrystal grain boundaries have 0 or 2 intrinsic π -phase shifts for a $d_{x^2-y^2}$ superconductor, and should therefore have local energy minima at $\Phi = n\Phi_0$ - conventional flux quantization. Similarly, the ring that does

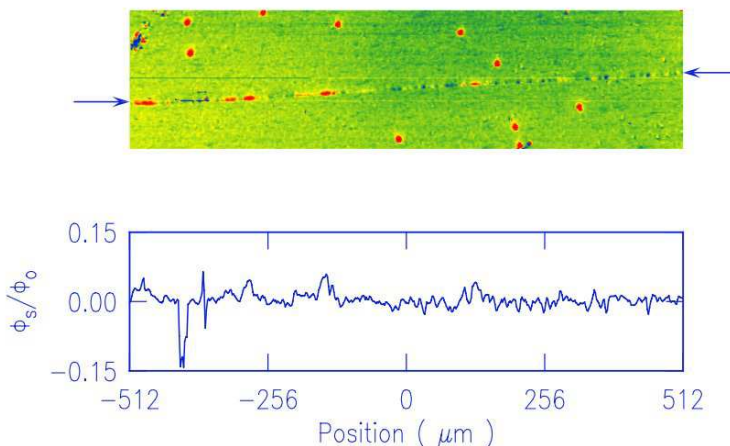


Figure 13. Scanning SQUID microscope image of an area of $1024 \times 256 \mu\text{m}^2$ along an asymmetric 45° $[001]$ tilt $\text{YBa}_2\text{Cu}_3\text{O}_{7-\delta}$ bicrystal grain boundary (arrows). There are some ten bulk vortices in the grains (film thickness ~ 180 nm), but there is also flux of both signs spontaneously generated in the grain boundary. The bottom section shows a cross section through the data along the grain boundary measured in units of Φ_0 penetrating the SQUID pickup loop. Reprinted figure with permission from J. Mannhart, H. Hilgenkamp, B. Mayer, Ch. Gerger, J.R. Kirtley, K.A. Moler, and M. Sigrist, *Phys. Rev. Lett.* **77**, 2782 (1996). Copyright 1996 by the American Physical Society.

not cross any grain boundaries has no intrinsic phase drop, and also has local minimum energies for $\Phi = n\Phi_0$. These expectations were confirmed using a SQUID microscope using a number of techniques [61], consistent with YBCO having $d_{x^2-y^2}$ pairing symmetry. Subsequent tricrystal experiments eliminated the possibility of a non-symmetry related origin for the half-integer flux quantization in the 3-junction ring [167], ruled out extended s -wave symmetry [168], demonstrated the existence of half-flux quantum Josephson vortices [169], showed results consistent with $d_{x^2-y^2}$ pairing symmetry for the hole-doped high- T_c cuprate superconductors $\text{Tl}_2\text{Ba}_2\text{CuO}_{6+\delta}$ [170], $\text{Bi}_2\text{Sr}_2\text{CaCu}_2\text{O}_{8+\delta}$ [171], and $\text{La}_{2-x}\text{Sr}_x\text{CuO}_{4-y}$ [172], for a range of doping concentrations [172], and the electron-doped cuprates $\text{Nd}_{1.85}\text{Ce}_{0.15}\text{CuO}_{4-y}$ (NCCO) and $\text{Pr}_{1.85}\text{Ce}_{0.15}\text{CuO}_{4-y}$ (PCCO) [173], and for a large range in temperatures [174]. SQUID magnetometry experiments on two-junction YBCO-Pb thin film SQUIDs were performed by Mathai *et al.* [175], and on tricrystals by Sugimoto *et al.* [176]. Josephson interference, SQUID magnetometry, and microwave measurements were made on biepitaxial all high- T_c YBCO junctions by Cedergren *et al.* [177].

Grain boundary junctions in the high- T_c cuprate superconductors are Josephson weak links. As such they are used for fundamental and device applications. In addition, grain boundaries play an important role in limiting the critical current density in superconducting cables made from the cuprates [178]. Anomalies in the dependence on magnetic field of the critical current of cuprate grain boundary junctions with misorientation angles near 45° can be understood in terms of their $d_{x^2-y^2}$ pairing symmetry combined with faceting, which naturally occurs on a 10-100nm scale in these grain boundaries [179]. This combination produces a series of intrinsic π -phase shifts along such grain boundaries. These π -shifts have spontaneous supercurrents and magnetic fields associated with them [180]. An example of SQUID microscope imaging of these spontaneous fields is shown in Figure 13. If the distance between intrinsic π -

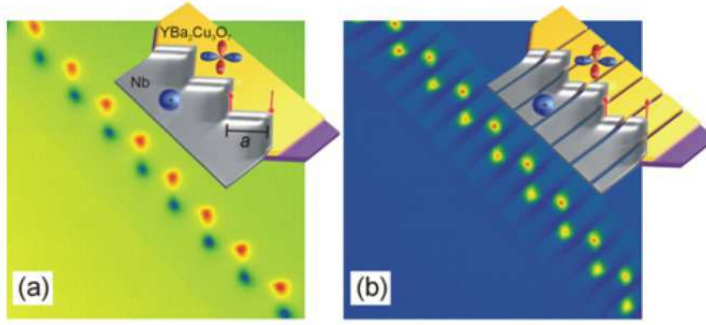


Figure 14. Generation of half-flux quanta in connected and unconnected $\text{YBa}_2\text{Cu}_3\text{O}_{7-\delta}$ -Au-Nb zigzag structures. Shown are scanning SQUID micrographs of (a) 16 antiferromagnetically ordered half-integer flux quanta at the corners of a connected zigzag structure, and (b) 16 ferromagnetically ordered half-flux quanta at the corners of an unconnected zigzag structure ($T=4.2\text{K}$). The corner to corner distance is $40\ \mu\text{m}$ in both (a) and (b). Reprinted figure with permission from Macmillan Publishers Ltd: H. Hilgenkamp, Ariando, H.J.H. Smilde, D.H.A. Blank, G. Rijnders, H. Rogalla, J.R. Kirtley, and C.C. Tsuei, *Nature* **422**, 50 (2003). Copyright 2003.

shifts is shorter than the Josephson penetration depth, the total magnetic flux associated with each will be less than $\Phi_0/2$ [181]; a high density of facets can result in “splintered” Josephson vortices with fractions of Φ_0 of flux [182].

Facetted (zigzag) junctions can also be fabricated by design, using for example a ramp-edge YBCO/Nb junction technology [183]. An example is shown in Figure 14, which shows scanning SQUID microscope images of two facetted junctions [184]. In Fig. 14a the corner junctions are connected by superconducting material. In this case there is a strong interaction between the half-flux quantum Josephson vortices upon cooling, so that they have a strong tendency to align with alternating signs of the circulating supercurrents and spontaneous magnetizations. In Fig. 14b the corner junctions have been isolated from each other by etching channels between them. In this case the half-flux quantum Josephson vortices all have the same alignment, even when cooled in a relatively small field.

Lombardi *et al.* [185], and Smilde *et al.* [186] have mapped out the in-plane momentum dependence of the superconducting gap amplitude of YBCO by measuring the critical current as a function of junction normal angle for a series of biepitaxial YBCO grain boundary junctions, and YBCO/Nb ramp junctions respectively. The latter experiments, performed in part on untwinned epitaxial YBCO films, were able to determine the anisotropy of the gap between the a and b in-plane crystalline directions. However, these experiments were only sensitive to the amplitude of the superconducting order parameter, not its phase. Phase sensitive measurements of the momentum dependence of the in-plane gap in YBCO were performed by Kirtley *et al.* [187] by imaging the spontaneously generated magnetic flux in a series of YBCO-Nb two-junction rings, with one junction angle normal relative to the YBCO crystalline axes held fixed from ring to ring, while the other junction normal angle varied. Some results from this study are shown in Figure 15. The rings either had $n\Phi_0$ (integer flux quantization) or $(n+1/2)\Phi_0$ (half-integer flux quantization) of flux in them, n an integer. The transition between integer and half-integer flux quantization happened at junction angles slightly different from $45^\circ + n \times 90^\circ$, as would be expected for a pure $d_{x^2-y^2}$ superconductor, because of the difference in gap amplitudes between the crystalline a and b phases. In

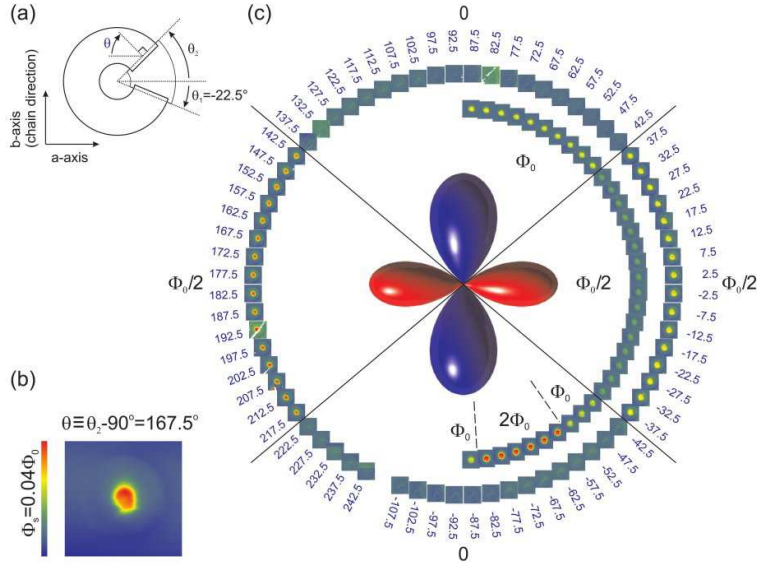


Figure 15. (a) Schematic of YBCO-Nb two-junction rings fabricated to phase sensitively determine the momentum dependence of the in-plane gap in YBCO. (b) SQUID microscope image, taken with a square pickup loop $8 \mu\text{m}$ on a side, of a square area $150 \mu\text{m}$ on a side centered on one of the rings, cooled and imaged in zero field at 4.2K . (c) The outer circle of images, taken after cooling in zero field, has a full-scale variation of $0.04 \Phi_0$ flux through the SQUID: the inner ring, taken after the sample was cooled in a field of $0.2 \mu\text{T}$, has a full scale variation of $0.09 \Phi_0$. The rings cooled in zero field had either 0 or $\Phi_0/2$ of flux in them; the rings cooled in $0.2 \mu\text{T}$ had $\Phi_0/2$, Φ_0 or $2\Phi_0$ of flux, as labelled. Reprinted figure with permission from Macmillan Publishing Ltd: J.R. Kirtley, C.C. Tsuei, Ariando, C.J.M. Verwijs, S. Harkema and H. Hilgenkamp, *Nature Physics* **2**, 190 (2006). Copyright 2006.

addition, careful integration of the total flux in the rings showed that any imaginary component to the order parameter, if present, must be small.

3.1.4. Ring arrays Arrays of superconducting rings are of interest as a physical analogue of a spin: for conventional superconducting rings the states with shielding supercurrent flowing clockwise or counter-clockwise are degenerate at a magnetic flux bias of $\Phi_0/2$ (half of a flux quantum threading each ring). Two neighboring rings can interact magnetically, making them a physical analogue of the Ising spin. Frustration can be introduced into the system by choosing the arrangement of the rings: square and hexagonal lattices are geometrically unfrustrated, while triangular and Kagome lattices are frustrated.

Davidovic *et al.* used scanning Hall bar microscopy to study two-dimensional arrays of closely spaced Nb rings (see Fig. 16) [144, 145]. In these experiments Davidovic *et al.* found that it was possible to find small islands of antiferromagnetically ordered “spins”, but no perfect ordering, even in arrays with no geometrical frustration. One source of disorder in arrays of conventional superconducting rings is variation in area from ring to ring from lithographic variations. Conventional rings must be flux biased to near $\Phi_0/2$ flux with high precision (see Fig. 16), and area variations lead to flux variations.

The same technology used for the pairing symmetry tests of Fig. 15 were used to form two-dimensional arrays of π -rings, superconducting rings with an intrinsic phase shift of π [184]. An example of SQUID microscope imaging of several π -ring arrays is

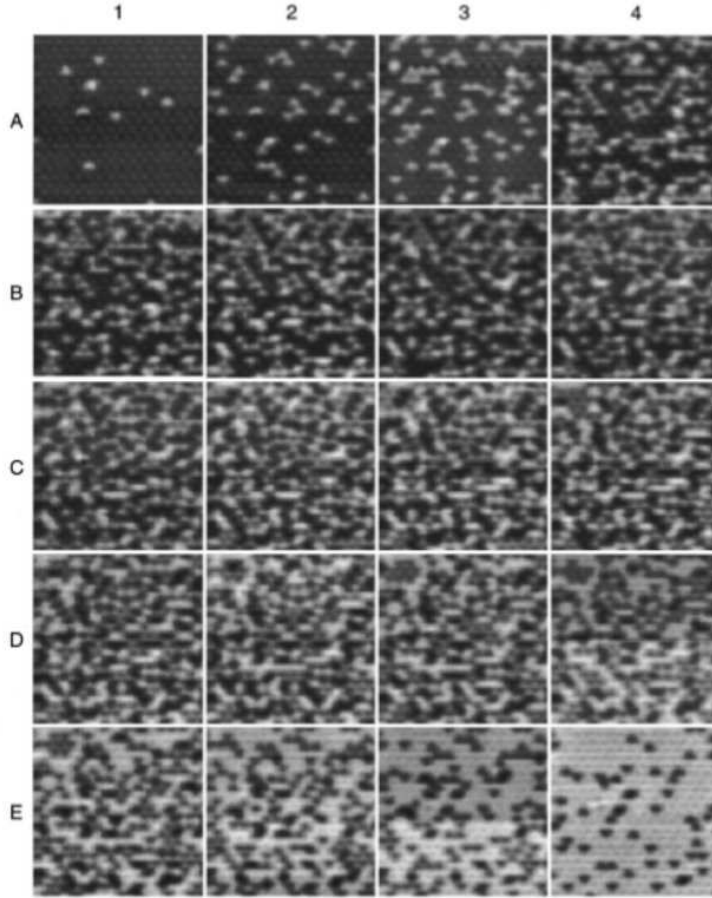


Figure 16. A sequence of field-cooled images of a honeycomb lattice of $1\mu\text{m}$ diameter hexagonal Nb thin film rings, taken in increasing applied fluxes near an applied flux per ring of $\Phi_0/2$. The flux increases from left to right starting at the upper left corner with $0.4913\Phi_0$ and ending in the lower right corner at $0.5066\Phi_0$. Reprinted figure with permission from D. Davidović, S. Kumar, D.H. Reich, J. Siegel, S.B. Field, R.C. Tiberio, R. Hey, and K. Ploog, *Phys. Rev. B* **55**, 6518 (1997). Copyright 1997 by the American Physical Society.

shown in Figure 17 [188]. π -rings have two degenerate states at zero flux bias, therefore eliminating the need for precise flux biasing of the rings, and thereby eliminating slight differences in the sizes of the rings as a source of disorder [188]. Although π -ring arrays showed more negative values of the bond-order σ , corresponding to greater antiferromagnetic ordering, perfect ordering was never observed in either conventional or π -ring arrays, possibly because of the large number of nearly degenerate states in this system [189].

3.1.5. Tests of the interlayer tunneling model One candidate mechanism for superconductivity at high temperatures in the cuprate perovskite superconductors is the interlayer tunneling model, in which the superconductivity results from an increased coupling between the layers in the superconducting state [190, 191, 192, 193, 194]. An essential test of this theory is the strength of the interlayer Josephson tunneling in layered superconductors. For the interlayer tunneling model to succeed, the interlayer

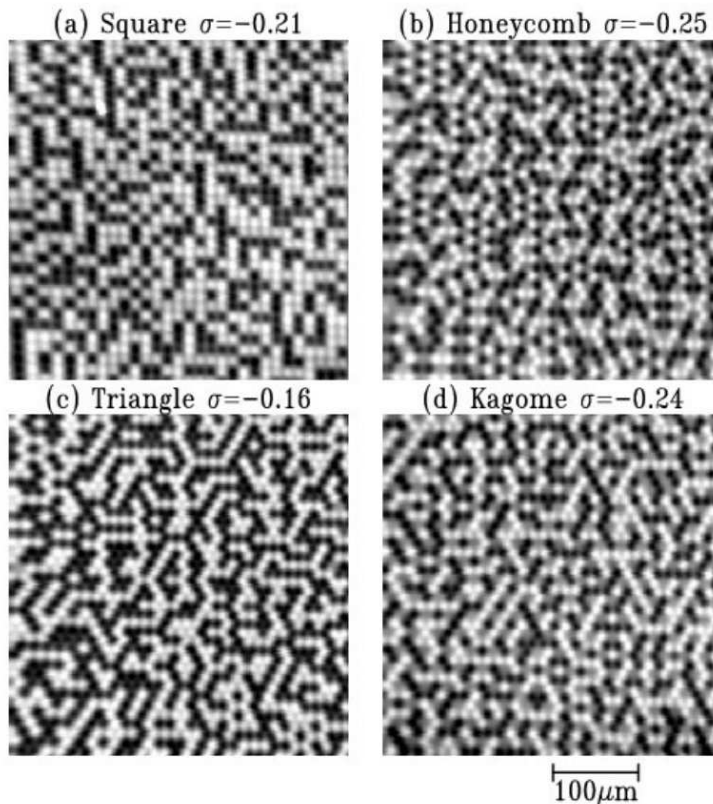


Figure 17. SQUID microscopy images of four electrically disconnected arrays of π -rings with $11.5 \mu\text{m}$ nearest neighbor distances. These images were taken at 4.2 K with a $4 \mu\text{m}$ diameter pickup loop after cooling in nominally zero field at 1-10 mK/s. The bond-order σ is a measure of the anti-ferromagnetic order in the arrays. The geometrically unfrustrated square and honeycomb arrays could have perfect antiferromagnetic correlation, which would correspond to $\sigma = -1$. The minimum possible bond-order for the frustrated Kagome and triangle lattices is $\sigma = -1/3$. Reprinted figure with permission from J.R. Kirtley, C.C. Tsuei, Ariando, H.J.H. Smilde, and H. Hilgenkamp, Phys. Rev. B **72**, 214521 (2005). Copyright 2005 by the American Physical Society.

coupling in the superconducting state must be sufficiently strong to account for the large condensation energy of the cuprate superconductors. The best materials for testing this requirement are $\text{Tl}_2\text{Ba}_2\text{CuO}_{6+\delta}$ (Tl-2201) and $\text{HgBa}_2\text{CuO}_{4+\delta}$ (Hg-1201), which have high critical temperatures ($T_c \approx 90$ K) and a single copper oxide plane per unit cell. Scanning SQUID microscope images were made of interlayer Josephson vortices emerging from the $a-c$ face of Tl-2201 [195] (Fig. 18) and Hg-1201 [196]. The extent of these vortices in the a -axis direction is set by the interlayer penetration depth λ_c . Some spreading of the vortex fields occurs as the crystal surface is approached [197], but not enough to affect the qualitative conclusions from these studies: the experimentally determined interlayer penetration depth λ_c is an order of magnitude larger than required by the interlayer tunneling model. These conclusions are in agreement with measurements of the Josephson plasma frequency in these materials [198].

3.1.6. Pearl vortices Vortices in thin superconductors satisfying $d \ll \lambda_L$, where d is the thickness and λ_L is the London penetration depth, first described by Pearl [199],

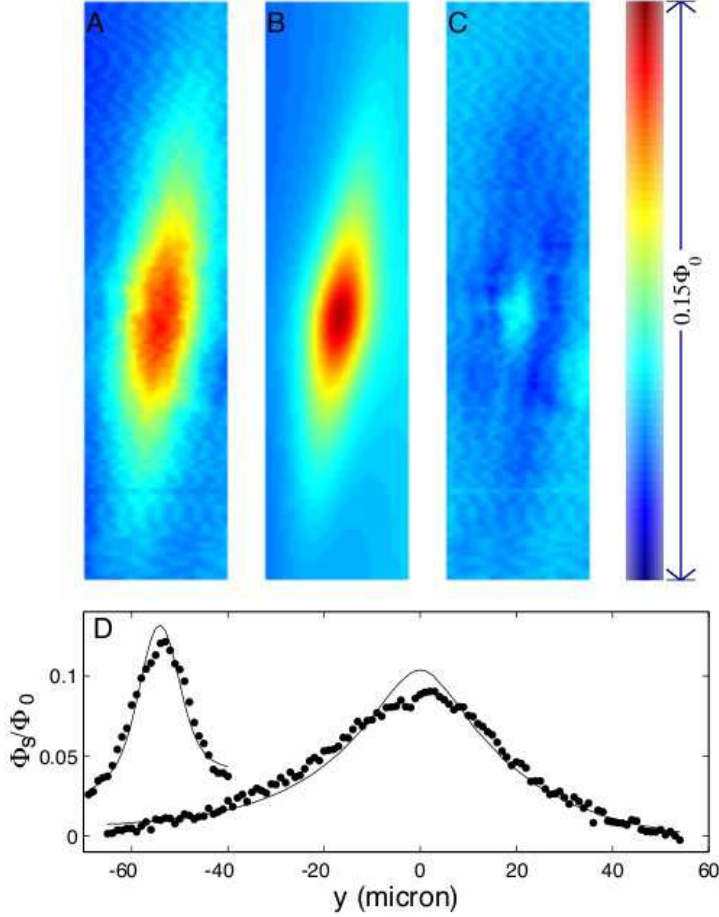


Figure 18. **A** Scanning SQUID microscope image of an interlayer Josephson vortex emerging from the *ac* face of a single crystal of the single-layer cuprate superconductor $\text{Tl}_2\text{Ba}_2\text{CuO}_{6+\delta}$, imaged at 4.2K with a square pickup loop $8.2 \mu\text{m}$ on a side. **B** A 2-dimensional fit to the vortex in **A** with λ_c , the penetration depth perpendicular to the CuO_2 planes, equal to $18\mu\text{m}$ and z_0 , the spacing between the SQUID pickup loop and the sample surface, equal to $3.6 \mu\text{m}$. **C** The difference between the data and the fit. **D** Cross sections perpendicular and parallel to the long axis of the vortex, offset for clarity. From K.A. Moler, J.R. Kirtley, D.G. Hinks, T.W. Li, and Ming Xu, *Science* **279**, 1193 (1998). Reprinted with permission from AAAS.

have several interesting attributes. The field strengths H_z perpendicular to the films diverge as $1/r$ at distances $r \ll \Lambda$, where $\Lambda = 2\lambda_L^2/d$ is the Pearl length, in Pearl vortices, whereas in Abrikosov (bulk) vortices the fields diverge as $\ln(r/\lambda_L)$ [200]. Since in the Pearl vortex much of the vortex energy is associated with the fields outside of the superconductor, the interaction potential $V_{int}(r)$ between Pearl vortices has a long range component $V_{int} \sim \Lambda/r$ for $r \gg \Lambda$ [199], unlike Abrikosov vortices, which have only short range interactions. Although it was originally believed that the interaction between Pearl vortices $V_{int} \sim \ln(\Lambda/r)$ for $r \ll \Lambda$ leads to a Berezinskii-Kosterlitz-Thouless (BKT) transition which is cut off due to screening on a scale Λ [111], Kogan [201] reports that the BKT transition could not happen in thin superconducting films of any size on insulating substrates because of boundary conditions at the film edges that turn the interaction into a near exponential decay. Grigorenko *et al.*, using SHM,

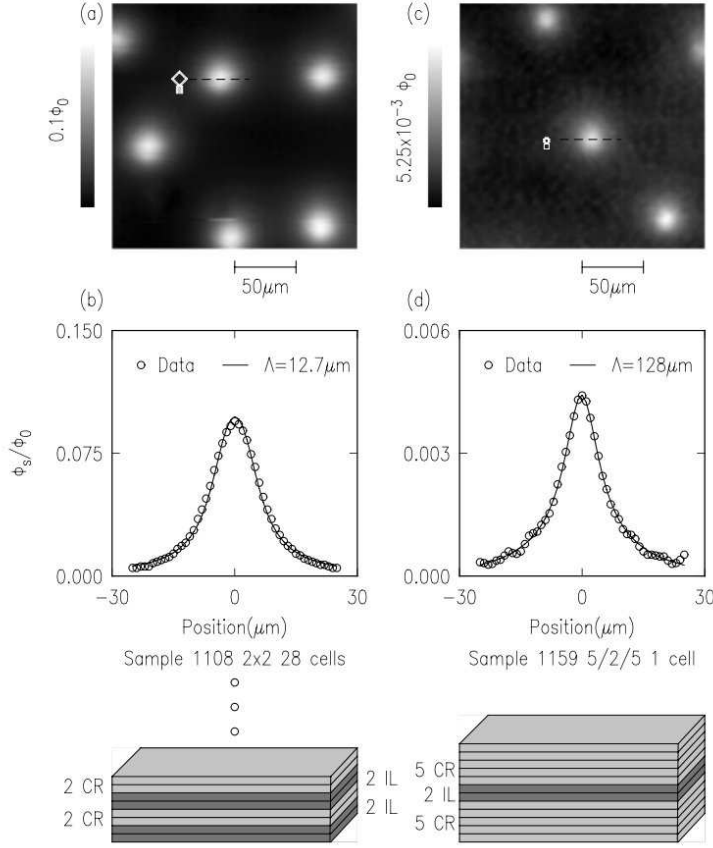


Figure 19. SQUID microscope image and cross-sectional data along the positions indicated by the dashed line in (a), (c) of Pearl vortices trapped in two artificially layered $(\text{Ba}_{0.9}\text{Nd}_{0.1}\text{CuO}_{2+x})_m/(\text{CaCuO}_2)_n$ superconducting films. The SQUID pickup loops were a square $7.5 \mu\text{m}$ on a side (a),(b), and an octagon $4 \mu\text{m}$ on a side (c),(d) (schematics superimposed on image). The open symbols in (b),(d) are the cross-sectional data; the solid lines in (b), (d) are fits. Reprinted figure with permission from F. Tafuri, J.R. Kirtley, P.G. Medaglia, P. Orgiani, and G. Balestrino, *Phys. Rev. Lett.* **92**, 157006 (2004). Copyright 2004 by the American Physical Society.

observed domains of commensurate vortex patterns near rational fractional matching fields of a periodic pinning array in a thin film superconductor, which could only form when the vortex-vortex interactions are long range [202].

Figure 19 shows scanning SQUID microscope images of Pearl vortices in ultra-thin $[\text{Ba}_{0.9}\text{Nd}_{0.1}\text{CuO}_{2+x}]_m/[\text{CaCuO}_2]_n$ (CBCO) high-temperature superconductor films. Pearl vortices can be magnetically imaged in such thin films, although the Pearl length can be as large as 1 mm, because of the strong $1/r$ divergence of the Pearl vortex magnetic fields at the vortex core: The thin-film limit for the two-dimensional Fourier transform of the z -component of the field from an isolated vortex trapped in a thin film is given by [199, 203]:

$$B_z(k, z) = \frac{\Phi_0 e^{-kz}}{1 + k\Lambda}, \quad (25)$$

where z is the height above the film, $k = \sqrt{k_x^2 + k_y^2}$, $\Lambda = 2\lambda_{ab}^2/d$, λ_{ab} is the in-plane

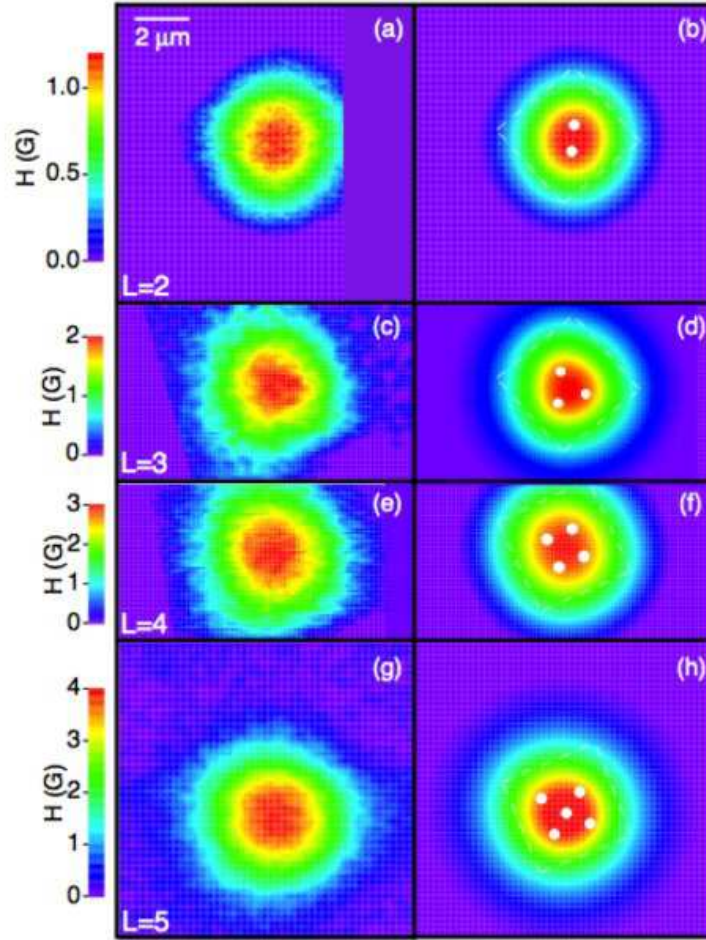


Figure 20. Scanning Hall probe microscope images of a $4\ \mu\text{m} \times 4\ \mu\text{m}$ square Pb film at applied fields of (a) 4.6 G, (c) 6.6 G, (e) 8.6 G, and (g) 10.6 G. [(b), (d), (f), and (h)] The results of 2D monopole fits to (a), (c), (e), and (g) respectively. The broken lines denote the shape of the square. The locations of the vortices are shown as white points. Reprinted figure with permission from T. Nishio, Q. Chen, W. Gillijns, K. De Keyser, K. Vervaeke, and V.V. Moshchalkov, Phys. Rev. B **77**, 012502 (2008). Copyright 2008 by the American Physical Society.

penetration depth, d is the film thickness and $\Phi_0 = h/2e$.

The open circles in Fig. 19(b,d) are cross-sections through the data of Fig. 19(a,c). The solid lines are fits to the data using Eq. 25, using the Pearl length Λ as a fitting parameter. The in-plane London penetration depth λ_{ab} of these thin films can be inferred from Λ if d is known.

3.1.7. Mesoscopic superconductors Vortices in superconductors with dimensions comparable to the superconducting coherence length ξ have been predicted to nucleate spontaneously in a number of interesting configurations, such as shells [204], giant vortices [205], and anti-vortices, so as to preserve the symmetry of the sample [206, 207]. Vortex trapping patterns in mesoscopic superconducting samples have been studied using Bitter decoration [208], scanning SQUID microscopy [209], ballistic Hall magnetometry [91], transport [210], and Hall bar microscopy. An example of Hall bar microscopy results is shown in Figure 20. Nishio *et al.* [211] report results in

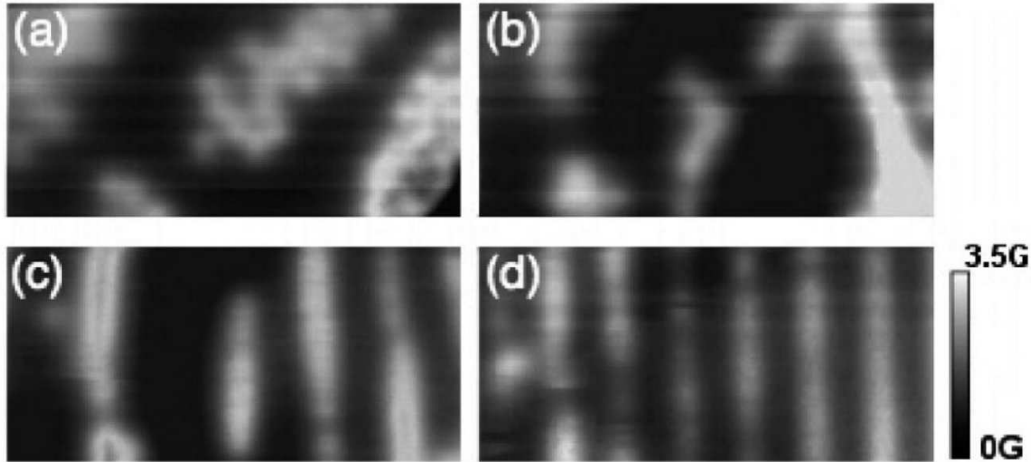


Figure 21. Scanning SQUID microscope images of flux domains in Sr_2RuO_4 at $T=0.36$ K after field cooling at various fields. In all cases, the magnetic field amplitude applied along the c axis (H_{\perp}) was kept constant at 2 G while the in-plane field (H_{ab}) was (a) 0 G, (b) 5 G, (c) 10 G, (d) 50 G. The imaging area is $31 \mu\text{m} \times 17 \mu\text{m}$. The field scale in G is shown on the right; dark regions are superconducting vortex-free regions. Reprinted figure with permission from V.O. Dolocan, C. Veauvy, F. Servant, P. Lejay, K. Hasselbach, Y. Liu, and D. Mailly, *Phys. Rev. Lett.* **95**, 097004 (2005). Copyright 2005 by the American Physical Society.

agreement with Ginzburg-Landau calculations for temperatures considerably lower than the superconducting transition temperature.

3.1.8. Sr_2RuO_4 Sr_2RuO_4 , with the same crystal structure as La_2CuO_4 , the parent compound for the first class of cuprate perovskite compounds shown to exhibit high-temperature superconductivity [2], was discovered in 1994 to be superconducting at about 1K [6]. It is thought to be a $p_x \pm ip_y$ -wave, triplet pairing superconductor with broken time-reversal symmetry. One of the consequences of this pairing symmetry state is spontaneously generated supercurrents, and consequent large magnetic fields at surfaces and boundaries between $p_x + ip_y$ and $p_x - ip_y$ domains [212]. Although there is evidence for characteristic magnetic fields of 0.5G in Sr_2RuO_4 from muon spin resonance experiments [213], and evidence for broken time-reversal symmetry at the surface of Sr_2RuO_4 has been obtained using Sagnac interferometry [18], no evidence for spontaneously generated magnetic fields at the surfaces of Sr_2RuO_4 samples has been found in scanning Hall bar and scanning SQUID experiments, with much higher sensitivity than the magnetic fields originally predicted [214, 215, 216]. A possible explanation for this failure to observe spontaneous magnetization directly is that the $p_x \pm ip_y$ domains are small, so that the fields from closely spaced domain boundaries nearly cancel each other. The experimental information on $p_x \pm ip_y$ domain sizes is not consistent, with the first phase sensitive pairing symmetry experiments on Sr_2RuO_4 being consistent with domain sizes of order 1 mm [217], while later phase-sensitive results are consistent with domain sizes $1\mu\text{m}$ or less [218], and the Sagnac interferometry being consistent with domain sizes intermediate between these two sizes [18]. Recently Raghu *et al.* have suggested that the superconductivity in Sr_2RuO_4 arises primarily in quasi-one-dimensional bands, and is therefore not expected to generate experimentally

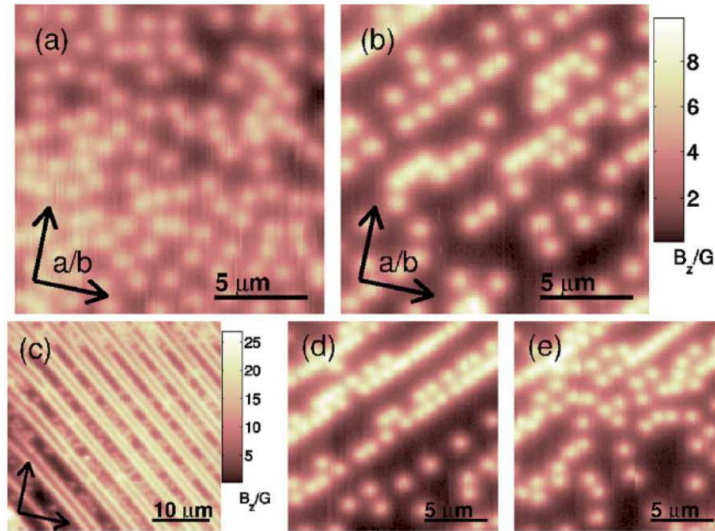


Figure 22. Scanning Hall bar image of a single crystal sample of $\text{ErNi}_2\text{B}_2\text{C}$. After cooling below T_c in a weak field [2.4 Oe in (a), (b), (d), (e), 18 Oe in (c)], a vortex distribution consistent with random pinning is observed on the ab face [(a) 7.3 K]. Upon reducing the temperature below T_N , the vortices spontaneously organize along twin domain walls along the $[110]$ [(b) 5.3 K] or $[1\bar{1}0]$ [(c) 4.2 K] direction. The pattern gradually disappears as the temperature is raised again [(d) 5.7 K, (e) 6.0 K, different cycle than (a) and (b)]. Reprinted figure with permission from H. Bluhm, S.E. Sebastian, J.W. Guikema, I.R. Fisher, and K.A. Moler, *Phys. Rev. B* **73**, 014514 (2006). Copyright 2006 by the American Physical Society.

detectable edge currents [219].

Dolocan *et al.* [220, 221] have magnetically imaged single crystals of Sr_2RuO_4 using a scanning μSQUID mounted on a tuning fork in a dilution refrigerator. This allowed combined magnetic and topographic information on a length scale of 1 micron, at temperatures below 400 mK. They found coalescence of vortices and the formation of flux domains (see Fig. 21). The formation of lines of vortices in a field tilted relative to the crystalline c -axis [222] can be attributed in this case to the large anisotropy in Sr_2RuO_4 , resulting in an attractive interaction between vortices in a plane defined by the c -axis and the magnetic field direction [221]. The vortex coalescence observed when the applied magnetic field is parallel to the c axis may be due to weak intrinsic pinning at domain walls, and the existence of a mechanism for bringing vortices together that overcomes the conventional repulsive vortex-vortex interaction.

3.1.9. Magnetic superconductors Magnetic order and superconductivity are competing orders since the Meissner state excludes a magnetic field from the bulk and superconductivity is destroyed at sufficiently high fields. However, superconductivity and magnetism can coexist [223, 224, 225, 226] if the orientation of the local magnetic moments varies on a length scale shorter than the superconducting penetration depth λ , or if the field generated by the magnetization is carried by a so-called spontaneous vortex lattice [227]. The former order has been observed in ErRh_4B_4 and HoMo_6S_8 [228, 229], and indirect evidence for the latter has been reported in UCoGe [230]. Several Hall bar studies have been performed on artificial ferromagnetic-superconducting hybrid

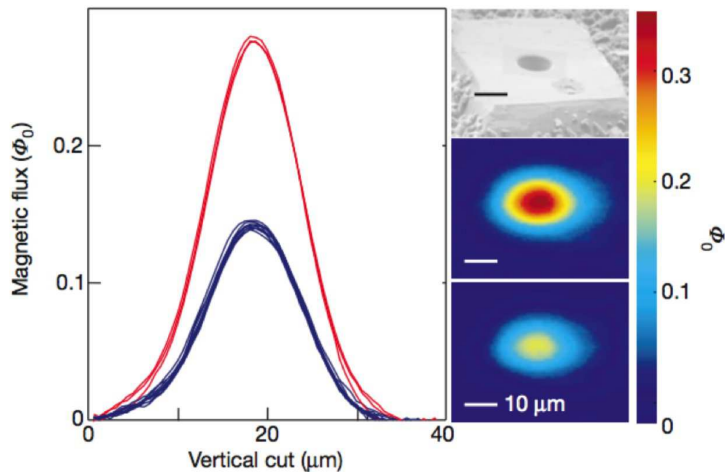


Figure 23. Cross-sections and images of single (bottom right image, blue cross-section) and double (middle right image, red cross section) flux quanta trapped in a $50\mu\text{m} \times 50\mu\text{m}$ square of single-crystal $\text{YBa}_2\text{Cu}_3\text{O}_{6.35}$ ($T_c=6.0\text{K}$) with a $10\mu\text{m}$ hole drilled using a focussed ion beam (top right image). When the sample was heated to 5.6K for 1 sec and re-cooled to 2K , these flux quanta escaped with no sign of the vortex memory associated with visons. Reprinted figure with permission from Macmillan Publishing Ltd: D.A. Bonn, J.C. Wynn, B.W. Gardner, Y.-J. Lin, R. Liang, W.N. Hardy, J.R. Kirtley and K.A. Moler, *Nature* **414**, 887 (2001). Copyright 2001.

structures [231, 232, 233, 234]. Fig. 22 [235] shows scanning Hall bar microscopy measurements of $\text{ErNi}_2\text{B}_2\text{C}$, which has a superconducting T_c of $\approx 11\text{K}$, becomes antiferromagnetic below $T_N \approx 6\text{K}$, and exhibits weak ferromagnetism below $T_{WFM} \approx 2.3\text{K}$ [236]. Bluhm *et al.* [235] found that in this material the superconducting vortices spontaneously rearranged to pin on twin boundaries upon cooling through the antiferromagnetic transition temperature, and that a weak random magnetic signal appears in the ferromagnetic phase.

3.2. Fluxoid dynamics

3.2.1. Limits on spin-charge separation One explanation for the peculiar normal state properties and high superconducting transition temperatures of the high- T_c cuprate perovskites is that there exists a new state of matter in which the elementary excitations are not electron-like, as in conventional metals, but rather the carriers “fractionalize” into “spinons”, chargeless spin $1/2$ fermions, and “chargons”, bosons with charge $+e$ [237]. Senthil and Fisher proposed a model for such a separation in two dimensions with sharp experimental tests [238]: in conventional superconductors a Cooper pair with charge $2e$ circling around a vortex with $h/2e$ of total magnetic flux experiences a phase shift of 2π . However, a chargon would pick up only a phase shift of π . In order for the chargon wave function to remain single-valued, it must be accompanied by a “vison” that provides an additional π phase shift. In the Senthil-Fisher test, a superconducting ring with flux trapped in it is warmed through the superconducting transition. If the number of vortices in the ring is odd, then it will also contain a vison that could persist above T_c . If the ring is then re-cooled in zero field before the vison escapes, it will spontaneously generate a single flux quantum with random sign. On the other hand, if the number of vortices in the ring is even, no such “vortex memory”

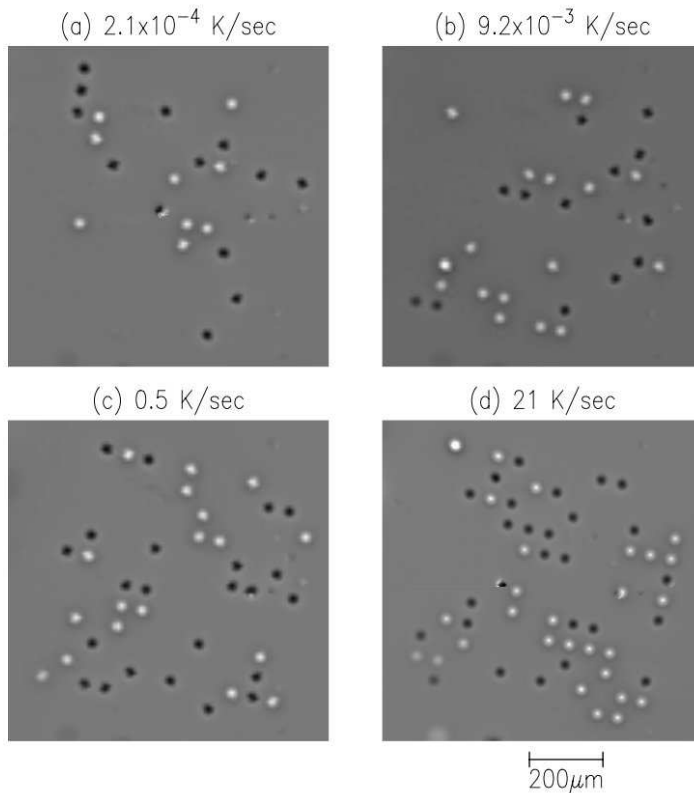


Figure 24. SQUID microscope images of a 12×12 array of $20 \mu\text{m}$ inside diameter, $30 \mu\text{m}$ outside diameter thin film rings of Mo_3Si , cooled in zero field through the superconducting T_c at various rates. The resulting ring vortex numbers were consistent with thermally activated spontaneous fluxoid formation. Reprinted figure with permission from J.R. Kirtley, C.C. Tsuei, and F. Tafuri, Phys. Rev. Lett. **90**, 257001 (2003). Copyright 2003 by the American Physical Society.

effect would exist. Bonn *et al.* [239] (Fig. 23) tested for this effect in highly underdoped single crystals of $\text{YBa}_2\text{Cu}_3\text{O}_{6+x}$. These crystals have a very sharp but low transition temperature favorable for such a test. They found no evidence for a vortex memory effect, and were able to put stringent upper limits on the energy associated with a vortex. Some models in which superconductivity results from spin-charge separation predicts h/e fluxoids in materials with low superfluid density [240, 241, 242]. Wynn *et al.* [243], using scanning SQUID and Hall bar microscopies, found no evidence for h/e vortices in strongly underdoped $\text{YBa}_2\text{Cu}_3\text{O}_{6+x}$ crystals, also placing limits on spin-charge separation in these materials.

3.2.2. Superconducting rings As we have seen in previous sections, the dynamics of fluxoids in a ring configuration are of interest as a model for the Ising spin system [144, 145, 188] 3.1.4, and for placing limits on spin-charge separation in underdoped cuprate superconductors [239] 3.2.1. Kirtley *et al.* studied fluxoid dynamics in photolithographically patterned thin film rings of the underdoped high-temperature superconductor $\text{Bi}_2\text{Sr}_2\text{CaCu}_2\text{O}_{8+\delta}$ using a scanning SQUID microscope, and concluded that their results could be understood in terms of thermally activated nucleation of a Pearl vortex in, and transport of the Pearl vortex across, the ring wall [244].

Fluxoid dynamics in superconducting rings may also provide clues to physics on an entirely different scale: the early development of the universe. Immediately after the Big Bang a fundamental symmetry related the particles that mediated the electromagnetic, strong, and weak forces. However, as the universe cooled down this symmetry was broken in such a way that, for example, the W and Z bosons, which mediate the weak interaction, have mass, while photons, which mediate the electromagnetic force, do not. Kibble proposed an intuitive picture of this symmetry breaking of the early universe [245, 246], with the underlying idea that causality governed the number of defects because a finite time delay is needed for information to be transferred between different regions of a system. Zurek pointed out that Kibble’s ideas could be tested by studying vortices in superfluids and superconductors [247]. As a superconductor or superfluid cools through its transition temperature different regions can nucleate into a state with the same order parameter amplitude ψ but different phases ϕ . This will produce “kinks” or “defects” where ϕ would eventually (at low temperature) change by 2π . These kinks can be removed by annihilation with anti-kinks if the coherence length ξ is long enough and the cooling rate is sufficiently slow. However, as the system cools this annihilation process proceeds less rapidly, until at some point the kinks “freeze-in” because part of the system cannot communicate with other parts quickly enough. In a superconducting ring a phase shift of 2π around the ring corresponds to a fluxoid trapped in the ring, so that the process of forming and freezing in kinks is also called spontaneous fluxoid generation. Kibble and Zurek showed that causality implies that the probability P of finding a spontaneous fluxoid in the ring (when cooled in zero external field) depends on the cooling rate τ_Q^{-1} as $P \propto (\tau_Q/\tau_0)^{-\sigma}$, where τ_0 is a characteristic time and σ depends on how the correlation length ξ and the relaxation time τ vary with temperature close to the transition. For a superconducting ring and assuming a mean-field approximation $\sigma = 1/4$.

Tests of the Kibble-Zurek prediction have been made by looking for vortices in superfluid ^4He [248, 249] and ^3He [250, 251], in superconducting films [252, 15], and superconducting rings interrupted by Josephson junctions [253, 254, 255]. However, verification of the ideas of Kibble and Zurek using arguably the simplest system, superconducting rings, were not made until recently. Kirtley, Tsuei and Tafuri [256] (Fig. 24) used a SQUID microscope to image an array of rings after repeated cooling in various magnetic fields and cooling rates to determine the probability of spontaneous fluxoid generation. They showed that a second mechanism prevailed, in which the final density of fluxoids depended on a balance between thermal generation and the relaxation rates of fluxoids [257, 258, 259]. They argued that the thermal fluctuation mechanism is complementary to the “causal” mechanism and should be considered in attempts to understand phase transitions, both in the laboratory and in the early universe. The Kirtley *et al.* experiments [256] were done on rings with parameters which favored the thermal activation mechanism over the Kibble-Zurek (causal) mechanism. Recently Monaco *et al.* [260] have studied superconducting rings with parameters more favorable to the causal mechanism, using a geometry in which the flux state of a single ring can be manipulated and sensed rapidly, and find results consistent with the Kibble-Zurek prediction, taking into account the fact that the ring’s circumference was much smaller than the coherence length at the temperature at which the fluctuations were frozen in.

3.2.3. High- T_c grain boundaries Grain boundaries in the cuprate high- T_c superconductors are widely used for devices and fundamental studies, and govern the transport properties of superconductors with technological applications [178]. It is therefore important to understand the mechanism of dissipation in transport across grain bound-

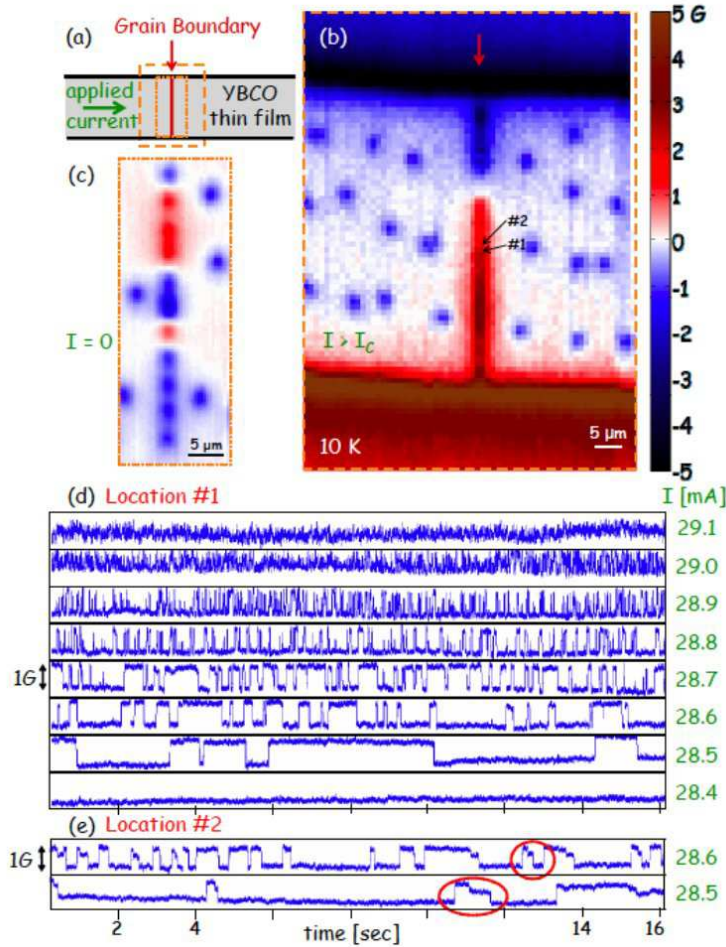


Figure 25. Scanning Hall bar measurements of vortex noise in a 24° symmetric YBCO grain boundary (GB). (a) Sketch of the sample. The bridge width is $50 \mu\text{m}$. (b,c) Magnetic image of the GB area (b) at 10 K and applied current $I = 29$ mA and (c) at 10 K after thermal cycling to 70 K with $I = 0$, showing individual vortices (red) and antivortices (blue). The regions imaged are outlined in orange in (a). (d,e) The Hall probe signals *vs.* time at 10 K for different currents applied to the GB measured at two positions marked in Fig. 1b. The switching events are vortices passing under the probe. Red circles indicate three-level switching events. Reprinted figure with permission from B. Kalisky, J.R. Kirtley, E.A. Nowadnick, R.B. Dinner, E. Zeldov, Ariando, S. Wenderich, H. Hilgenkamp, D.M. Feldmann, and K.A. Moler, *Appl. Phys. Lett.* **94**, 202504 (2009). Copyright 2009 by the American Institute of Physics.

aries. Transport across grain boundaries is usually studied with a voltage threshold on the order of nanovolts. At these voltages millions of vortices traverse the boundary per second. Much smaller voltages can be measured by magnetically imaging the vortices in the grain boundaries. Kalisky *et al.* [261] performed such measurements on grain boundaries produced by epitaxial growth of the cuprate high- T_c superconductor $\text{YBa}_2\text{Cu}_3\text{O}_{7-\delta}$ on bicrystals of SrTiO_3 using a large scanning area Hall bar microscope [84]. They observed (Figure 25) telegraph noise in the Hall bar signal when the sensor was directly above the grain boundary, which they attributed to the motion of vortices. They inferred the voltage across the grain boundary from the frequency of the telegraph noise, with voltage sensitivity as small as $2 \times 10^{-16} \text{V}$. The dependence of the inferred

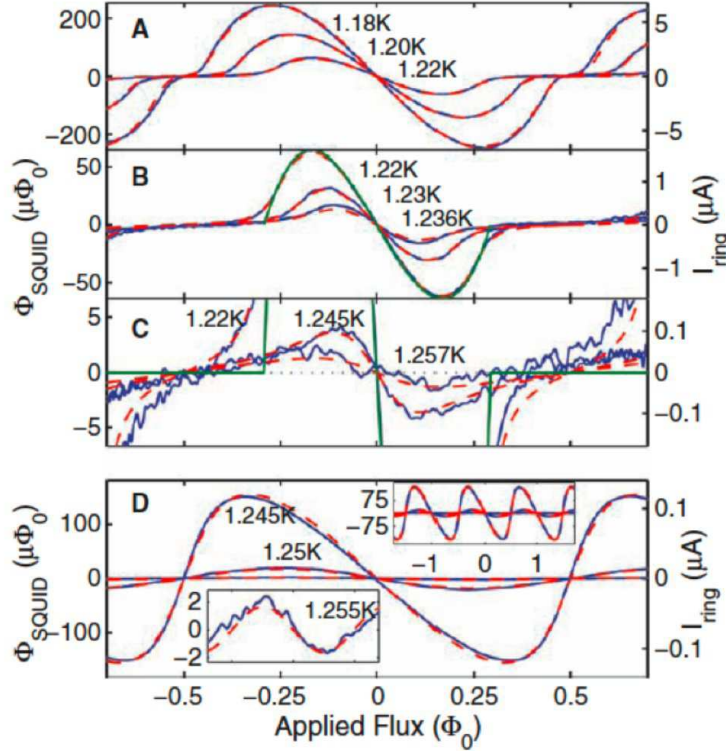


Figure 26. SQUID signal (left axis) and ring current (right axis) as a function of applied flux Φ_a for two aluminum rings, both with thickness $d = 60$ nm and annulus width $w = 110$ nm. The fluctuation theory (dashed red) was fit to the data (blue) through the dependence of I_{ring} on Φ_a and temperature. (A to C) ring radius $R = 0.35 \mu\text{m}$, fitted $T_c(\Phi_a=0) = 1.247$ K, and $\gamma = 0.075$. The parameter γ characterizes the size of the ring. The green line is the theoretical mean field response for $T = 1.22$ K and shows the characteristic Little-Parks line shape, in which the ring is not superconducting near $\Phi_a = \Phi_0/2$. The excess persistent current in this region indicates the large fluctuations in the Little-Parks regime. (D) $R = 2 \mu\text{m}$, fitted $T_c(\Phi_a=0) = 1.252$ K, and $\gamma = 13$. From N.C. Koshnick, H. Bluhm, M.E. Huber, and K.A. Moler, *Science* **318**, 1440 (2007). Reprinted with permission from AAAS.

grain boundary voltage on current followed either an exponential $V \propto e^{mI/I_c}$ or a power law $V \propto I^n$ dependence with high values of m or n . These results were qualitatively different from grain boundary transport measurements at higher voltages [178, 262, 263], and could not be fully explained using existing models.

3.3. Local susceptibility measurements

3.3.1. Superconducting fluctuations Experimental knowledge of superconducting fluctuations in one dimension has largely been derived from transport measurements [264], which require electrical contacts and an externally applied current. The SQUID susceptometer, along with a ring geometry for the superconductor, allows the study of fluctuation effects, without contacts, in isolated, quasi one-dimensional rings in the temperature range where the circumference is comparable to the temperature-dependent Ginzburg-Landau coherence length $\xi(T)$. In such measurements, an example of which is shown in Fig. 26 [265], a magnetic field is applied to the ring using a single-turn field

coil, co-planar and concentric with the pickup loop, both of which are integrated into the SQUID sensor [72]. The response of the ring to this applied flux is measured by the pickup loop. The SQUID sensor is in a carefully balanced gradiometer configuration, such that it is insensitive to the fields applied by the field coil [73]. Nevertheless, further background subtraction, by comparing the mutual inductance between the field coil and SQUID with the pickup loop close to the ring with that with the pickup loop at a distance, is required to measure the response field due to the ring, which can be 7 orders of magnitude smaller than the applied field. A scanned sensor allows multiple rings to be measured in a single cooldown. The experimental results agree with a full numeric solution of thermal fluctuations in a Ginzburg-Landau framework that includes non-Gaussian effects [266, 267] for all of the rings for which calculations were numerically tractable. This is in contrast to previous work on a single Al ring [268], which disagreed strongly with theory.

Similar techniques have allowed the measurement of spontaneous persistent currents in normal metal rings [269].

3.3.2. Stripes The pnictide class of superconductors [8] have the highest critical temperatures (57K) observed for a non-cuprate superconductor, multiband Fermi surfaces, and at certain doping levels a paramagnetic to antiferromagnetic as well as a tetragonal to orthorhombic transition above the superconducting transition temperature. In $\text{Ba}(\text{Fe}_{1-x}\text{Co}_x)_2\text{As}_2$ (Co doped Ba-122) and other members of the 122 family (AFe_2As_2 with $\text{A}=\text{Ca}, \text{Sr}, \text{and Ba}$), doping causes the spin-density-wave transition temperature and the structural transition temperature to decrease [270, 271] falling to zero at or near the doping where the highest T_c occurs, suggesting the importance of lattice changes in determining transport properties. Both experiment [272, 273, 274] and theory [275] have suggested a close relationship between structural and magnetic properties, leading some authors to describe the lattice and spin density-wave transition by a single order parameter [276, 277]. In addition, structural strain appears to play a significant role in the superconductivity. For example, in the 122 compounds, small amounts of non-hydrostatic pressure can induce superconductivity [278, 279, 280, 281, 282]. In addition, there is evidence that the structural perfection of the Fe-As tetrahedron is important for the high critical temperatures observed in the Fe pnictides [283, 284].

Kalisky *et al.* [285] have shown that Co doped Ba-122 has stripes of enhanced susceptibility below the superconducting transition temperature (see Fig. 27). These stripes are resolution limited using a SQUID pickup loop with an effective diameter of $4\mu\text{m}$, and are believed to be associated with boundaries between twins- crystallites with their in-plane a, b axes rotated by 90° . The amplitude of the susceptibility stripes becomes larger as the superconducting transition temperature is approached from below. Since the susceptibility signal for a homogeneous superconductor becomes larger as the penetration depth becomes shorter and the superfluid density becomes larger, it seems reasonable to associate the susceptibility stripes with shorter penetration depths and enhanced superfluid densities on the twin boundaries. Twin boundaries have been associated with enhanced superfluid density in conventional superconductors [286], but the influence of twin planes on superconductivity in, for example, the cuprates is less clear [287, 288, 289, 290, 291].

It is difficult to calculate analytically the effect of a plane of reduced penetration depth (enhanced superfluid density) on the susceptibility observed in scanning SQUID measurements. Kirtley *et al.* [292] have done a finite-element calculation in the appropriate geometry. Because of the uncertainty in the width of the region with

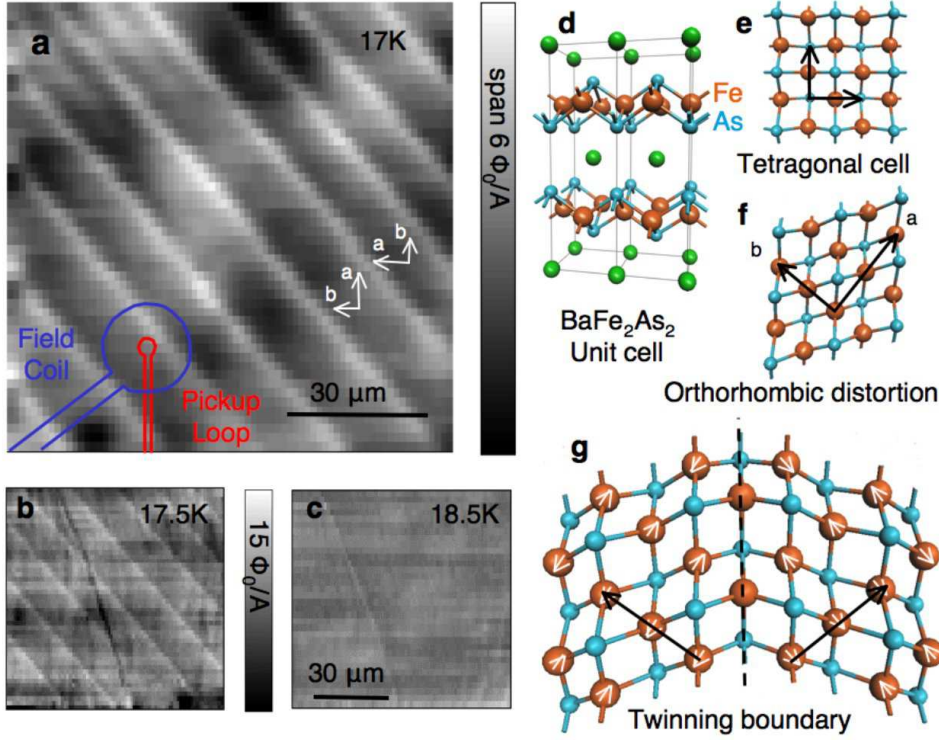


Figure 27. Local susceptibility image in underdoped $\text{Ba}(\text{Fe}_{1-x}\text{Co}_x)_2\text{As}_2$, indicating increased diamagnetic shielding on twin boundaries. (a) Local diamagnetic susceptibility, at $T=17$ K, of the ab face of a sample with $x=0.051$ and $T_c=18.25$ K, showing stripes of enhanced diamagnetic response (white). In addition there is a mottled background associated with local T_c variations that becomes more pronounced as $T \rightarrow T_c$. Overlay: sketch of the scanning SQUID sensor. The size of the pickup loop sets the spatial resolution of the susceptibility images. (b) and (c) Images of the same region at (b) $T=17.5$ K and (c) at $T=18.5$ K show that the stripes disappear above T_c . A topographic feature (scratch) appears in (b) and (c). (d) Crystal structure of a unit cell of the parent compound BaFe_2As_2 . (e) Top view of the FeAs layer with tetragonal symmetry, and (f) an exaggerated view of the orthorhombic distortion that occurs at low temperatures. (g) Schematic of a possible arrangement of spins across a twin boundary in the anti-ferromagnetic state. Reprinted figure with permission from B. Kalisky, J.R. Kirtley, J.G. Analytis, J.-H. Chu, A. Vailionis, I.R. Fisher, and K.A. Moler, *Phys. Rev. B* **81**, 184513 (2010). Copyright 2010 by the American Physical Society.

enhanced superfluid density, it is also difficult to estimate the size of the enhancement in the Cooper pair density from the scanning susceptibility measurements. Nevertheless, Kirtley *et al.* estimate an enhancement in the two-dimensional Cooper pair density in the range between 10^{19} and 10^{20} m^{-2} . For comparison, the two-dimensional electron liquid [293] at the $\text{LaAlO}_3\text{-SiTiO}_3$ interface, which exhibits superconductivity at about 0.2K [294], has a carrier concentration of about 10^{17} m^{-2} . The temperature dependence of the stripe amplitude can be best fit by assuming that the twin boundary has a different critical temperature than the bulk, although no stripes were observed above the bulk T_c .

Kalisky *et al.* also observed that vortices tended to avoid pinning on the twin boundaries, and that they were difficult to drag over the twin boundaries using either a

SQUID susceptometer sensor or a magnetic force microscope tip [292]. The enhancement of supercurrent density, as well as the barrier to vortex motion presented by the twin boundaries, provide two mechanisms for enhanced critical currents in twinned samples. Prozorov *et al.* [295] have noted an enhancement of the critical current of slightly underdoped single crystals of $\text{Ba}(\text{Fe}_{1-x}\text{Co}_x)_2\text{As}_2$, which they associate with twinning.

3.3.3. Spinlike susceptibility There appears to be a component of $1/f^\alpha$ ($\alpha \sim 1$) noise in superconducting devices, which is apparently due to magnetic flux noise, and is remarkably universal [296, 297]. Recently Koch, DiVincenzo, and Clarke (KDC) have proposed that this noise is due to unpaired, metastable spin states [44]. The proposed spin states are bistable, with a broad distribution of activation energies for changing their spin orientation. When the spin state changes it changes the amount of magnetic flux coupling into the superconducting device. Each contributes a Lorentzian with a particular cutoff frequency to the total noise; adding up a large number of Lorentzians with a broad distribution of cutoff frequencies results in noise with $1/f$ distribution [43]. KDC estimate that a density of unpaired spin states of about $5 \times 10^{17} \text{m}^{-2}$ is required to explain universal $1/f$ noise.

Bluhm *et al.* [298] have found a signal in scanning SQUID susceptometry measurements at low temperatures in a number of materials, both metals and insulators, even including Au, that has a paramagnetic response with a temperature dependence consistent with unpaired spins. This susceptibility has a component that is out of phase with the applied field, implying that it could contribute to $1/f$ -like magnetic noise. The density of these spin states is estimated to be in the range of 10^{17}m^{-2} , consistent with the KDC estimate. This implies that scanning SQUID susceptometry could be used as a diagnostic for determining which materials and processes contribute most strongly to $1/f$ noise in superconducting devices.

3.4. Penetration depths

Penetration depths have been inferred from fitting the magnetic images of superconducting vortices for a number of years [79, 80, 299, 32, 300, 301, 302]. An alternate means is to measure the mutual inductance between the SQUID pickup loop and a field coil integrated into the sensor in SSM [72] (Fig. 28). The 2-dimensional Fourier transform of the z -component of the response field in the pickup loop, with a current I in a circular ring of radius R oriented parallel to, and a height z above a homogeneous bulk superconductor with penetration depth λ is given by [303]

$$B_z(k) = -\pi\mu_0 I R \left(\frac{q-k}{q+k} \right) J_1(kR) e^{-2kz}, \quad (26)$$

where $q = \sqrt{k^2 + 1/\lambda^2}$, and J_1 is the order 1 Bessel function of the first kind. Similarly the response field for a thin film superconducting sample with Pearl length Λ is given by [303]

$$B_z(k) = -\pi\mu_0 I R J_1(kR) \frac{e^{-2kz}}{1+k\Lambda}. \quad (27)$$

To a good approximation, if $z \gg \lambda$ the magnetic fields resulting from the screening of the field coil fields by the sample act as if they are due to an image coil spaced by a distance $2h_{eff} = 2(z + \lambda)$ from the real coil, where z is the physical spacing between the sample surface and the field coil. A SQUID sensor with a single circular field coil

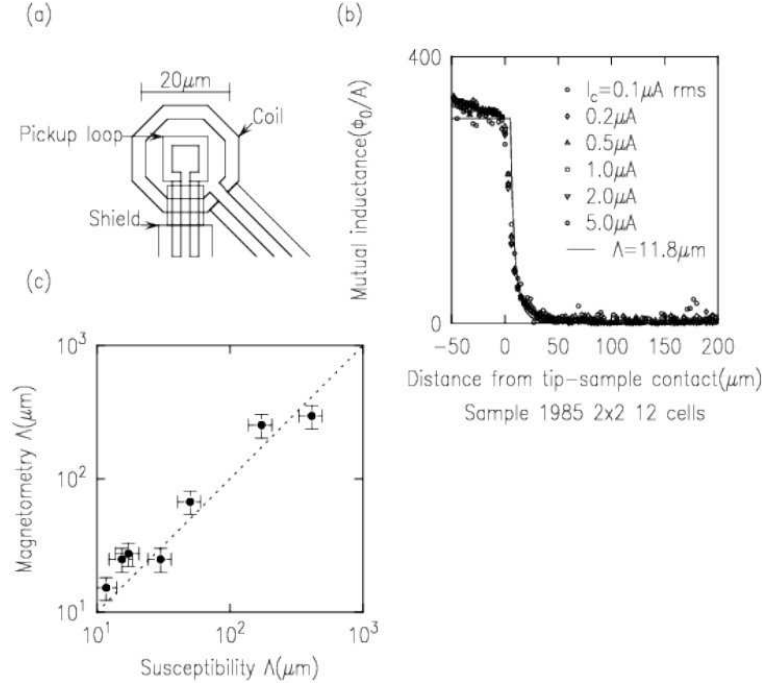


Figure 28. (a) Geometry of a SQUID susceptometer. (b) Mutual inductance between the field coil and the pickup loop, as a function of the spacing z between the SQUID substrate and a thin CBCO film. The symbols are data, taken with various alternating currents through the field coil. The solid line is modeling using Eq. 25, with $\Lambda=11.8\mu\text{m}$. (c) Comparison of the Pearl length Λ for a number of CBCO samples using fitting of SQUID magnetometry images of vortices (vertical axis) vs susceptibility measurements (horizontal axis). Reprinted figure with permission from F. Tafuri, J.R. Kirtley, P.G. Medaglia, P. Orgiani, and G. Balestrino, *Phys. Rev. Lett.* **92**, 157006 (2004). Copyright 2004 by the American Physical Society.

of radius R and a co-planar, coaxial circular pickup loop of radius a oriented parallel to a homogeneous bulk sample surface will have a mutual inductance [304]

$$M = \frac{\mu_0}{2} \pi a^2 \left(\frac{1}{R} - \frac{R^2}{(R^2 + 4h_{eff}^2)^{3/2}} \right). \quad (28)$$

The solid line in Fig. 28(b) is obtained by numerically integrating the 2-D Fourier transform of Eq. (27) over the area of the pickup loop, for various values of z , and fit to the data by varying Λ . Figure 28(c) compares the values obtained for the Pearl lengths for a number of the CBCO samples using magnetometry and susceptometry methods. The two methods agree within experimental error over the range of Pearl lengths present. Since the fitting to the Pearl vortex images was done assuming each vortex has Φ_0 of total flux threading through it, rather than a fractional value [305], this agreement means that the superconducting layers are sufficiently strongly Josephson-coupled that it is energetically favorable for the vortex flux to thread vertically through the superconducting layers, as opposed to escaping between the layers.

Figure 29 shows results from a study using scanning SQUID susceptometry of the penetration depth of the pnictide superconductor LaFePO [304]. This study used the technique of measuring the mutual inductance between the SQUID field coil and pickup loop as a function of spacing z , and then repeating the measurement at fixed z while varying the temperature. Since the mutual inductance is a function of

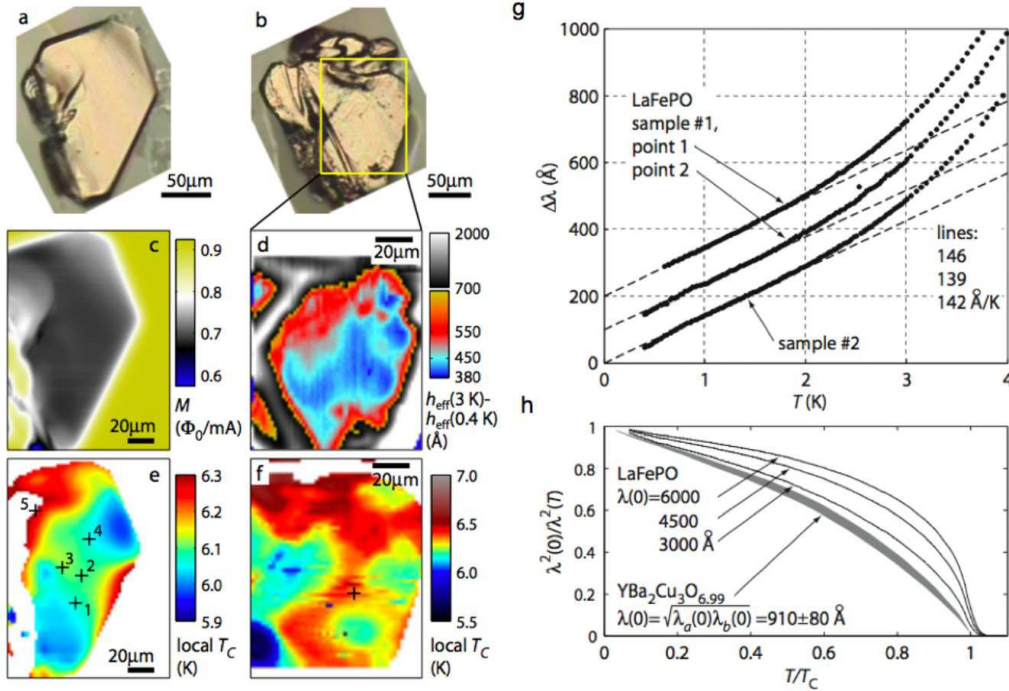


Figure 29. (a,b) Optical micrographs of two single crystals of the pnictide superconductor LaFePO. (c) Susceptibility scan of #1 at $T=0.4\text{K}$. (d) Change in $h_{\text{eff}} = h + \lambda$ between 0.4 and 3K over sample #2. (e,f) Maps of local T_C over the same areas as in (c) and (d). The crosses indicate points where $\Delta\lambda(T)$ data were collected. (g) $\Delta\lambda$ of samples #1, and #2. The dashed lines are fits between $0.7\text{ K} < T < 1.6\text{ K}$. (h) Black lines are possible superfluid densities for LaFePO sample #1, with different $\lambda(0)$. Shaded area: superfluid density of $\text{YBa}_2\text{Cu}_3\text{O}_{6.99}$ from [306],[307]. The width of the shaded area reflects uncertainty in $\lambda(0)$. Reprinted figure with permission from C.W. Hicks, T.M. Lippman, M.E. Huber, J.G. Analytis, J.-H. Chu, A.S. Erickson, I.R. Fisher, and K.A. Moler, Phys. Rev. Lett. **103**, 127003 (2009). Copyright 2009 by the American Physical Society.

$z + \lambda$, the temperature dependence of λ can be inferred from such measurements, even without a detailed model for the mutual inductance. Spatially resolved susceptibility measurements (Fig. 29c-f) showed that the effective height depended on the topography of the sample, with scratches, bumps, and pits effecting the measurements strongly. However, the measured penetration depth and the temperature dependence of the penetration depth was reproducible for positions more than $10\mu\text{m}$ from surface irregularities. In this case the penetration depth had a linear temperature dependence at low temperatures, similar to the cuprate high temperature superconductors, indicative of well formed nodes in the energy gap. It should be noted that in this geometry it is λ_{ab} , the in-plane penetration depth, that controls the mutual inductance.

Perhaps the most promising application of MFM to the study of superconductivity is for high spatial resolution, absolute measurements of penetration depths. There are two ways of inferring superconducting penetration depths from MFM measurements. The first is, as mentioned above, to fit MFM vortex images to a model with the penetration depth as a fitting parameter[301, 302]. While Nazaretski *et al.* modeled

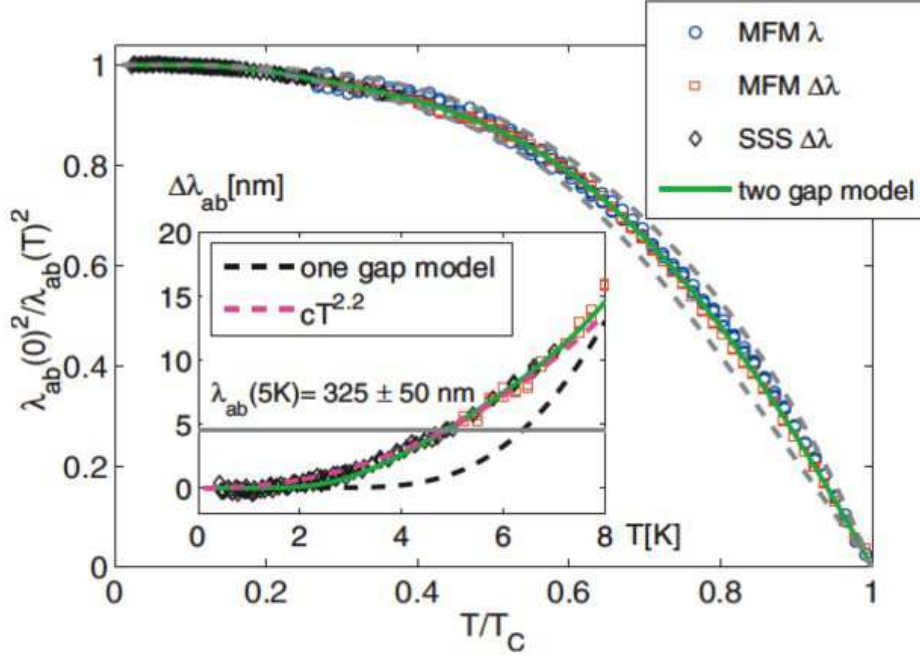


Figure 30. Normalized superfluid density $\rho_s(T)/\rho_s(0) \equiv \lambda_{ab}(0)^2/\lambda_{ab}(T)^2$ vs T for the pnictide superconductor $\text{Ba}(\text{Fe}_{0.95}\text{Co}_{0.05})_2\text{As}_2$. $\Delta\lambda_{ab}(T)$ is determined from MFM (squares) and SSS (diamonds) experiments by measuring the change in the diamagnetic response at fixed height. These values are offset to match the absolute value of $\lambda_{ab}(T)$ by fitting the MFM data to a truncated cone model (circles). The green solid line shows a fit to a two-band s -wave model. The width of the dashed band reflects the uncertainty in $\lambda_{ab}(0)$. Inset: $\Delta\lambda_{ab}(T)$ vs T at low T . Black dashed line: one gap s -wave model with $a=1.5$ and $\Delta_0 = 1.95T_c$. Magenta dashed line: $\Delta\lambda(T) = cT^{2.2}$ ($c=0.14$ nm/ $\text{K}^{2.2}$). Reprinted figure with permission from L. Luan, O.M. Auslaender, T.M. Lippman, C.W. Hicks, B. Kalisky, J.-H. Chu, J.G. Analytis, I.R. Fisher, J.R. Kirtley, and K.A. Moler, *Phys. Rev. B* **81**, 100501 (2010). Copyright 2010 by the American Physical Society.

their tip numerically [301], Luan *et al.* used an analytical approach which is easy to fit to experimental data and not strongly affected by differences between tips [302]. A second method is to consider the interaction between the magnetic material in the tip and its image in the superconducting material due to Meissner screening of the tip fields. Following Xu *et al.* [308], Lu *et al.* [309] wrote the force due to the interaction between the magnetic tip, approximated as a magnetic dipole, and its image in the superconductor as

$$F(z) = \frac{3\mu_0 m_0^2}{32\pi[z + \lambda(T)]^4}, \quad (29)$$

where m_0 is the tip's magnetic moment and z is the physical distance between tip and sample. They fit their measured MFM force derivative curves to the $z \gg \lambda$ approximation

$$\frac{dF(z)}{dz} = -\frac{3\mu_0 m_0^2}{8\pi[z + \lambda(T)]^5}. \quad (30)$$

to obtain the temperature dependence of the penetration depth λ for a single crystal of YBCO. Luan *et al.* [302] used a truncated cone tip model to write

$$\left. \frac{\partial F_z(z, T)}{\partial z} - \frac{\partial F_z(z, T)}{\partial z} \right|_{z=\infty} = A \left\{ \frac{1}{z + \lambda_{ab}(T)} + \frac{h_0}{[z + \lambda_{ab}(T)]^2} + \frac{h_0^2}{2[z + \lambda_{ab}(T)]^3} \right\} \quad (31)$$

for the difference between the force derivative at a given height z and that at large distances, where A , which depends on the tip shape and coating, is determined from fitting experimental data at low temperatures, $\lambda_{ab}(T)$ is the in-plane component of the penetration depth, and h_0 is the truncation height of the tip. Model independent values for $\Delta\lambda(T)$ were obtained by mapping a change in λ to a change in z since they are equivalent. Absolute values for $\lambda(T)$ were obtained by fitting to Eq. 31. Figure 30 shows experimental results for the superfluid density ρ_s of the pnictide superconductor $\text{Ba}(\text{Fe}_{0.95}\text{Co}_{0.05})_2\text{As}_2$ obtained by MFM and SSM measurements. The $\Delta\lambda(T)$ results from MFM measurements were later confirmed by a bulk technique on similar samples [310]. The advantage of MFM is that both the absolute value and high sensitivity relative values of λ can be obtained in the same measurement, so that superfluid density is obtained over the full temperature range and from it the gap structure of the order parameter. Luan *et al.* found a two full-gap model model fit the data well, consistent with the s^{+-} order parameter most frequently discussed in the pnictides. Luan *et al.* also found that ρ_s was uniform on the submicron scale despite highly disordered vortex pinning.

3.5. Manipulation of individual vortices

While there is a vast literature on the properties of superconducting vortices [111], there has been relatively little work on manipulation of individual vortices by scanning magnetic probes. Such manipulation, performed with MFM [112, 119, 116, 311, 312, 313] or SSM [314], can directly measure the interaction of a moving vortex with the local disorder potential [312]. Keay *et al.* used MFM to observe sequential vortex hopping between sites in an array of artificial pinning centers [313]. An example of another such MFM study is shown in Figure 31 [312]. Here vortices in a high quality, detwinned sample of $\text{YBa}_2\text{Cu}_3\text{O}_{6.991}$ are fixed at low temperatures and high scan heights, but at higher temperatures and lower scan heights the tops of the vortices can be dragged by an attractive magnetic interaction with the tip. The vortices are dragged along the fast scan direction until a combination of pinning and elastic forces overcomes the attractive tip-vortex force. The displacement of the vortex in the slow scan direction is much longer than in the fast scan direction, demonstrating a “vortex wiggling” effect: alternating transverse forces markedly enhance vortex dragging. Vortex motion in both the slow and fast scan directions is stochastic. From such measurements Auslaender *et al.* [312] were able to infer the maximum lateral dragging force before the top of the vortices were depinned. They also found a marked in-plane anisotropy in the distance w the top of the vortex was dragged by the tip in the fast scan direction, larger than could be accounted for by the in-plane anisotropy of the vortex core and point pinning. They speculated that a likely source for extra pinning anisotropy is nanoscale clustering of oxygen vacancies along the Cu-O chains in YBCO.

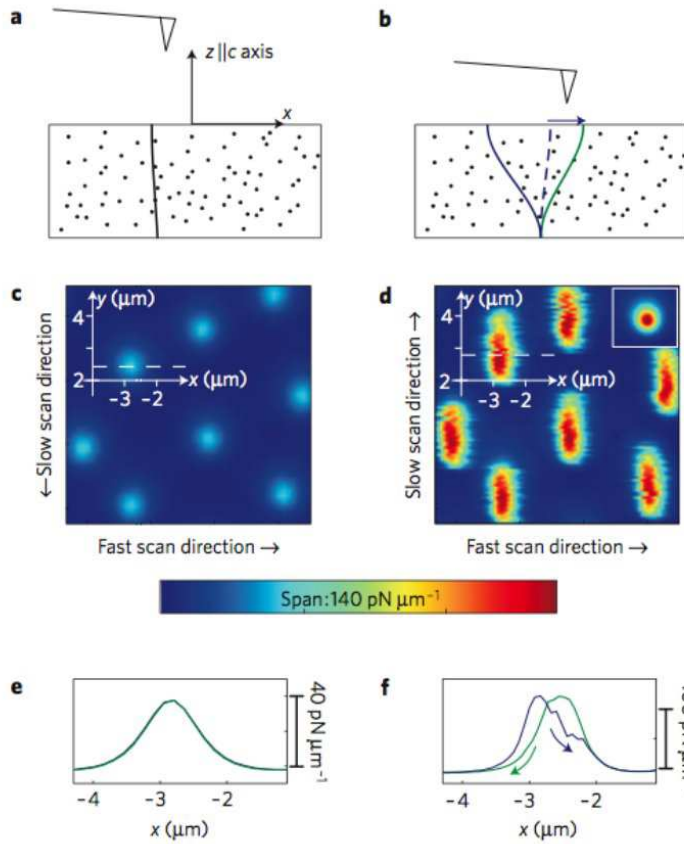


Figure 31. MFM imaging and manipulation of individual vortices in YBCO at $T = 22.3\text{K}$. **a,b** Schematic drawings of an MFM tip (triangle) that attracts a vortex (thick lines) in a sample with randomly distributed pinning sites (dots): at large heights **a** the force between tip and vortex is too weak to move the vortex; at small heights **b** the vortex moves right and then left as the tip rasters over it. **c** MFM image taken at $z=420 \text{ nm}$ (maximum applied lateral force $F_{max}^{lat} \approx 6 \text{ nN}$). **d** $z=170 \text{ nm}$ ($F_{max}^{lat} \approx 12 \text{ nN}$). Inset: Scan taken at a comparable height at $T=5.2\text{K}$. **e** Line cut through the data in **c** along the dashed line, showing the signal from a stationary vortex (blue). Overlapping it is a line cut from the reverse scan (green). **f** Line cut through the data in **d** along the dashed line, showing a typical signal from a dragged vortex. Reprinted by permission from Macmillan Publishers Ltd: O.M. Auslaender, L. Luan, E.W.J. Straver, J.E. Hoffman, N.C. Koshnick, E. Zeldov, D.A. Bonn, R. Liang, W.N. Hardy, and K.A. Moler, *Nature Physics* **5**, 35-39 (2008). Copyright 2008.

4. Conclusions

In summary, there are now many types of scanning magnetic microscopies, each with their own strengths and weaknesses. Of the three covered here, SSM is the most sensitive for low resolution applications, but requires a cooled sensor. MFM has the highest spatial resolution, but also applies the largest fields to the sample. SHM can be used over a broader temperature range than SSM. A major thrust in development has been towards higher spatial resolution, which requires smaller sensors scanned closer to the sample. The scaling of resolution and sensitivity with sensor size and spacing depends both on the technique and the source of field. Many of the applications discussed here have involved the imaging of magnetic flux in special

geometries, unconventional superconductors, or both. Others have involved time dependence, through *e.g.* multiple cooldowns, cooldowns at varying cooling rates, or noise measurements. Some exciting new developments have been scanning susceptibility, which allows the measurement of local penetration depths, spins, and superconducting fluctuations with unprecedented sensitivity and resolution; MFM imaging of Meissner force derivatives, which allow spatially resolved absolute measurements of penetration depths; and controlled manipulation of superconducting vortices. I expect to see many other exciting developments in the future.

5. Acknowledgements

I would like to thank Lan Luan, Beena Kalisky, Cliff Hicks, Danny Hykel and Klaus Hasselbach for carefully reading this review. Any errors are mine, not theirs. I would also like to acknowledge support from the NSF under Grant No. PHY-0425897, by the German Humboldt Foundation, and by the French NanoSciences Fondation, during this work.

References

- [1] J. Bardeen, L. N. Cooper, and J. R. Schrieffer. Microscopic theory of superconductivity. *Phys. Rev.*, 106(1):162–164, 1957.
- [2] J. G. Bednorz and K. A. Müller. Possible high T_c superconductivity in the Ba-La-Cu-O system. *Z. Phys. B*, 64:189–193, 1986.
- [3] M. K. Wu, J. R. Ashburn, C. J. Torng, P. H. Hor, R. L. Meng, L. Gao, Z. J. Huang, Y. Q. Wang, and C. W. Chu. Superconductivity at 93 K in a new mixed-phase Y-Ba-Cu-O compound system at ambient pressure. *Phys. Rev. Lett.*, 58(9):908–910, 1987.
- [4] F. Steglich, J. Aarts, C. D. Bredl, W. Lieke, D. Meschede, W. Franz, and H. Schäfer. Superconductivity in the presence of strong pauli paramagnetism: CeCu_2Si_2 . *Phys. Rev. Lett.*, 43(25):1892–1896, 1979.
- [5] G. R. Stewart. Heavy-fermion systems. *Rev. Mod. Phys.*, 56(4):755–787, 1984.
- [6] Y. Maeno, H. Hashimoto, K. Yoshida, S. Nishizaki, T. Fujita, J. G. Bednorz, and F. Lichtenberg. Superconductivity in a layered perovskite without copper. *Nature*, 372(6506):532–534, 1994.
- [7] Andrew Peter Mackenzie and Yoshiteru Maeno. The superconductivity of Sr_2RuO_4 and the physics of spin-triplet pairing. *Rev. Mod. Phys.*, 75(2):657–712, 2003.
- [8] Hiroki Takahashi, Kazumi Igawa, Kazunobu Arii, Yoichi Kamihara, Masahiro Hirano, and Hideo Hosono. Superconductivity at 43K in an iron-based layered compound $\text{LaO}_{1-x}\text{F}_x\text{FeAs}$. *Nature*, 453:376–378, 2008.
- [9] K. Harada, T. Matsuda, J. Bonevich, M. Igarashi, S. Kondo, G. Pozzi, U. Kawabe, and A. Tonomura. Real-time observation of vortex lattices in a superconductor by electron microscopy. *Nature*, 360:51–53, 1992.
- [10] K. Harada, T. Matsuda, H. Kasai, JE Bonevich, T. Yoshida, U. Kawabe, and A. Tonomura. Vortex configuration and dynamics in $\text{Bi}_2\text{Sr}_{1.8}\text{CaCu}_2\text{O}_x$ thin films by Lorentz microscopy. *Phys. Rev. Lett.*, 71(20):3371–3374, 1993.
- [11] T. Matsuda, K. Harada, H. Kasai, O. Kamimura, and A. Tonomura. Observation of dynamic interaction of vortices with pinning centers by Lorentz microscopy. *Science*, 271(5254):1393, 1996.
- [12] K Harada, O. Kamimura, H. Kasai, T. Matsuda, A. Tonomura, and V.V. Moshchalkov. Direct Observation of Vortex Dynamics in Superconducting Films with Regular Arrays of Defects. *Science*, 274:1167–1170, 1996.
- [13] MR Koblischka and RJ Wijngaarden. Magneto-optical investigations of superconductors. *Supercond. Sci. Tech.*, 8:199–213, 1995.
- [14] DC Larbalestier, LD Cooley, MO Rikel, AA Polyanskii, J. Jiang, S. Patnaik, XY Cai, DM Feldmann, A. Gurevich, AA Squitieri, et al. Strongly linked current flow in polycrystalline forms of the superconductor MgB_2 . *Nature*, 410(6825):186–189, 2001.
- [15] D. Golubchik, E. Polturak, and G. Koren. Correlations beyond the horizon. *arXiv:0911.5613*, 2009.

- [16] A Kapitulnik, J S Dodge, and M M Fejer. High-resolution magneto-optic measurements with a Sagnac interferometer (invited). *J. Appl. Phys.*, 75:6872, 1994.
- [17] BL Petersen, A. Bauer, G. Meyer, T. Creelius, and G. Kaindl. Kerr-rotation imaging in scanning near-field optical microscopy using a modified Sagnac interferometer. *Appl. Phys. Lett.*, 73:538, 1998.
- [18] J. Xia, E. Schemm, G. Deutscher, SA Kivelson, DA Bonn, WN Hardy, R. Liang, W. Siemons, G. Koster, MM Fejer, et al. Polar Kerr-effect measurements of the high-temperature $\text{YBa}_2\text{Cu}_3\text{O}_{6+x}$ superconductor: Evidence for broken symmetry near the pseudogap temperature. *Phys. Rev. Lett.*, 100(12):127002, 2008.
- [19] JYT Wei, N.C. Yeh, CC Fu, and RP Vasquez. Tunneling spectroscopy study of spin-polarized quasiparticle injection effects in cuprate/manganite heterostructures. *J. Appl. Phys.*, 85:5350, 1999.
- [20] A. Wachowiak, J. Wiebe, M. Bode, O. Pietzsch, M. Morgenstern, and R. Wiesendanger. Direct observation of internal spin structure of magnetic vortex cores. *Science*, 298(5593):577, 2002.
- [21] J. Wiebe, A. Wachowiak, F. Meier, D. Haude, T. Foster, M. Morgenstern, and R. Wiesendanger. A 300 mK ultra-high vacuum scanning tunneling microscope for spin-resolved spectroscopy at high energy resolution. *Rev. Sci. Instr.*, 75:4871, 2004.
- [22] E. Lifshitz, I. Dag, ID Litvitn, and G. Hodes. Optically Detected Magnetic Resonance Study of Electron/Hole Traps on CdSe Quantum Dot Surfaces. *J. Phys. Chem. B*, 102(46):9245–9250, 1998.
- [23] B.M. Chernobrod and G.P. Berman. Spin microscope based on optically detected magnetic resonance. *J. Appl. Phys.*, 97:014903, 2005.
- [24] CL Degen. Scanning magnetic field microscope with a diamond single-spin sensor. *Appl. Phys. Lett.*, 92:243111, 2008.
- [25] G. Balasubramanian, IY Chan, R. Kolesov, M. Al-Hmoud, J. Tisler, C. Shin, C. Kim, A. Wojcik, P.R. Hemmer, A. Krueger, et al. Nanoscale imaging magnetometry with diamond spins under ambient conditions. *Nature*, 455(7213):648–651, 2008.
- [26] J R Maze, P L Stanwix, J S Hodges, S Hong, J M Taylor, P Cappellaro, L Jiang, M V G Dutt, E Togan, and A S Zibrov. Nanoscale magnetic sensing with an individual electronic spin in diamond. *Nature*, 455(7213):644–647, 2008.
- [27] WJ Gallagher, SSP Parkin, Y. Lu, XP Bian, A. Marley, KP Roche, RA Altman, SA Rishton, C. Jahnes, TM Shaw, et al. Microstructured magnetic tunnel junctions (invited). *J. Appl. Phys.*, 81:3741, 1997.
- [28] B D Schrag, X Liu, W Shen, and G Xiao. Current density mapping and pinhole imaging in magnetic tunnel junctions via scanning magnetic microscopy. *Appl. Phys. Lett.*, 84:2937–2939, 2004.
- [29] B.D. Schrag, M.J. Carter, X. Liu, J.S. Hoftun, G. Xiao, et al. Magnetic current imaging with magnetic tunnel junction sensors: case study and analysis. In *Conference proceedings from the 32nd International Symposium for Testing and Failure Analysis*, page 13. ASM International (OH), 2006.
- [30] U. Hartmann. Scanning probe microscopy on superconductors: Achievements and challenges. *Appl. Phys. A*, 59(1):41–48, 1994.
- [31] A. De Lozanne. Scanning probe microscopy of high-temperature superconductors. *Supercond. Sci. Technol.*, 12:43–56, 1999.
- [32] S J Bending. Local magnetic probes of superconductors. *Adv. in Phys.*, 48(4):449–535, 1999.
- [33] B. D. Josephson. Possible new effects in superconductive tunnelling. *Phys. Lett.*, 1(7):251 – 253, 1962.
- [34] D. E. McCumber. Tunneling and weak-link superconductor phenomena having potential device applications. *J. Appl. Phys.*, 39(6):2503–2508, 1968.
- [35] W. C. Stewart. Current-voltage characteristics of josephson junctions. *Appl. Phys. Lett.*, 12(8):277–280, 1968.
- [36] T. A. Fulton and L. N. Dunkleberger. Lifetime of the zero-voltage state in Josephson tunnel junctions. *Phys. Rev. B*, 9(11):4760–4768, 1974.
- [37] Richard F. Voss and Richard A. Webb. Macroscopic quantum tunneling in $1\text{-}\mu\text{m}$ Nb josephson junctions. *Phys. Rev. Lett.*, 47(4):265–268, 1981.
- [38] Smilde H J H, Ariando, Blank D A A, Hilgenkamp H, and Rogalla H. π -SQUIDS based on Josephson contacts between high- T_c and low- T_c superconductors. *Phys. Rev. B*, 70:024519, 2004.
- [39] Tesche C D and Clarke J. dc SQUID: Noise and optimization. *J. Low. Temp. Phys.*, 29:301–331, 1977.
- [40] A. J. Dahm, A. Denenstien, D. N. Langenberg, W. H. Parker, D. Rogovin, and D. J. Scalapino.

- Linewidth of the Radiation Emitted by a Josephson Junction. *Phys. Rev. Lett.*, 22(26):1416–1420, 1969.
- [41] Michael J. Stephen. Theory of a Josephson Oscillator. *Phys. Rev. Lett.*, 21(24):1629–1632, 1968.
- [42] Roger H. Koch, D. J. Van Harlingen, and John Clarke. Quantum noise theory for the dc SQUID. *Appl. Phys. Lett.*, 38(5):380–382, 1981.
- [43] P. Dutta, P. Dimon, and PM Horn. Energy Scales for Noise Processes in Metals. *Phys. Rev. Lett.*, 43(9):646–649, 1979.
- [44] R.H. Koch, D.P. Divincenzo, and J. Clarke. Model for 1/f Flux Noise in SQUIDs and Qubits. *Phys. Rev. Lett.*, 98:26, 2007.
- [45] J. Clarke. Principles and applications of SQUIDs. *Proc. IEEE*, 77(8):1208–1223, 1989.
- [46] J R Kirtley and J R Jr Wikswo. Scanning SQUID Microscopy. *Ann. Rev. Mat. Sci.*, 29:117–148, 1999.
- [47] R.P. Welty and J.M. Martinis. A series array of DC SQUIDs. *IEEE Trans. Magn.*, 27(2):2924–2926, 1991.
- [48] M.E. Huber, P.A. Neil, R.G. Benson, D.A. Burns, A.M. Corey, C.S. Flynn, Y. Kitaygorodskaya, O. Massihzadeh, J.M. Martinis, and G.C. Hilton. DC SQUID series array amplifiers with 120 MHz bandwidth. *IEEE Trans. Appl. Supercond.*, 11(1):1251–1256, 2001.
- [49] Bradley J. Roth, Nestor G. Sepulveda, and Jr. John P. Wikswo. Using a magnetometer to image a two-dimensional current distribution. *J. Appl. Phys.*, 65(1):361–372, 1989.
- [50] P. W. Anderson and J. M. Rowell. Probable Observation of the Josephson Superconducting Tunneling Effect. *Phys. Rev. Lett.*, 10(6):230–232, 1963.
- [51] R. C. Jaklevic, John Lambe, A. H. Silver, and J. E. Mercereau. Quantum Interference Effects in Josephson Tunneling. *Phys. Rev. Lett.*, 12(7):159–160, 1964.
- [52] J E Zimmerman and J E Mercereau. Quantized Flux Pinning in Superconducting Niobium. *Phys. Rev. Lett.*, 13(4):125–126, 1964.
- [53] F P Rogers. A device for experimental observation of flux vortices trapped in superconducting thin films. Master’s thesis, Massachusetts Institute of Technology, Cambridge, Massachusetts, 1983.
- [54] A. Mathai, D. Song, Y. Gim, and F. C. Wellstood. One-dimensional magnetic flux microscope based on the dc superconducting quantum interference device. *Appl. Phys. Lett.*, 61(5):598–600, 1992.
- [55] R. C. Black, A. Mathai, F. C. Wellstood, E. Dantsker, A. H. Miklich, D. T. Nemeth, J. J. Kingston, and J. Clarke. Magnetic microscopy using a liquid nitrogen cooled $\text{YBa}_2\text{Cu}_3\text{O}_7$ superconducting quantum interference device. *App. Phys. Lett.*, 62(17):2128–2130, 1993.
- [56] RC Black, FC Wellstood, E. Dantsker, AH Miklich, D. Koelle, F. Ludwig, and J. Clarke. Imaging radio-frequency fields using a scanning SQUID microscope. *Appl. Phys. Lett.*, 66:1267, 1995.
- [57] L.N. Vu and D.J. Van Harlingen. Design and implementation of a scanning SQUID microscope. *IEEE Trans. Appl. Supercond.*, 3(1):1918–1921, 1993.
- [58] L N Vu, M S Wistrom, and D J van Harlingen. Imaging of magnetic vortices in superconducting networks and clusters by scanning SQUID microscopy. *Appl. Phys. Lett.*, 63(12):1693–1695, 1993.
- [59] Y.P. Ma, I.M. Thomas, A. Lauder, and Jr. Wikswo, J.P. A high resolution imaging susceptometer. *IEEE Trans. Appl. Supercond.*, 3(1):1941–1944, 1993.
- [60] Y R Chemla, H L Grossman, Y Poon, R McDermott, R Stevens, M D Alper, and J Clarke. Ultrasensitive magnetic biosensor for homogeneous immunoassay. *Proc. Nat. Acad. Sci.*, 97(26):14268–14272, 2000.
- [61] C C Tsuei, J R Kirtley, C C Chi, Lock See Yu-Jahnes, A Gupta, T Shaw, J Z Sun, and M B Ketchen. Pairing symmetry and flux quantization in a tricrystal superconducting ring of $\text{YBa}_2\text{Cu}_3\text{O}_{7-\delta}$. *Phys. Rev. Lett.*, 73(4):593–596, 1994.
- [62] J. R. Kirtley, M. B. Ketchen, K. G. Stawiasz, J. Z. Sun, W. J. Gallagher, S. H. Blanton, and S. J. Wind. High-resolution scanning squid microscope. *Appl. Phys. Lett.*, 66(9):1138–1140, 1995.
- [63] W. Wernsdorfer, E. Bonet Orozco, K. Hasselbach, A. Benoit, B. Barbara, N. Demoncy, A. Loiseau, H. Pascard, and D. Mailly. Experimental Evidence of the Néel-Brown Model of Magnetization Reversal. *Phys. Rev. Lett.*, 78(9):1791–1794, 1997.
- [64] C Veauvy, K Hasselbach, and D Mailly. Scanning μ -superconduction quantum interference device force microscope. *Rev. Sci. Instrum.*, 73:3825, 2002.
- [65] A G P Troeman, H Derking, B Borger, J Pleikies, D Veldhuis, and H Hilgenkamp. NanoSQUIDs based on niobium constrictions. *Nano Lett.*, 7(7):2152–2156, 2007.
- [66] C Granata, E Esposito, A Vettoliere, L Petti, and M Russo. An integrated superconductive magnetic nanosensor for high-sensitivity nanoscale applications. *Nanotech.*, 19(27):275501–275600, 2008.

- [67] L Hao, J C Macfarlane, J C Gallop, D Cox, J Beyer, D Drung, and T Schurig. Measurement and noise performance of nano-superconducting-quantum-interference devices fabricated by focused ion beam. *Appl. Phys. Lett.*, 92:192507, 2008.
- [68] A. Finkler, Y. Segev, Y. Myasoedov, M.L. Rappaport, L. Neeman, D. Vasyukov, E. Zeldov, M.E. Huber, J. Martin, and A. Yacoby. Self-aligned nanoscale SQUID on a tip. *Nano Lett.*, 10:1046–1049, 2010.
- [69] M B Ketchen, D D Awschalom, W J Gallagher, A W Kleinsasser, R L Sandstrom, J R Rozen, and B Bumble. Design, fabrication, and performance of integrated miniature SQUID susceptometers. *IEEE Trans. Mag.*, 25(2):1212–1215, 1989.
- [70] M B Ketchen and J R Kirtley. Design and performance aspects of pickup loop structures for miniature SQUID magnetometry. *IEEE Trans. Appl. Supercon.*, 5(2 Part 3):2133–2136, 1995.
- [71] N C Koshnick, M E Huber, J A Bert, C W Hicks, J Large, H Edwards, and K A Moler. A Terraced Scanning Superconducting Quantum Interference Device Susceptometer with Sub-Micron Pickup Loops. *Appl. Phys. Lett.*, 93:243101, 2008.
- [72] Brian W. Gardner, Janice C. Wynn, Per G. Björnsson, Eric W. J. Straver, Kathryn A. Moler, John R. Kirtley, and Mark B. Ketchen. Scanning superconducting quantum interference device susceptometry. *Rev. Sci. Instrum.*, 72(5):2361–2364, 2001.
- [73] Martin E. Huber, Nicholas C. Koshnick, Hendrik Bluhm, Leonard J. Archuleta, Tommy Azua, Per G. Björnsson, Brian W. Gardner, Sean T. Halloran, Erik A. Lucero, and Kathryn A. Moler. Gradiometric micro-SQUID susceptometer for scanning measurements of mesoscopic samples. *Rev. Sci. Instrum.*, 79(5):053704, 2008.
- [74] M Freitag, J C Tsang, J R Kirtley, A Carlsen, J Chen, A Troeman, H Hilgenkamp, and P Avouris. Electrically excited, localized infrared emission from single carbon nanotubes. *Nano Lett.*, 6(7):1425–1433, 2006.
- [75] M B Ketchen, D Pearson, A W Kleinsasser, C K Hu, M Smyth, J Logan, K Stawiasz, E Baran, M Jaso, and T Ross. Sub- μm , planarized, Nb-AlO-Nb Josephson process for 125 mm wafers developed in partnership with Si technology. *Appl. Phys. Lett.*, 59:2609–2611, 1991.
- [76] R F Broom and E H Rhoderick. Studies of the Intermediate State in Thin Superconducting Films. *Proc. Phys. Soc.*, 79:586–593, 1962.
- [77] H W Weber and R Riegler. Measurement of the Flux Density Distribution in Type-II Superconductors With Several Micro Field-Probes. *Solid-State Commun.*, 12(2):121–124, 1973.
- [78] T Tamegai, L Krusin-Elbaum, L Civale, P Santhanam, M J Brady, W T Masselink, F Holtzberg, and C Feild. Direct observation of the critical state field profile in a $\text{YBa}_2\text{Cu}_3\text{O}_{7-y}$ single crystal. *Phys. Rev. B*, 45(14):8201–8204, 1992.
- [79] A M Chang, H D Hallen, L Harriott, H F Hess, H L Kao, J Kwo, R E Miller, R Wolfe, J Van der Ziel, and T Y Chang. Scanning Hall probe microscopy. *Appl. Phys. Lett.*, 61:1974–1976, 1992.
- [80] AM Chang, HD Hallen, HF Hess, HL Kao, J. Kwo, and A. Sudbo. Scanning Hall-probe microscopy of a vortex and field fluctuations in $\text{La}_{1.85}\text{Sr}_{0.15}\text{CuO}_4$ films. *Europhys. Lett.*, 20(7):645–50, 1992.
- [81] A Oral, S J Bending, and M Henini. Real-time scanning Hall probe microscopy. *Appl. Phys. Lett.*, 69:1324–1326, 1996.
- [82] A Oral, J C Barnard, S J Bending, I I Kaya, S Ooi, T Tamegai, and M Henini. Direct Observation of Melting of the Vortex Solid in $\text{Bi}_2\text{Sr}_2\text{CaCu}_2\text{O}_8$ Single Crystals. *Phys. Rev. Lett.*, 80:3610–3613, 1998.
- [83] A N Grigorenko, S J Bending, J K Gregory, and R G Humphreys. Scanning Hall probe microscopy of flux penetration into a superconducting YBaCuO thin film strip. *Appl. Phys. Lett.*, 78:1586–1588, 2001.
- [84] R B Dinner, M R Beasley, and K A Moler. Cryogenic scanning Hall-probe microscope with centimeter scan range and submicron resolution. *Rev. Sci. Instr.*, 76:103702, 2005.
- [85] R G Van Veen, A H Verbruggen, E Van der Drift, S Radelaar, S Anders, and H M Jaeger. Micron-sized Hall probes on a Si/SiGe heterostructure as a tool to study vortex dynamics in high-temperature superconducting crystals. *Rev. Sci. Instrum.*, 70:1767–1770, 1999.
- [86] V Cambel, G Karapetrov, P Eliáš, S Hasenöhrl, W K Kwok, J Krause, and J Mañka. Approaching the pT range with a 2DEG InGaAs/InP Hall sensor at 77 K. *Microelect. Eng.*, 51(52):333–342, 2000.
- [87] C W Hicks, L Luan, K A Moler, E Zeldov, and H Shtrikman. Noise characteristics of 100 nm scale GaAs/AlGaAs scanning Hall probes. *Appl. Phys. Lett.*, 90:133512, 2007.
- [88] A. Sandhu, K. Kurosawa, M. Dede, and A. Oral. 50 nm hall sensors for room temperature scanning hall probe microscopy. *Jap. J. Appl. Phys.*, 43:777–778, 2004.
- [89] G. Mihajlović, P. Xiong, S. von Molnár, M. Field, and G.J. Sullivan. InAs quantum well Hall devices for room-temperature detection of single magnetic biomolecular labels. *J. Appl. Phys.*,

- 102:034506, 2007.
- [90] F M Peeters and X Q Li. Hall magnetometer in the ballistic regime. *Appl. Phys. Lett.*, 72:572, 1998.
- [91] A K Geim, S V Dubonos, J G S Lok, I V Grigorieva, J C Maan, L T Hansen, and P E Lindelof. Ballistic hall micromagnetometry. *Appl. Phys. Lett.*, 71:2379, 1997.
- [92] K S Novoselov, S V Morozov, S V Dubonos, M. Missous, A O Volkov, D A Christian, and A Geim. Submicron probes for Hall magnetometry over the extended temperature range from helium to room temperature. *J. Appl. Phys.*, 93:10053, 2003.
- [93] S J Bending and A Oral. Hall effect in a highly inhomogeneous magnetic field distribution. *J. Appl. Phys.*, 81(8):3721–3725, 1997.
- [94] G. Boero, M. Demierre, P.A. Besse, and RS Popovic. Micro-Hall devices: performance, technologies and applications. *Sens. & Act. A*, 106(1-3):314–320, 2003.
- [95] Yongqing Li, Cong Ren, Peng Xiong, Stephan von Molnár, Yuzo Ohno, and Hideo Ohno. Modulation of Noise in Submicron GaAs/AlGaAs Hall Devices by Gating. *Phys. Rev. Lett.*, 93(24):246602, 2004.
- [96] Jens Müller, Stephan von Molnár, Yuzo Ohno, and Hideo Ohno. Decomposition of $1/f$ Noise in $\text{Al}_x\text{Ga}_{1-x}\text{As}/\text{GaAs}$ Hall Devices. *Phys. Rev. Lett.*, 96(18):186601, 2006.
- [97] Y. Martin and HK Wickramasinghe. Magnetic imaging by force microscopy with 1000 Å resolution. *Appl. Phys. Lett.*, 50:1455, 1987.
- [98] D Rugar, H J Mamin, P Guethner, S E Lambert, J E Stern, I McFadyen, and T Yogi. Magnetic force microscopy: General principles and application to longitudinal recording media. *J. Appl. Phys.*, 68:1169–1183, 1990.
- [99] U. Hartmann. Magnetic force microscopy. *Ann. Rev. Mat. Sci.*, 29(1):53–87, 1999.
- [100] C Schönenberger and S.F. Alvarado. Understanding magnetic force microscopy. *Z. Phys. B*, 80:373–383, 1990.
- [101] J Lohau, S Kirsch, A Carl, G Dumpich, and E F Wassermann. Quantitative determination of effective dipole and monopole moments of magnetic force microscopy tips. *J. Appl. Phys.*, 86:3410–3417, 1999.
- [102] G N Phillips, M Siekman, L Abelmann, and J C Lodder. High resolution magnetic force microscopy using focused ion beam modified tips. *Appl. Phys. Lett.*, 81:865–867, 2002.
- [103] D Litvinov and S Khizroev. Orientation-sensitive magnetic force microscopy for future probe storage applications. *Appl. Phys. Lett.*, 81:1878, 2002.
- [104] M R Koblischka, U Hartmann, and T Sulzbach. Improvements of the lateral resolution of the MFM technique. *Thin Solid Films*, 428(1-2):93–97, 2003.
- [105] Z Deng, E Yenilmez, J Leu, J E Hoffman, E W J Straver, H Dai, and K A Moler. Metal-coated carbon nanotube tips for magnetic force microscopy. *Appl. Phys. Lett.*, 85:25, 2004.
- [106] A R Champagne, A J Couture, F Kuemmeth, and D C Ralph. Nanometer-scale scanning sensors fabricated using stencil lithography. *Appl. Phys. Lett.*, 82:1111, 2003.
- [107] S Sun, C B Murray, D Weller, L Folks, and A Moser. Monodisperse FePt nanoparticles and ferromagnetic FePt nanocrystal superlattices. *Science*, 287(5460):1989, 2000.
- [108] J R Kirtley, Z Deng, L Luan, E Yenilmez, H Dai, and K A Moler. Moment switching in nanotube magnetic force probes. *Nanotechnol.*, 18(46):465506–465600, 2007.
- [109] D W Abraham and F A McDonald. Theory of magnetic force microscope images. *Appl. Phys. Lett.*, 56:1181–1183, 1990.
- [110] Y. Otani, T. Kohda, V. Novosad, K. Fukamichi, S. Yuasa, and T. Katayama. Shape induced in-plane magnetic anisotropy reorientation in epitaxial hexagonal close packed cobalt dots. *J. Appl. Phys.*, 87(9):5621–5623, 2000.
- [111] G. Blatter, M. V. Feigel'man, V. B. Geshkenbein, A. I. Larkin, and V. M. Vinokur. Vortices in high-temperature superconductors. *Rev. Mod. Phys.*, 66(4):1125–1388, 1994.
- [112] HJ Hug, A. Moser, I. Parashikov, B. Stiefel, O. Fritz, H.J. Güntherodt, and H. Thomas. Observation and manipulation of vortices in a $\text{YBa}_2\text{Cu}_3\text{O}_7$ thin film with a low temperature magnetic force microscope. *Phys. C*, 235:2695–2696, 1994.
- [113] A. Volodin, K. Temst, Y. Bruynseraede, C. Van Haesendonck, M I Montero, I. K. Schuller, B. Dam, J M Huijbregtse, and R. Griessen. Magnetic force microscopy of vortex pinning at grain boundaries in superconducting thin films. *Phys. C*, 369(1-4):165–170, 2002.
- [114] A. Moser, H. J. Hug, I. Parashikov, B. Stiefel, O. Fritz, H. Thomas, A. Baratoff, H.-J. Güntherodt, and P. Chaudhari. Observation of Single Vortices Condensed into a Vortex-Glass Phase by Magnetic Force Microscopy. *Phys. Rev. Lett.*, 74(10):1847–1850, Mar 1995.
- [115] CW Yuan, Z. Zheng, AL De Lozanne, M. Tortonesi, DA Rudman, and JN Eckstein. Vortex images in thin films of $\text{YBa}_2\text{Cu}_3\text{O}_{7-x}$ and $\text{Bi}_2\text{Sr}_2\text{Ca}_1\text{Cu}_2\text{O}_{8+x}$ obtained by low-temperature magnetic force microscopy. *J. Vac. Sci. Tech. B*, 14(2):1210–1213, 1996.

- [116] A. Moser, HJ Hug, B. Stiefel, and H.J. Güntherodt. Low temperature magnetic force microscopy on YBa₂Cu₃O₇-delta thin films. *J. Magn. Magn. Mat.*, 190:114–123, 1998.
- [117] A. Volodin, K. Temst, C. Van Haesendonck, and Y. Bruynseraede. Imaging of vortices in conventional superconductors by magnetic force microscopy. *Phys. C*, 332(1-4):156–159, 2000.
- [118] A. Volodin, K. Temst, C.V. Haesendonck, and Y. Bruynseraede. Magnetic force microscopy on superconducting NbSe₂ and Nb surfaces. *Phys. B*, 284:815–816, 2000.
- [119] M. Roseman and P. Grütter. Magnetic imaging and dissipation force microscopy of vortices on superconducting Nb films. *Appl. Surf. Sci.*, 188(3-4):416–420, 2002.
- [120] J.R. Clem. Vortex Exclusion from Superconducting Strips and SQUIDS in Weak Perpendicular Ambient Magnetic Fields. *Bull. Am. Phys. Soc.*, 43:401, 1998. paper K36.06 and unpublished.
- [121] M. B. Ketchen, D. J. Herrell, and C. J. Anderson. Josephson cross-sectional model experiment. *J. Appl. Phys.*, 57(7):2550–2574, 1985.
- [122] S. Berman and T. Gheewala. Moat-guarded Josephson SQUIDS. *IEEE Trans. Magn.*, MAG-19:1160–1164, 1983.
- [123] Mark Jeffery, T. Van Duzer, J. R. Kirtley, and M. B. Ketchen. Magnetic imaging of moat-guarded superconducting electronic circuits. *App. Phys. Lett.*, 67(12):1769–1771, 1995.
- [124] C. Veauvy, K. Hasselbach, and D. Mailly. Micro-SQUID microscopy of vortices in a perforated superconducting Al film. *Phys. Rev. B*, 70(21):214513, 2004.
- [125] E. Dantsker, S. Tanaka, and John Clarke. High-T_c super conducting quantum interference devices with slots or holes: Low 1/f noise in ambient magnetic fields. *Appl. Phys. Lett.*, 70(15):2037–2039, 1997.
- [126] A.B.M. Jansman, M. Izquierdo, Flokstra J., and H. Rogalla. Slotted high-T_c dc SQUID magnetometers. *IEEE Trans. Appl. Supercond.*, 9:3290, 1999.
- [127] K.K. Likharev. *Sov. Radiophysics*, 14:722, 1972.
- [128] A.V. Kuznetsov, D.V. Eremenko, and V.N. Trofimov. Onset of flux penetration into a thin superconducting film strip. *Phys. Rev. B*, 59:1507–1513, 1999.
- [129] G.M. Maksimova. Mixed state and critical current in narrow semiconducting films. *Phys. Solid State*, 40:1607–1610, 1998.
- [130] E. Dantsker, S. Tanaka, P.-A. Nilsson, R. Kleiner, and John Clarke. Reduction of 1/f noise in high-T_c dc superconducting quantum interference devices cooled in an ambient magnetic field. *Appl. Phys. Lett.*, 69(26):4099–4101, 1996.
- [131] G. Stan, Stuart B. Field, and J. M. Martinis. Critical field for complete vortex expulsion from narrow superconducting strips. *Phys. Rev. Lett.*, 92(9):097003, 2004.
- [132] K. Suzuki, Li. Yijie, T. Utagawa, and Tanabe K. Magnetic imaging of NdBa₂Cu₃O_y thin-film patterns with slots. *Appl. Phys. Lett.*, 76:3615–3617, 2000.
- [133] K H Kuit, J R Kirtley, W van der Veur, C G Molenaar, F J G Roesthuis, A G P Troeman, J R Clem, H Hilgenkamp, H Rogalla, and J Flokstra. Vortex trapping and expulsion in thin-film YBa₂Cu₃O_{7-δ} strips. *Phys. Rev. B*, 77:13, 2008.
- [134] Eric Bronson, Martin P. Gelfand, and Stuart B. Field. Equilibrium configurations of Pearl vortices in narrow strips. *Phys. Rev. B*, 73(14):144501, 2006.
- [135] Richard A. Webb, Richard F. Voss, G. Grinstein, and P. M. Horn. Magnetic field behavior of a josephson-junction array: Two-dimensional flux transport on a periodic substrate. *Phys. Rev. Lett.*, 51(8):690–693, 1983.
- [136] R.F. Voss and R.A. Webb. Phase coherence in a weakly coupled array of 20 000 Nb Josephson junctions. *Physical Review B*, 25:3446–3449, 1982.
- [137] D Sanchez and Berchier J.L. Properties of nxn square arrays of proximity effect bridges. *J. Low Temp. Phys.*, 43:65–89, 1981.
- [138] D. J. Resnick, J. C. Garland, J. T. Boyd, S. Shoemaker, and R. S. Newrock. Kosterlitz-thouless transition in proximity-coupled superconducting arrays. *Phys. Rev. Lett.*, 47(21):1542–1545, 1981.
- [139] David W. Abraham, C. J. Lobb, M. Tinkham, and T. M. Klapwijk. Resistive transition in two-dimensional arrays of superconducting weak links. *Phys. Rev. B*, 26(9):5268–5271, 1982.
- [140] R. Fazio and H. Van Der Zant. Quantum phase transitions and vortex dynamics in superconducting networks. *Physics Reports*, 355(4):235–334, 2001.
- [141] J.M. Kosterlitz and D.J. Thouless. Ordering, metastability and phase transitions in two-dimensional systems. *J. Phys. C*, 6:1181, 1973.
- [142] S. Teitel and C. Jayaprakash. Josephson-junction arrays in transverse magnetic fields. *Phys. Rev. Lett.*, 51(21):1999–2002, 1983.
- [143] H. D. Hallen, R. Seshadri, A. M. Chang, R. E. Miller, L. N. Pfeiffer, K. W. West, C. A. Murray, and H. F. Hess. Direct spatial imaging of vortices in a superconducting wire network. *Phys. Rev. Lett.*, 71(18):3007–3010, 1993.

- [144] Dragomir Davidović, Suman Kumar, Daniel H. Reich, Jeffrey Siegel, S. B. Field, R. C. Tiberio, R. Hey, and K. Ploog. Correlations and disorder in arrays of magnetically coupled superconducting rings. *Phys. Rev. Lett.*, 76(5):815–818, 1996.
- [145] D. Davidovic, S. Kumar, D.H. Reich, J. Siegel, SB Field, RC Tiberio, R. Hey, and K. Ploog. Magnetic correlations, geometrical frustration, and tunable disorder in arrays of superconducting rings. *Phys. Rev. B*, 55(10):6518–6540, 1997.
- [146] S. Teitel and C. Jayaprakash. Phase transitions in frustrated two-dimensional xy models. *Phys. Rev. B*, 27(1):598–601, 1983.
- [147] Mohammad R. Kolahchi and Joseph P. Straley. Ground state of the uniformly frustrated two-dimensional xy model near $f=1/2$. *Phys. Rev. B*, 43(10):7651–7654, Apr 1991.
- [148] Thomas C. Halsey. Josephson-junction arrays in transverse magnetic fields: Ground states and critical currents. *Phys. Rev. B*, 31(9):5728–5745, 1985.
- [149] B. Pannetier, J. Chaussy, R. Rammal, and J. C. Villegier. Experimental fine tuning of frustration: Two-dimensional superconducting network in a magnetic field. *Phys. Rev. Lett.*, 53(19):1845–1848, 1984.
- [150] M. A. Itzler, A. M. Behrooz, C. W. Wilks, R. Bojko, and P. M. Chaikin. Commensurate states in disordered networks. *Phys. Rev. B*, 42(13):8319–8331, 1990.
- [151] M. S. Rzchowski, S. P. Benz, M. Tinkham, and C. J. Lobb. Vortex pinning in Josephson-junction arrays. *Phys. Rev. B*, 42(4):2041–2050, 1990.
- [152] C. J. Lobb, David W. Abraham, and M. Tinkham. Theoretical interpretation of resistive transition data from arrays of superconducting weak links. *Phys. Rev. B*, 27(1):150–157, Jan 1983.
- [153] K. Runge and B. Pannetier. First decoration of superconducting networks. *Europhys. Lett.*, 24(9):737–742, 1993.
- [154] S. B. Field, S. S. James, J. Barentine, V. Metlushko, G. Crabtree, H. Shtrikman, B. Ilic, and S. R. J. Brueck. Vortex configurations, matching, and domain structure in large arrays of artificial pinning centers. *Phys. Rev. Lett.*, 88(6):067003, 2002.
- [155] D. J. Scalapino. The case for $d_{x^2-y^2}$ pairing in the cuprate superconductors. *Phys. Rep.*, 250(6):329 – 365, 1995.
- [156] J F Annett, N D Goldenfeld, and A.J. Leggett. In D M Ginsberg, editor, *Physical Properties of High Temperature Superconductors*, volume 5, chapter 6. World Scientific, Singapore, 1996.
- [157] D. J. Van Harlingen. Phase-sensitive tests of the symmetry of the pairing state in the high-temperature superconductors—evidence for $d_{x^2-y^2}$ symmetry. *Rev. Mod. Phys.*, 67(2):515–535, 1995.
- [158] C. C. Tsuei and J. R. Kirtley. Pairing symmetry in cuprate superconductors. *Rev. Mod. Phys.*, 72(4):969, 2000.
- [159] D. A. Wollman, D. J. Van Harlingen, W. C. Lee, D. M. Ginsberg, and A. J. Leggett. Experimental determination of the superconducting pairing state in YBCO from the phase coherence of YBCO-Pb dc SQUIDs. *Phys. Rev. Lett.*, 71(13):2134–2137, 1993.
- [160] D. A. Wollman, D. J. Van Harlingen, J. Giapintzakis, and D. M. Ginsberg. Evidence for $d_{x^2-y^2}$ Pairing from the Magnetic Field Modulation of $\text{YBa}_2\text{Cu}_3\text{O}_{7-\delta}$ -Pb Josephson Junctions. *Phys. Rev. Lett.*, 74(5):797–800, 1995.
- [161] D. A. Brawner and H. R. Ott. Evidence for an unconventional superconducting order parameter in $\text{YBa}_2\text{Cu}_3\text{O}_{6.9}$. *Phys. Rev. B*, 50(9):6530–6533, 1994.
- [162] I. Iguchi and Z. Wen. Experimental evidence for a d-wave pairing state in $\text{YBa}_2\text{Cu}_3\text{O}_{7-y}$ from a study of $\text{YBa}_2\text{Cu}_3\text{O}_{7-y}$ /insulator/Pb Josephson tunnel junctions. *Phys. Rev. B*, 49(17):12388–12391, 1994.
- [163] J. H. Miller, Jr., Q. Y. Ying, Z. G. Zou, N. Q. Fan, J. H. Xu, M. F. Davis, and J. C. Wolfe. Use of Tricrystal Junctions to Probe the Pairing State Symmetry of $\text{YBa}_2\text{Cu}_3\text{O}_{7-\delta}$. *Phys. Rev. Lett.*, 74(12):2347–2350, 1995.
- [164] K. A. Kouznetsov, A. G. Sun, B. Chen, A. S. Katz, S. R. Bahcall, John Clarke, R. C. Dynes, D. A. Gajewski, S. H. Han, M. B. Maple, J. Giapintzakis, J.-T. Kim, and D. M. Ginsberg. c -axis Josephson Tunneling between $\text{YBa}_2\text{Cu}_3\text{O}_{7-\delta}$ and Pb: Direct Evidence for Mixed Order Parameter Symmetry in a High- T_c Superconductor. *Phys. Rev. Lett.*, 79(16):3050–3053, 1997.
- [165] V B Geshkenbein and A I Larkin. Josephson effect in superconductors with heavy fermions. *JETP Lett.*, 43:395, 1986.
- [166] V. B. Geshkenbein, A. I. Larkin, and A. Barone. Vortices with half magnetic flux quanta in “heavy-fermion” superconductors. *Phys. Rev. B*, 36(1):235–238, 1987.
- [167] J R Kirtley, C C Tsuei, J Z Sun, C C Chi, Lock See Yu-Jahnes, A Gupta, M Rupp, and M.B. Ketchen. Symmetry of the order parameter in the high- T_c superconductor $\text{YBa}_2\text{Cu}_3\text{O}_{7-\delta}$. *Nature*, 373:225, 1995.

- [168] CC Tsuei, JR Kirtley, M. Rupp, JZ Sun, L.S. Yu-Jahnes, CC Chi, A. Gupta, and MB Ketchen. Flux quantization in tricrystal cuprate rings—a new probe of pairing symmetry. *J. Phys. Chem. Solids*, 56(12):1787–1795, 1995.
- [169] J R Kirtley, C C Tsuei, M Rupp, J Z Sun, L S Yu-Jahnes, A Gupta, M B Ketchen, K A Moler, and M Bhushan. Direct imaging of integer and half-integer Josephson vortices in high- T_c grain boundaries. *Phys. Rev. Lett.*, 76:1336, 1996.
- [170] C C Tsuei, J R Kirtley, M Rupp, J Z Sun, A Gupta, M B Ketchen, C A Wang, Z F Ren, J H Wang, and M Bhushan. Half-integer flux quantum effect and pairing symmetry in high- T_c tetragonal $Tl_2Ba_2CuO_{6+\delta}$ films. *Science*, 272:329, 1996.
- [171] J R Kirtley, C C Tsuei, H Raffy, Z Z Li, A Gupta, J Z Sun, and S Megert. Half-integer flux quantum effect in tricrystal $Bi_2Sr_2CaCu_2O_{8+\delta}$. *Europhys. Lett.*, 36:707, 1996.
- [172] C. C. Tsuei, J. R. Kirtley, G. Hammerl, J. Mannhart, H. Raffy, and Z. Z. Li. Robust $d_{x^2-y^2}$ Pairing Symmetry in Hole-Doped Cuprate Superconductors. *Phys. Rev. Lett.*, 93(18):187004, 2004.
- [173] C. C. Tsuei and J. R. Kirtley. Phase-sensitive evidence for d -wave pairing symmetry in electron-doped cuprate superconductors. *Phys. Rev. Lett.*, 85(1):182–185, 2000.
- [174] J R Kirtley, C C Tsuei, and K A Moler. Temperature dependence of the half-integer magnetic flux quantum. *Science*, 285:1373, 1999.
- [175] A. Mathai, Y. Gim, R. C. Black, A. Amar, and F. C. Wellstood. Experimental Proof of a Time-Reversal-Invariant Order Parameter with a π shift in $YBa_2Cu_3O_{7-\delta}$. *Phys. Rev. Lett.*, 74(22):4523–4526, 1995.
- [176] Akira Sugimoto, Tetsuji Yamaguchi, and Ienari Iguchi. Temperature dependence of half flux quantum in $YBa_2Cu_3O_{7-y}$ tricrystal thin film observed by scanning SQUID microscopy. *Physica C*, 367(1-4):28 – 32, 2002.
- [177] K Cedergren, J R Kirtley, Bauch T, Rotoli G, Troeman A, Hilgenkamp H, Tafuri F, and Lombardi F. Interplay between static and dynamic properties of semifluxons in $YBa_2Cu_3O_{7-\delta}$ $0-\pi$ Josephson junctions. *Phys. Rev. Lett.*, 104:177003, 2010.
- [178] H. Hilgenkamp and J. Mannhart. Grain boundaries in high- T_c superconductors. *Rev. Mod. Phys.*, 74(2):485–549, 2002.
- [179] H. Hilgenkamp, J. Mannhart, and B. Mayer. Implications of $d_{x^2-y^2}$ symmetry and faceting for the transport properties of grain boundaries in high- T_c superconductors. *Phys. Rev. B*, 53(21):14586–14593, 1996.
- [180] J Mannhart, H Hilgenkamp, B Mayer, C Gerber, J R Kirtley, K A Moler, and M Sigrist. Generation of magnetic flux by single grain boundaries of $YBa_2Cu_3O_{7-x}$. *Phys. Rev. Lett.*, 77(13):2782–2785, 1996.
- [181] J. R. Kirtley, K. A. Moler, and D. J. Scalapino. Spontaneous flux and magnetic-interference patterns in $0-\pi$ Josephson junctions. *Phys. Rev. B*, 56(2):886–891, 1997.
- [182] R. G. Mints, Ilya Papiashvili, J. R. Kirtley, H. Hilgenkamp, G. Hammerl, and J. Mannhart. Observation of Splintered Josephson Vortices at Grain Boundaries in $YBa_2Cu_3O_{7-\delta}$. *Phys. Rev. Lett.*, 89(6):067004, 2002.
- [183] Henk-Jan H. Smilde, Hans Hilgenkamp, Guus Rijnders, Horst Rogalla, and Dave H. A. Blank. Enhanced transparency ramp-type Josephson contacts through interlayer deposition. *Appl. Phys. Lett.*, 80(24):4579–4581, 2002.
- [184] H Hilgenkamp, Ariando, H J Smilde, D H A Blank, H Rogalla, J R Kirtley, and C C Tsuei. Ordering and manipulation of the magnetic moments in large-scale superconducting π -loop arrays. *Nature*, 422:50, 2003.
- [185] F. Lombardi, F. Tafuri, F. Ricci, F. Miletto Granozio, A. Barone, G. Testa, E. Sarnelli, J. R. Kirtley, and C. C. Tsuei. Intrinsic d -Wave Effects in $YBa_2Cu_3O_{7-\delta}$ Grain Boundary Josephson Junctions. *Phys. Rev. Lett.*, 89(20):207001, 2002.
- [186] H. J. H. Smilde, A. A. Golubov, Ariando, G. Rijnders, J. M. Dekkers, S. Harkema, D. H. A. Blank, H. Rogalla, and H. Hilgenkamp. Admixtures to d -Wave Gap Symmetry in Untwinned $YBa_2Cu_3O_7$ Superconducting Films Measured by Angle-Resolved Electron Tunneling. *Phys. Rev. Lett.*, 95(25):257001, 2005.
- [187] J R Kirtley, C C Tsuei, V Ariando, S Harkema, and H Hilgenkamp. Angle-resolved phase-sensitive determination of the in-plane symmetry in $YBa_2Cu_3O_{7-\delta}$. *Nature Phys.*, 2(5):190–194, 2006.
- [188] Kirtley J R, Tsuei C C, Ariando, Smilde H J H, and Hilgenkamp H. Antiferromagnetic ordering in arrays of superconducting π -rings. *Phys. Rev. B*, 72(21):214521–214521, 2005.
- [189] A. O’Hare, F.V. Kusmartsev, M.S. Laad, and K.I. Kugel. Evidence of superstructures at low temperatures in frustrated spin systems. *Phys. C*, 437-438:230 – 233, 2006. Proceedings of the Fourth International Conference on Vortex Matter in Nanostructured Superconductors VORTEX IV.

- [190] Wheatley J M, Hsu T C, and Anderson P W. Interlayer effects in high- T_c superconductors. *Nature*, 333:121, 1988.
- [191] P. W. Anderson. Comment on “Anomalous spectral weight transfer at the superconducting transition of $\text{Bi}_2\text{Sr}_2\text{CaCu}_2\text{O}_{8+\delta}$ ”. *Phys. Rev. Lett.*, 67(5):660, 1991.
- [192] P. W. Anderson. Experimental Constraints on the Theory of High- T_c Superconductivity. *Science*, 256(5063):1526–1531, 1992.
- [193] Sudip Chakravarty, Asle Sudbo, Philip W. Anderson, and Steven Strong. Interlayer Tunneling and Gap Anisotropy in High-Temperature Superconductors. *Science*, 261(5119):337–340, 1993.
- [194] P. W. Anderson. Interlayer Tunneling Mechanism for High- T_c Superconductivity: Comparison with c Axis Infrared Experiments. *Science*, 268(5214):1154–1155, 1995.
- [195] K A Moler, J R Kirtley, D G Hinks, T W Li, and M Xu. Images of Interlayer Josephson Vortices in $\text{Tl}_2\text{Ba}_2\text{CuO}_{6+\delta}$. *Science*, 279(5354):1193–1196, 1998.
- [196] J. R. Kirtley, K. A. Moler, G. Villard, and A. Maignan. c -Axis Penetration Depth of Hg-1201 Single Crystals. *Phys. Rev. Lett.*, 81(10):2140–2143, 1998.
- [197] J. R. Kirtley, V. G. Kogan, J. R. Clem, and K. A. Moler. Magnetic field of an in-plane vortex outside a layered superconductor. *Phys. Rev. B*, 59(6):4343–4348, 1999.
- [198] A. A. Tsvetkov, D. van der Marel, K. A. Moler, J. R. Kirtley, J. L. de Boer, A. Meetsma, Z. F. Ren, N. Koleshnikov, D. Dulic, A. Damascelli, M. Gruninger, J. Schutzmann, J. W. van der Eb, H. S. Somal, and Wang J. H. Global and local measures of the intrinsic Josephson coupling in $\text{Tl}_2\text{Ba}_2\text{CuO}_6$ as a test of the interlayer tunneling model. *Nature*, 395:360–362, 1999.
- [199] K. Pearl. Current distribution in superconducting films carrying quantized fluxoids. *Appl. Phys. Lett.*, 5:65–66, 1964.
- [200] V. G. Kogan, V. V. Dobrovitski, J. R. Clem, Yasunori Mawatari, and R. G. Mints. Josephson junction in a thin film. *Phys. Rev. B*, 63(14):144501, 2001.
- [201] V. G. Kogan. Interaction of vortices in thin superconducting films and the Berezinskii-Kosterlitz-Thouless transition. *Phys. Rev. B*, 75(6):064514, 2007.
- [202] AN Grigorenko, SJ Bending, MJ Van Bael, M. Lange, VV Moshchalkov, H. Fangohr, and PAJ de Groot. Symmetry locking and commensurate vortex domain formation in periodic pinning arrays. *Physical review letters*, 90(23):237001, 2003.
- [203] V. G. Kogan, A. Yu. Simonov, and M. Ledvij. Magnetic field of vortices crossing a superconductor surface. *Phys. Rev. B*, 48(1):392–397, 1993.
- [204] Yu. E. Lozovik and E. A. Rakoch. Energy barriers, structure, and two-stage melting of microclusters of vortices. *Phys. Rev. B*, 57(2):1214–1225, Jan 1998.
- [205] H. J. Fink and A. G. Presson. Magnetic Irreversible Solution of the Ginzburg-Landau Equations. *Phys. Rev.*, 151(1):219–228, 1966.
- [206] Chibotaru L F, Ceulemans A, Bruyndoncx V, and Moshchalkov V V. Symmetry-induced formation of antivortices in mesoscopic superconductors. *Nature*, 48:833–835, 2000.
- [207] L. F. Chibotaru, A. Ceulemans, V. Bruyndoncx, and V. V. Moshchalkov. Vortex entry and nucleation of antivortices in a mesoscopic superconducting triangle. *Phys. Rev. Lett.*, 86(7):1323–1326, 2001.
- [208] I. V. Grigorieva, W. Escoffier, J. Richardson, L. Y. Vinnikov, S. Dubonos, and V. Oboznov. Direct observation of vortex shells and magic numbers in mesoscopic superconducting disks. *Phys. Rev. Lett.*, 96(7):077005, 2006.
- [209] T. Nishio, S. Okayasu, J. Suzuki, and K. Kadowaki. Penetration of vortices into microsuperconductors observed with a scanning SQUID microscope. *Phys. C*, 412:379–384, 2004.
- [210] VV Moshchalkov, L. Gielen, C. Strunk, R. Jonckheere, X. Qiu, C. Van Haesendonck, and Y. Bruynseraede. Effect of sample topology on the critical fields of mesoscopic superconductors. *Nature*, 373:319–322, 1995.
- [211] T. Nishio, Q. Chen, W. Gillijns, K. De Keyser, K. Vervaeke, and V V Moshchalkov. Scanning Hall probe microscopy of vortex patterns in a superconducting microsquare. *Phys. Rev. B*, 77:012502, 2008.
- [212] M. Matsumoto and M. Sigrist. Quasiparticle States near the Surface and the Domain Wall in a $p_x + ip_y$ -Wave Superconductor. *J. Phys. Soc. Jap.*, 68:994–1007, 1999.
- [213] GM Luke, Y. Fudamoto, KM Kojima, MI Larkin, J. Merrin, B. Nachumi, Y. Maeno, ZQ Mao, and Y. Mori. Time-reversal symmetry-breaking superconductivity in Sr_2RuO_4 . *Nature*, 394(6693):558–561, 1998.
- [214] P.G. Björnsson, Y. Maeno, M.E. Huber, and K.A. Moler. Scanning magnetic imaging of Sr_2RuO_4 . *Phys. Rev. B*, 72(1):12504–12504, 2005.
- [215] JR Kirtley, C. Kallin, CW Hicks, E.A. Kim, Y. Liu, KA Moler, Y. Maeno, and KD Nelson. Upper limit on spontaneous supercurrents in Sr_2RuO_4 . *Phys. Rev. B*, 76(1):14526, 2007.
- [216] Clifford W. Hicks, John R. Kirtley, Thomas M. Lippman, Nicholas C. Koshnick, Martin E. Huber,

- Yosheritu Maeno, William M. Yuhasz, M. Brian Maple, and Kathryn A. Moler. Limits on Superconductivity-Related Magnetization in Sr_2RuO_4 and $\text{PrOs}_4\text{Sb}_{12}$ from Scanning SQUID Microscopy. *Phys. Rev. B*, 81:214501, 2010.
- [217] KD Nelson, ZQ Mao, Y. Maeno, and Y. Liu. Odd-parity superconductivity in Sr_2RuO_4 . *Science*, 306(5699):1151, 2004.
- [218] F. Kidwingira, JD Strand, DJ Van Harlingen, and Y. Maeno. Dynamical superconducting order parameter domains in Sr_2RuO_4 . *Science*, 314(5803):1267, 2006.
- [219] S. Raghu, A. Kapitulnik, and SA Kivelson. Hidden quasi one-dimensional superconductivity in Sr_2RuO_4 . *Arxiv preprint arXiv:1003.2266*, 2010.
- [220] V O Dolocan, C Veauvy, F Servant, P Lejay, K Hasselbach, Y Liu, and D Mailly. Observation of vortex coalescence in the anisotropic spin-triplet superconductor Sr_2RuO_4 . *Phys. Rev. Lett.*, 95(9):097004, 2005.
- [221] V. O. Dolocan, P. Lejay, D. Mailly, and K. Hasselbach. Observation of two species of vortices in the anisotropic spin-triplet superconductor Sr_2RuO_4 . *Phys. Rev. B*, 74(14):144505, 2006.
- [222] A. Grigorenko, S. Bending, T. Tamegai, S. Ooi, and M. Henini. A one-dimensional chain state of vortex matter. *Nature*, 414:728–731, 2001.
- [223] SS Saxena, P. Agarwal, K. Ahilan, FM Grosche, RKW Haselwimmer, MJ Steiner, E. Pugh, IR Walker, SR Julian, P. Monthoux, et al. Superconductivity on the border of itinerant-electron ferromagnetism in UGe_2 . *Nature*, 406(6796):587–592, 2000.
- [224] D. Aoki, Huxley A., E. Ressouche, D. Braithwaite, J. Flouquet, J.P. Brison, E. Lhotel, and C. Paulsen. Coexistence of superconductivity and ferromagnetism in URhGe . *Nature*, 413(6856):613–616, 2001.
- [225] NT Huy, A. Gasparini, DE De Nijs, Y. Huang, JCP Klaasse, T. Gortenmulder, A. De Visser, A. Hamann, T. Görlach, and H. Löhneysen. Superconductivity on the border of weak itinerant ferromagnetism in UCoGe . *Phys. Rev. Lett.*, 99(6):067006, 2007.
- [226] E. Slooten, T. Naka, A. Gasparini, YK Huang, and A. De Visser. Enhancement of superconductivity near the ferromagnetic quantum critical point in UCoGe . *Phys. Rev. Lett.*, 103(9):97003, 2009.
- [227] M. Tachiki, H. Matsumoto, T. Koyama, and H. Umezawa. Self-induced vortices in magnetic superconductors. *Solid State Commun.*, 34(1):19 – 23, 1980.
- [228] DE Moncton, DB McWhan, PH Schmidt, G. Shirane, W. Thomlinson, MB Maple, HB MacKay, LD Wolf, Z. Fisk, and DC Johnston. Oscillatory Magnetic Fluctuations near the Superconductor-to-Ferromagnet Transition in ErRh_4B_4 . *Phys. Rev. Lett.*, 45(25):2060–2063, 1980.
- [229] JW Lynn, G. Shirane, W. Thomlinson, and RN Shelton. Competition between Ferromagnetism and Superconductivity in HoMo_6S_8 . *Phys. Rev. Lett.*, 46(5):368–371, 1981.
- [230] T. Ohta, T. Hattori, K. Ishida, Y. Nakai, E. Osaki, K. Deguchi, K. Noriaki, and I. Satoh. Microscopic Coexistence of Ferromagnetism and Superconductivity in Single-Crystal UCoGe . *J. Phys. Soc. Jap.*, 79(2):023707, 2010.
- [231] J. Fritzsche, R. B. G. Kramer, and V. V. Moshchalkov. Visualization of the vortex-mediated pinning of ferromagnetic domains in superconductor-ferromagnet hybrids. *Phys. Rev. B*, 79(13):132501, 2009.
- [232] MJ Van Bael, J. Bekaert, K. Temst, L. Van Look, VV Moshchalkov, Y. Bruynseraede, GD Howells, AN Grigorenko, SJ Bending, and G. Borghs. Local observation of field polarity dependent flux pinning by magnetic dipoles. *Phys. Rev. Lett.*, 86(1):155–158, 2001.
- [233] Mariela Menghini, R. B. G. Kramer, A. V. Silhanek, J. Sautner, V. Metlushko, K. De Keyser, J. Fritzsche, N. Verellen, and V. V. Moshchalkov. Direct visualization of magnetic vortex pinning in superconductors. *Phys. Rev. B*, 79(14):144501, 2009.
- [234] D M Silevitch, D H Reich, C L Chien, S B Field, and H Shtrikman. Imaging and magnetotransport in superconductor/magnetic dot arrays. *J. Appl. Phys.*, 89:7478, 2001.
- [235] H Bluhm, S E Sebastian, J W Guikema, I R Fisher, and K A Moler. Scanning Hall probe imaging of $\text{ErNi}_2\text{B}_2\text{C}$. *Phys. Rev. B*, 73:014514, 2006.
- [236] PC Canfield, SL Bud'Ko, and BK Cho. Possible co-existence of superconductivity and weak ferromagnetism in $\text{ErNi}_2\text{B}_2\text{C}$. *Physica C*, 262(3-4):249–254, 1996.
- [237] P.W. Anderson. The resonating valence bond state in La_2CuO_4 and superconductivity. *Science*, 235:1196–1198, 1987.
- [238] T. Senthil and M.P.A. Fisher. Fractionalization in the cuprates: Detecting the topological order. *Phys. Rev. Lett.*, 86:292–295, 2001.
- [239] D A Bonn, Wynn J C, Gardner B W, Lin Yu-Ju, Liang R, Hardy W N, Kirtley J R, and Moler K A. A limit on spin-charge separation in high- T_c superconductors from the absence of a vortex-memory effect. *Nature*, 414:887–889, 2001.

- [240] Subir Sachdev. Stable hc/e vortices in a gauge theory of superconductivity in strongly correlated systems. *Phys. Rev. B*, 45(1):389–399, 1992.
- [241] Naoto Nagaosa and Patrick A. Lee. Ginzburg-landau theory of the spin-charge-separated system. *Phys. Rev. B*, 45(2):966–970, 1992.
- [242] Naoto Nagaoka. e vs. $2e$ Quantization in the Spin Gap Phase of High- T_c Superconductors. *J. Phys. Soc. Jap.*, 63(7):2835–2836, 1994.
- [243] J. C. Wynn, D. A. Bonn, B. W. Gardner, Yu-Ju Lin, Ruixing Liang, W. N. Hardy, J. R. Kirtley, and K. A. Moler. Limits on Spin-Charge Separation from $h/2e$ Fluxoids in Very Underdoped $\text{YBa}_2\text{Cu}_3\text{O}_{6+x}$. *Phys. Rev. Lett.*, 87(19):197002, 2001.
- [244] J.R. Kirtley, Tsuei C.C., Kogan V.G., Clem J.R., Raffy H., and Z.Z. Li. Fluxoid dynamics in superconducting thin film rings. *Phys. Rev. B*, 68:214505–214505, 2003.
- [245] T. W. B. Kibble. Topology of cosmic domains and strings. *J. Phys. A*, 9:1387–1398, 1976.
- [246] T. Kibble. Phase-transition dynamics in the lab and the universe. *Physics Today*, September:47–52, 2007.
- [247] W. H. Zurek. Cosmological experiments in superfluid helium? *Nature*, 317:505–508, 1985.
- [248] P.C. Hendry, N.S. Lawson, R.A.M. Lee, P.V.E. McClintock, and C.D.H. Williams. Generation of defects in superfluid ^4He as an analogue of the formation of cosmic strings. *Nature*, 368:315–317, 1994.
- [249] M. E. Dodd, P. C. Hendry, N. S. Lawson, P. V. E. McClintock, and C. D. H. Williams. Nonappearance of Vortices in Fast Mechanical Expansions of Liquid 4He through the Lambda Transition. *Phys. Rev. Lett.*, 81(17):3703–3706, 1998.
- [250] C. Bäuerle, Yu. M. Bunkov, S.N. Fisher, H. Godfrin, and G.R. Pickett. Laboratory simulation of cosmic string formation in the early Universe using superfluid ^3He . *Nature*, 382:332–334, 1996.
- [251] V.M.H. Ruutu, Eltsov V.B., Gill A.J., Kibble T.W.B., M. Krusius, Yu. G. Makhlin, B. Blaçaïs, G.E. Volovik, and Wen Xu. Vortex formation in neutron-irradiated superfluid ^3He as an analogue of cosmological defect formation. *Nature*, 382:332–334, 1996.
- [252] R. Carmi and E. Polturak. Search for spontaneous nucleation of magnetic flux during rapid cooling of $\text{YBa}_2\text{Cu}_3\text{O}_{7-\delta}$ films through T_c . *Phys. Rev. B*, 60:7595–7600, 1999.
- [253] Raz Carmi, Emil Polturak, and Gad Koren. Observation of Spontaneous Flux Generation in a Multi-Josephson-Junction Loop. *Phys. Rev. Lett.*, 84(21):4966–4969, 2000.
- [254] E. Kavoussanaki, R. Monaco, and R. J. Rivers. Testing the Kibble-Zurek Scenario with Annular Josephson Tunnel Junctions. *Phys. Rev. Lett.*, 85(16):3452–3455, 2000.
- [255] R. Monaco, J. Mygind, and R. J. Rivers. Zurek-Kibble Domain Structures: The Dynamics of Spontaneous Vortex Formation in Annular Josephson Tunnel Junctions. *Phys. Rev. Lett.*, 89(8):080603, 2002.
- [256] J R Kirtley, C C Tsuei, and F Tafuri. Thermally activated spontaneous fluxoid formation in superconducting thin film rings. *Phys. Rev. Lett.*, 90(25; PART 1):257001–257001, 2003.
- [257] M. Hindmarsh and A. Rajantie. Defect formation and local gauge invariance. *Phys. Rev. Lett.*, 85(22):4660–4663, 2000.
- [258] M. Ghinovker, B. Ya. Shapiro, and I. Shapiro. Spontaneous magnetic-flux generation in superconducting ring. *Europhys. Lett.*, 53(2):240, 2001.
- [259] M Donaire, T W B Kibble, and A Rajantie. Spontaneous vortex formation on a superconducting film. *New J. Phys.*, 9(5):148, 2007.
- [260] R. Monaco, J. Mygind, R. J. Rivers, and V. P. Koshelets. Spontaneous fluxoid formation in superconducting loops. *Phys. Rev. B*, 80(18):180501, 2009.
- [261] Kalisky B, Kirtley J R, Nowadnick E A, Dinner R B, Zeldov E, Ariando, Wenderich S, Hilgenkamp H, Feldmann D M, and Moler K A. Dynamics of single vortices in grain boundaries: I-V characteristics on the ferno-volt scale. *Appl. Phys. Lett.*, 94:202504, 2009.
- [262] D. Dimos, P. Chaudhari, J. Mannhart, and FK LeGoues. Orientation dependence of grain-boundary critical currents in $\text{YBa}_2\text{Cu}_3\text{O}_{7-\delta}$ bicrystals. *Phys. Rev. Lett.*, 61:219–222, 1988.
- [263] N.F. Heinig, R.D. Redwing, J.E. Nordman, and D.C. Larbelestier. Strong to weak coupling transition in low misorientation angle thin film $\text{YBa}_2\text{Cu}_3\text{O}_{7-x}$ bicrystals. *Phys. Rev. B*, 60(2):1409–1417, 1999.
- [264] CN Lau, N. Markovic, M. Bockrath, A. Bezryadin, and M. Tinkham. Quantum phase slips in superconducting nanowires. *Phys. Rev. Lett.*, 87(21):217003, 2001.
- [265] N C Koshnick, H Bluhm, M E Huber, and K A Moler. Fluctuation Superconductivity in Mesoscopic Aluminum Rings. *Science*, 318(5855):1440, 2007.
- [266] F. von Oppen and E.K. Riedel. Flux-periodic persistent current in mesoscopic superconducting rings close to T_c . *Phys. Rev. B*, 46(5):3203–3206, 1992.
- [267] DJ Scalapino, M. Sears, and RA Ferrell. Statistical mechanics of one-dimensional Ginzburg-

- Landau fields. *Phys. Rev. B*, 6(9):3409–3416, 1972.
- [268] Xiaxian Zhang and John C. Price. Susceptibility of a mesoscopic superconducting ring. *Phys. Rev. B*, 55(5):3128–3140, 1997.
- [269] H. Bluhm, N.C. Koshnick, J.A. Bert, M.E. Huber, and K.A. Moler. Persistent currents in normal metal rings. *Phys. Rev. Lett.*, 102(13):136802, 2009.
- [270] Jiun-Haw Chu, James G. Analytis, Chris Kucharczyk, and Ian R. Fisher. Determination of the phase diagram of the electron-doped superconductor $\text{Ba}(\text{Fe}_{1-x}\text{Co}_x)_2\text{As}_2$. *Phys. Rev. B*, 79(1):014506, 2009.
- [271] N. Ni, M. E. Tillman, J.-Q. Yan, A. Kracher, S. T. Hannahs, S. L. Bud’ko, and P. C. Canfield. Effects of Co substitution on thermodynamic and transport properties and anisotropic H_{c2} in $\text{Ba}(\text{Fe}_{1-x}\text{Co}_x)_2\text{As}_2$ single crystals. *Phys. Rev. B*, 78(21):214515, 2008.
- [272] S.A.J. Kimber, A. Kreyssig, Y.Z. Zhang, H.O. Jeschke, R. Valentí, F. Yokaichiya, E. Colombier, J. Yan, T.C. Hansen, T. Chatterji, et al. Similarities between structural distortions under pressure and chemical doping in superconducting BaFe_2As_2 . *Nature Mat.*, 2009.
- [273] R.H. Liu, T. Wu, G. Wu, H. Chen, X.F. Wang, YL Xie, J.J. Ying, Y.J. Yan, Q.J. Li, B.C. Shi, W.S. Chu, Z.Y. Wu, and X.H. Chen. A large iron isotope effect in $\text{SmFeAsO}_{1-x}\text{F}_x$ and $\text{Ba}_{1-x}\text{K}_x\text{Fe}_2\text{As}_2$. *Nature*, 459(7243):64–67, 2009.
- [274] W.E. Pickett. Iron-based superconductors: Timing is crucial. *Nature Phys.*, 5(2):87–88, 2009.
- [275] T. Yildirim. Strong Coupling of the Fe-Spin State and the As-As Hybridization in Iron-Pnictide Superconductors from First-Principle Calculations. *Phys. Rev. Lett.*, 102(3):037003, 2009.
- [276] Chen Fang, Hong Yao, Wei-Feng Tsai, JiangPing Hu, and Steven A. Kivelson. Theory of electron nematic order in LaFeAsO . *Phys. Rev. B*, 77(22):224509, 2008.
- [277] Cenke Xu, Markus Müller, and Subir Sachdev. Ising and spin orders in the iron-based superconductors. *Phys. Rev. B*, 78(2):020501, 2008.
- [278] E. Colombier, S. L. Bud’ko, N. Ni, and P. C. Canfield. Complete pressure-dependent phase diagrams for SrFe_2As_2 and BaFe_2As_2 . *Phys. Rev. B*, 79(22):224518, 2009.
- [279] A. I. Goldman, A. Kreyssig, K. Prokeš, D. K. Pratt, D. N. Argyriou, J. W. Lynn, S. Nandi, S. A. J. Kimber, Y. Chen, Y. B. Lee, G. Samolyuk, J. B. Leão, S. J. Poulton, S. L. Bud’ko, N. Ni, P. C. Canfield, B. N. Harmon, and R. J. McQueeney. Lattice collapse and quenching of magnetism in CaFe_2As_2 under pressure: A single-crystal neutron and x-ray diffraction investigation. *Phys. Rev. B*, 79(2):024513, 2009.
- [280] A. Kreyssig, M. A. Green, Y. Lee, G. D. Samolyuk, P. Zajdel, J. W. Lynn, S. L. Bud’ko, M. S. Torikachvili, N. Ni, S. Nandi, J. B. Leão, S. J. Poulton, D. N. Argyriou, B. N. Harmon, R. J. McQueeney, P. C. Canfield, and A. I. Goldman. Pressure-induced volume-collapsed tetragonal phase of CaFe_2As_2 as seen via neutron scattering. *Phys. Rev. B*, 78(18):184517, 2008.
- [281] W. Yu, A. A. Aczel, T. J. Williams, S. L. Bud’ko, N. Ni, P. C. Canfield, and G. M. Luke. Absence of superconductivity in single-phase CaFe_2As_2 under hydrostatic pressure. *Phys. Rev. B*, 79(2):020511, 2009.
- [282] P.L. Alireza, YT Ko, J. Gillett, C.M. Petrone, J.M. Cole, G.G. Lonzarich, and S.E. Sebastian. Superconductivity up to 29 K in SrFe_2As_2 and BaFe_2As_2 at high pressures. *J. Phys.: Cond. Mat.*, 21:012208, 2009.
- [283] J. Zhao, Q. Huang, C. de La Cruz, S. Li, JW Lynn, Y. Chen, MA Green, GF Chen, G. Li, Z. Li, et al. Structural and magnetic phase diagram of $\text{CeFeAsO}_{1-x}\text{F}_x$ and its relation to high-temperature superconductivity. *Nature Mat.*, 7(12):953–959, 2008.
- [284] C.H. Lee, A. Iyo, H. Eisaki, H. Kito, M.T. Fernandez-Diaz, T. Ito, K. Kihou, H. Matsuhata, M. Braden, and K. Yamada. Effect of Structural Parameters on Superconductivity in Fluorine-Free LnFeAsO_{1-y} ($\text{Ln} = \text{La}, \text{Nd}$). *J. Phys. Soc. Jap.*, 77(8):3704, 2008.
- [285] B. Kalisky, J. R. Kirtley, J. G. Analytis, Jiun-Haw Chu, A. Vailionis, I. R. Fisher, and K. A. Moler. Stripes of increased diamagnetic susceptibility in underdoped superconducting $\text{Ba}(\text{Fe}_{1-x}\text{Co}_x)_2\text{As}_2$ single crystals: Evidence for an enhanced superfluid density at twin boundaries. *Phys. Rev. B*, 81(18):184513, 2010.
- [286] IN Khlyustikov and AI Buzdin. Twinning-plane superconductivity. *Adv. Phys.*, 36(3):271–330, 1987.
- [287] MM Fang, VG Kogan, DK Finnemore, JR Clem, LS Chumbley, and DE Farrell. Possible twin-boundary effect upon the properties of high- T_c superconductors. *Phys. Rev. B*, 37(4):2334–2337, 1988.
- [288] D. Dalidovich, AJ Berlinsky, and C. Kallin. Superfluid density near the critical temperature in the presence of random planar defects. *Phys. Rev. B*, 78(21):214508, 2008.
- [289] J. E. Sonier, J. H. Brewer, R. F. Kiefl, D. A. Bonn, S. R. Dunsiger, W. N. Hardy, Ruixing Liang, W. A. MacFarlane, R. I. Miller, T. M. Riseman, D. R. Noakes, C. E. Stronach, and M. F. White. Measurement of the Fundamental Length Scales in the Vortex State of $\text{YBa}_2\text{Cu}_3\text{O}_{6.60}$.

- Phys. Rev. Lett.*, 79(15):2875–2878, 1997.
- [290] AA Abrikosov, AI Buzdin, ML Kulic, and DA Kuptsov. Phenomenological theory for twinning-plane superconductivity in $\text{YBa}_2\text{Cu}_3\text{O}_{7-x}$. *Supercond. Sci. Tech.*, 1:260, 1989.
- [291] G. Deutscher and KA Müller. Origin of superconductive glassy state and extrinsic critical currents in high- T_c oxides. *Phys. Rev. Lett.*, 59(15):1745–1747, 1987.
- [292] John R. Kirtley, Beena Kalisky, Lan Luan, and Kathryn A. Moler. Meissner response of a bulk superconductor with an embedded sheet of reduced penetration depth. *Phys. Rev. B*, 81(18):184514, 2010.
- [293] M. Breitschaft, V. Tinkl, N. Pavlenko, S. Paetel, C. Richter, J. R. Kirtley, Y. C. Liao, G. Hammerl, V. Eyert, T. Kopp, and J. Mannhart. Two-dimensional electron liquid state at $\text{LaAlO}_3 - \text{SrTiO}_3$ interfaces. *Phys. Rev. B*, 81(15):153414, 2010.
- [294] N. Reyren, S. Thiel, AD Caviglia, L. Kourkoutis, G. Hammerl, C. Richter, CW Schneider, T. Kopp, A.S. Ruetschi, D. Jaccard, et al. Superconducting interfaces between insulating oxides. *Science*, 317(5842):1196, 2007.
- [295] R. Prozorov, M. A. Tanatar, N. Ni, A. Kreyssig, S. Nandi, S. L. Bud'ko, A. I. Goldman, and P. C. Canfield. Intrinsic pinning on structural domains in underdoped single crystals of $\text{Ba}(\text{Fe}_{1-x}\text{Co}_x)_2\text{As}_2$. *Phys. Rev. B*, 80(17):174517, 2009.
- [296] F.C. Wellstood, C. Urbina, and J. Clarke. Low-frequency noise in dc superconducting quantum interference devices below 1 K. *Appl. Phys. Lett.*, 50:772, 1987.
- [297] R.H. Koch, J. Clarke, WM Goubau, JM Martinis, CM Pegrum, and DJ Harlingen. Flicker (1/f) noise in tunnel junction DC squids. *J. Low Temp. Phys.*, 51(1):207–224, 1983.
- [298] H. Bluhm, J.A. Bert, N.C. Koshnick, M.E. Huber, and K.A. Moler. Spinlike Susceptibility of Metallic and Insulating Thin Films at Low Temperature. *Phys. Rev. Lett.*, 103(2):26805, 2009.
- [299] F Tafuri, J R Kirtley, P G Medaglia, P Orgiani, and G Balestrino. Magnetic imaging of Pearl vortices in artificially layered $(\text{Ba}_{0.9}\text{Nd}_{0.1}\text{CuO}_{2+x})_m/(\text{CaCuO}_2)_n$ systems. *Phys. Rev. Lett.*, 92(15):157006, 2004.
- [300] JR Kirtley, CC Tsuei, KA Moler, VG Kogan, JR Clem, and AJ Turberfield. Variable sample temperature scanning superconducting quantum interference device microscope. *Appl. Phys. Lett.*, 74:4011, 1999.
- [301] E. Nazaretski, JP Thibodaux, I. Vekhter, L. Civale, JD Thompson, and R. Movshovich. Direct measurements of the penetration depth in a superconducting film using magnetic force microscopy. *Appl. Phys. Lett.*, 95:262502, 2009.
- [302] Lan Luan, Ophir M. Auslaender, Thomas M. Lippman, Clifford W. Hicks, Beena Kalisky, Jiun-Haw Chu, James G. Analytis, Ian R. Fisher, John R. Kirtley, and Kathryn A. Moler. Local measurement of the penetration depth in the pnictide superconductor $\text{Ba}(\text{Fe}_{0.95}\text{Co}_{0.05})_2\text{As}_2$. *Phys. Rev. B*, 81(10):100501, 2010.
- [303] V. G. Kogan. Meissner response of anisotropic superconductors. *Phys. Rev. B*, 68(10):104511, Sep 2003.
- [304] Clifford W. Hicks, Thomas M. Lippman, Martin E. Huber, James G. Analytis, Jiun-Haw Chu, Ann S. Erickson, Ian R. Fisher, and Kathryn A. Moler. Evidence for a Nodal Energy Gap in the Iron-Pnictide Superconductor LaFePO from Penetration Depth Measurements by Scanning SQUID Susceptometry. *Phys. Rev. Lett.*, 103(12):127003, 2009.
- [305] Roman G. Mints, Vladimir G. Kogan, and John R. Clem. Vortices in magnetically coupled superconducting layered systems. *Phys. Rev. B*, 61(2):1623–1629, 2000.
- [306] D A Bonn and W N Hardy. In J R Schrieffer, editor, *Handbook of High Temperature Superconductivity*. Springer, New York, 2007.
- [307] T Pereg-Barnea, P J Turner, R Harris, G K Mullins, J S Bobowski, M Raudsepp, R Liang, D A Bonn, and W N Hardy. Absolute values of the London penetration depth in $\text{YBa}_2\text{Cu}_3\text{O}_{6+y}$ measured by zero field ESR spectroscopy on Gd doped single crystals. *Phys. Rev. B*, 69:184513, 2004.
- [308] JH Xu, JH Miller Jr, and CS Ting. Magnetic levitation force and penetration depth in type-II superconductors. *Phys. Rev. B*, 51(1):424–434, 1995.
- [309] Q. Lu, K. Mochizuki, J. T. Markert, and A. De Lozanne. Localized measurement of penetration depth for a high T_c superconductor single crystal using a magnetic force microscope. *Phys. C*, 371(2):146–150, 2002.
- [310] H. Kim, R.T. Gordon, M.A. Tanatar, J. Hua, Welp U., W.K. Kwok, N. Ni, S.L. Bud'ko, P.C. Canfield, A.B. Vorontsov, and R. Prozorov. London penetration depth in $\text{Ba}(\text{Fe}_{1-x}\text{T}_x)_2\text{As}_2$ ($\text{T}=\text{Co},\text{Ni}$) superconductors irradiated with heavy ions. *arXiv:1003.2959*, 2010.
- [311] E W J Straver, J E Hoffman, O M Auslaender, D. Rugar, and K. A. Moler. Controlled manipulation of individual vortices in a superconductor. *Appl. Phys. Lett.*, 93:172514, 2008.
- [312] O. M. Auslaender, L. Luan, E. W. J. Straver, J. E. Hoffman, N. C. Koshnick, E. Zeldov, D. A.

- Bonn, R. Liang, W. N. Hardy, and K. A. Moler. Mechanics of individual isolated vortices in a cuprate superconductor. *Nature Physics*, 5:35–39, 2008.
- [313] J.C. Keay, P.R. Larson, K.L. Hobbs, M.B. Johnson, J.R. Kirtley, O.M. Auslaender, and K.A. Moler. Sequential vortex hopping in an array of artificial pinning centers. *Phys. Rev. B*, 80:165421, 2009.
- [314] B.W. Gardner, J.C. Wynn, DA Bonn, R. Liang, WN Hardy, J.R. Kirtley, V.G. Kogan, and K.A. Moler. Manipulation of single vortices in $\text{YBa}_2\text{Cu}_3\text{O}_{6.354}$ with a locally applied magnetic field. *Appl. Phys. Lett.*, 80:1010, 2002.